Stony Brook University

The Role of Surface Interactions and Morphology in Determining Thermal Dynamic Properties of Polymer Nanocomposites

A Dissertation Presented

by

Seongchan Pack

to

The Graduate School

in Partial Fulfillment of the

Requirements

for the Degree of

Doctor of Philosophy

in

Materials Science and Engineering

Stony Brook University

May 2010

Stony Brook University

The Graduate School

Seongchan Pack

We, the dissertation committee for the above candidate for the **Doctor of Philosophy** degree, hereby recommend acceptance of this dissertation.

Dr. Miriam H. Rafailovich – Dissertation Advisor
Professor, Materials Science and Engineering

Dr. Jonathan C. Sokolov
Professor, Materials Science and Engineering

Dr. Gary Halada
Associate Professor, Materials Science and Engineering

Dr. Steven A. Schwarz
Professor, Physics, Queen College, NY

Dr. Nan-Loh Yang
Professor, Chemistry, College of Staten Island, NY

This dissertation is accepted by the Graduate School

Lawrence Martin
Dean of the Graduate School

Abstract of the Dissertation

The Role of Surface Interactions and Morphology in Determining Thermal Dynamic Properties of Polymer Nanocomposites

by

Seongchan Pack

Doctor of Philosophy

in

Materials Science and Engineering

Stony Brook University

2010

Since interfacial properties rely on interactions between polymers and nanoparticles at interfaces, obtaining a minimization of the interfacial energy can be complicated when nanoparticles are added in a polymer blend, even more complicated when the blend is mixed with conventional flame retardant (FR) agents. We here show that the addition of nanoparticles, such as layered silicates and carbon nanotubes (CNTs), could not only enhance the compatibilization of immiscible polymer blends but also improve the degree of the dispersion of FR agents, since the nanoparticles were seen at either the blend interfaces or the FR agents. In addition, we have demonstrated that the addition of the clays can stabilize the blends against further phase segregation, thereby suppressing the formation of either ribbon-like or tubular-like structures along the interfaces during heating. These structures can significantly improve flame retardant properties, such as heat release rate (HRR) and mass loss rate (MLR), which can be evidenced by enhanced thermal conduction within the structures. In spite of these improvements, most polymer blends with the nanoparticles cannot be rendered self-extinguishing unless the conventional FR agents are added. Furthermore, too much added

FR agents deteriorate material properties because the FR agents can be classified as an additive. Therefore, we have showed that the FR agents can be directly absorbed on the clay surface, which not only improves the dispersion of FR agents but also results in the exfoliation and/or intercalation in several homopolymers. The strong absorption of FR agents on the nanoparticles can effectively achieve the result of self-extinguishment. This is obtained from the interfaces between the FR agents and the nanoparticles, where a synergy may be attributed to the interfacial activity and the improved thermal conductivity. Finally, we here explain a mechanism of the self-extinguishment of nanocomposites containing both the FR agents and the nanoparticles in terms of the thermal dynamic behaviors of the nanoparticles.

Dedicated To

My

Family

TABLE OF CONTENTS

LIST OF FIGURES

LIST OF TABLES

LIST OF ILLUSTRATIONS

Acknowledgements

People believe of what they think even though they do not know how to explain it properly. On the other hand, science does know how to precisely demonstrate the thought that people have. Earning a degree of doctor of philosophy is a beginning step for me to connect the people with the science. Before PhD I was one of the people. Now I am so deeply thoughtful and able to contribute my science knowledge to societies and nations. I must mention my gratitude to people who already know how to make the world better with their knowledge. Without them, I could not learn the lesson. Here I present them.

First of all, my dissertation advisor, Professor Miriam Rafailovich, is my super-mentor not only for science knowledge, creativity and research guidance, but also for various components of my life. She has tremendously shown me essential qualifications of being a scientist day by day. I sincerely thank Dr. Rafailovich for the chance to be her PhD student.

I greatly thank Prof. Takashi Kashiwagi for his enthusiastic guiding my research in spike of my poor background of combustion at the beginning. By his every effort, I was able to extend my research area to fundamental study of nanocomposite in flame retardant. I thank him for giving me the honor of working together.

I thank Prof. Jonathan Sokolov, for generous assistance, discussion and suggestions for my research as well as for my life as a parent.

I also thank Prof. Steven Schwarz, for serving my preliminary and dissertation committee and his suggestions.

I also thank Prof. Gary Halada, for serving my dissertation committee and his suggestions.

It is also my pleasure to extend my gratitude to Professor Na-Loh Yang, for serving my dissertation committee, suggesting valuable comments on my research, and giving me good science knowledge in chemistry.

I greatly appreciate the senior scientists for their assistance and valuable comments – Prof. Edward Weil, Prof. Menachem Lewin, Prof. Tadanori Koga, Steven Bennett.

Dr. Jaseung Koo –He is my best friend and brother who take care of me with everything that he could share. I wish he will be my best man for my wedding. I thank him for sharing my concerns which I took during PhD.

I also would like to thank my colleagues, Dr. Binquan Li, Dr. Xaiohua Fang, Dr. Mayu Si, Dr. Yuan Ji, Dr. Yuan Sun, Dr. Chunghua Li, Dr. Jun Jiang, Dr. Yiantian Wang, Dr. Clive Li, Dr. Perumal Ramasamy, Dr. Zhi Pan, Dr. Jim Quinn, Dr. John Jerome, Dr. Brian Choi, Dr. Jae hun Kim, Dr. Kyunghwan Yoon, Ying Liu, Xiaolan Ba, Tatsiana Mironava, Chungchueh Chang, Divya Bhatnagar, Eli Hoory, Chien-Hsu Lin, Cheng Pan, SiSi Qin, Jennifer Segui, Jason H.C. Yang, Liudi Zhang, Kai Yang, Youjun Zhai, Jusang Lee, Jungkwon Chung, Nahyun Cho for their help and discussions.

I specially thank Ms. Susan Von Horn, Ms. Lourdes, my undergraduate students and high school students, for supporting my research during my the PhD. Finally, I thank my parents, younger brother, and Miss Su Jung Han, for their support. Since their love and encouragement have driven a completion of my dissertation, I hereby dedicate this dissertation to my parents, younger brother, and Miss Su Jung Han.

Chapter 1: Introduction: Background and Synergies in Nanoparticles/Flame Retardants in Polymer Blends.

1.1. Flame Retardants (FR) in Immiscible Polymer Blends.

Flame retardance is a process of disrupting burning process, which have several stages involving physical and chemical reactions. The addition of flame retardant (FR) agents is a conventional method for achieving flame retardant materials and composites. In general, there are two major categories in flame retardants: halogenated and non-halogenated FR agents. They have been developed for use as either additives or plasticizers [1-3]. Halogenated FR agents mostly consist of bromine or chlorine compounds. They can produce the hydrogen halides that react with either hydrogen or hydroxyl radicals during combustion. Therefore, the rate of chain reactions can be reduced because the hydrogen halides inhibit the exothermic oxidation reactions [4]. On the other hand, non-halogenated FR agents have been extensively developed due to an increase of environmental concerns regarding the use of the halogenated FR derivatives. The use of aryl phosphates are an alternative for replacing the halogenated FR agents, where they are well known for flame retardants in aromatic compounds.[5]

However, it is difficult to obtain a good mixture of polymer blends with flame retardants since they are immiscible in the blends, which can lead to a formation of agglomerated FR agents. This situation is more complicated when the blends are exposed to heat because thermal responses of the blends can continuously change at elevated temperatures. Therefore, the agglomerated FR agents do not produce high efficiency in flame retardancy. In addition, too much added FR agents can deteriorate mechanical properties of the blends. Although phosphate-based FR agents serve somewhat as a plasticizer, they still phase separate with the polymer blends, especially, styrenic resins.

Hence the degree of dispersion of FR agents in polymer blends can be an important factor to determine flame retardancy of the blends.

1.2. The Synergy of a Combination of Flame Retardants (FR) Additives with Nanoparticles.

The addition of nanoparticles, such as organoclays and carbon nanotuebs, is known to improve the mechanical and thermal properties of polymeric materials since they have shown excellent physical and chemical properties in melt polymers at the molecular level, where polymer chains strongly interact with either individual nanoparticle or its entanglements [6-7]. Recently, Si *et al.* and others investigated that the addition of functionalized clays could enhance the efficacy of various compound formulations for rendering homopolymers flame retardant [8-9]. They demonstrated that with the small quantities of clays, much less of the flame retardant (FR) formulations had to be added in order to achieve a significant reduction in the heat release rate (HRR) and mass loss rate (MLR). On the other hand, the addition of carbon nanotubes (CNTs) can also show the improved thermal responses when the nanotubes are well entangled and dispersed within melt polymers. Kashiwagi *et al*. found that when either 1.0 wt% mulit-wall carbon nanotubes (MWCNTs) or 0.5 wt% single-wall carbon nanotubes (SWCNTs) was added to poly (methyl methacrylate) PMMA homopolymer, the continuous network-like protective layers were formed, which could lead to the reduction on HRR and MLR [10].

Although homopolymers are relatively easy to obtain self-extinguishments, it is difficult to predict the thermal properties of polymer blends because thermal degradations are involved at different temperatures as well as phase separation occurring continuously. As a result of that, the distribution of the FR components in the blends cannot be the same as that when the blends are heated. We showed that the inclusion of large aspect nanoparticles was one solution to predict thermal responses in the morphology of polymer blends containing FR agents, where they segregated to the interfacial regions,

thereby stabilizing the blends against further thermal decomposition. Furthermore, since the FR agents were seen at the nanoparticles surfaces, the high aspect ratio particles also acted as dispersants of the FR particles. We therefore postulated that an additional synergy could exist when the two types of nanoparticles were combined. I will discuss more details in chapter 2 and 3.

1.3. The Surface Interaction between Flame Retardants (FRs) and Nanoparticles.

Knowing the interfacial tension between FR agents and nanoparticles can be useful to design, synthesize, and fabricate flame retardant formulations. Since the FR agents are favorable to certain polymers the strong absorption of FR agents on nanoparticles can be one solution for replacing di-tallow surfactants on clays, where several toxic chemical processes were used to produce the functionalized clays [11-12]. We showed that resorcinol bis(diphenyl phosphate) (RDP), an oligomeric phosphate ester, could be intercalated in the clay galleries. We also demonstrated that the intercalated RDP clays were exfoliated in homopolymers, while they retain the ability for compatibilization in some polymer blends. These effects were confirmed by the combination of transmission electron microscope (TEM) images with small angle X-ray scattering (SAXS) experiments. The absorption RDP on the clay surfaces could result from screening the charged clay surfaces, which ultimately produced a very thin RDP oligomers layers in clay intergallaries. Therefore, interfacial tension between the thin RDP layer and the clay surface can be an important determinant to obtain a minimization of the interfacial energy. We measured the values of surface tensions for the RDP oligomers at the processing temperatures. Using the contact angles we were able to calculate the interfacial tensions between RDP and polymers. We found that the contact angle for between polystyrene (PS)/RDP clays substrate was ~ 2.5°, whereas the angle for PS/Cloisite 20A clays substrate was ~ 32°. Therefore, the RDP coated clays were

more compatible to the styrene groups compared to the Cloisite clays. Furthermore, we showed that since the RDP oligomers were more thermal stable the flame retardant properties, such as HRR and MLR, were also enhanced. In chapter 4, I will demonstrate the enhancements more detail.

Chapter 2: Mode-of-Action of Self-extinguishing Polymer Blends Containing Organoclays.

2.1. Introduction

The use of functionalized organoclays is known to enhance the physical and chemical properties of polymer nanocomposites since they have been shown to intercalate or exfoliate within the polymer matrix and interact with the polymer chains at the molecular level [6,13-14]. Most of the current work has focused on homoplymer nanocomposites, where the results could be explained in terms of the interactions between the clay functional groups and the polymer host [15-22]. Recently, Si *et al*. and others have demonstrated that clays can also enhance the efficacy of various formulations for rendering homopolymers flame retardant (FR) [8, 9, 42]. They demonstrated that with the addition of small quantities of clays, much less of the flame retardant formulations had to be added in order to achieve a significant reduction in the heat release rate (HRR) and mass loss rate (MLR). Since the FR standard formulations also embrittle the matrix, the ability to reduce the volume fraction of additives resulted in nanocomposites with better mechanical properties, which were also able to pass the stringent flame tests conditions required to obtain UL-94-V0 certification [8-9].

The situation is much more complex in a polymer blend. The ability of clays to exfoliate or intercalate, does not depend only on the clay-polymer interaction, but also on the interactions between the polymers [24-30]. The thermal properties are even more complicated, since the properties of the blend can change continuously as the blend is heated to high temperatures and phase separation accelerates. Recently, Si *et al*. [31] showed that when functionalized clays were introduced into a polymer blend, *in situ* grafts were formed, as polymer chains from the blend absorbed onto the clay surfaces.

These grafts have very high energies in either of the phases and hence segregate strongly to the phase interfaces, effectively reducing the interfacial tension. Hence they showed that clays could potentially stabilize the blend against phase segregation. Furthermore, since this mechanism was activated in-situ, the process was relatively non-specific and could work for a wide spectrum of binary blends.

When FR formulations are added to polymer blends, they tend to segregate in one of the phases. As the phase segregation proceeds during heating, the efficacy of the formulation is further reduced, since its agglomeration becomes more severe. In this case the clays may have an even larger impact on the entire system, than in the case of the homopolymer nanocomposites. We show that in the case of the blend nanocomposites, the clays stabilize the system against progressive phase segregation even during high temperature heating, maintain the dispersion of the flame retardant formulations, and dramatically increase the flame resistance of the entire matrix of polymer blend nanocomposites.

We focus on two polymer blend model systems, which Si *et al*. [31] had characterized and demonstrated that they could be compatiblized by organo-clays. We then expose the blends to intense heating and study the distribution of the clays and flame retardant formulations within the nanocomposites, using a variety of complementary techniques. The results are then correlated with the thermal and mechanical properties of the system, where we demonstrate that strong synergy between the flame retardants and the clays also enable us to obtain blend nanocomposites with superior mechanical properties that can pass the UL-94V0 test.

2.2. Experimental Section

2.2.1. Materials and Nanocomposite Preparation.

The properties of the polymers used in this study are tabulated in Table 2.1. Polystyrene (PS) with an average molecular weight of 280K, and poly(methyl methacrylate) (PMMA) with an average molecular weight of 120K, were obtained from AMCO plastics. Cloisite 20A was provided by Southern Clay Products Inc. The halogen based flame retardant (FR) compound was decabromodiphenyl ether (DB), purchased from Sigma Aldrich and the catalyst, an antimony trioxide, Microfine® AO3, (AO) was purchased from Great Lakes Chemical Corporation. Polycarbonate (PC), average Mw= 23K, and poly(styrene-co-acrylonitrile) (SAN with 24 wt% AN, known as Luran 358N) were obtained from Mitsubishi Engineering Plastic Corp and BASF, respectively. A C.W. Brabender twin screw extruder was used to blend the nanocomposites. The polymers were first added in the chamber at a rotation speed of 20 rpm, and temperature of 170 °C or 230 °C for PC and mixed for 1 min. The FR agents were then added and blended at the same rpm for 2 min. Finally, the Cloisite 20A clay was gradually introduced into the chamber, while mixing. The entire mixture was blended at 100 rpm for 15 min. under nitrogen gas flow, which was added to suppress degradation due to heat-induced oxidation. The melt was allowed to cool at room temperature, and then molded in a hot press, into the different shapes required for the various mechanical tests that were performed.

2.2.2. Flame Test Measurements.

Cone calorimetry was performed at NIST, where the HRR and the MLR of each sample (35 ± 2 g) were measured as a function of time in either air or nitrogen. The samples, whose dimensions were 75 mm x 75 mm x 5 mm, were first wrapped with thin aluminum foil except for the irradiated sample surface. They were then exposed in a horizontal position to an external radiant flux of 50 kW/M^2 in order to measure the HRR and MLR. The residues in the foil were collected and their morphology analyzed using the scanning electron microscopy (SEM). The standard uncertainty of the measured HRR was ± 10 %. The test was done following ASME/ISO 5660. A vertical burning chamber

purchased from Underwriters Laboratories Inc. was used to test for flammability. The protocols were obtained from ASTM D3801/ISO 1210 UL 94 V0, where we timed the duration of the flame and recorded whether the nancomposites dripped and ignited a wad of cotton under the holder. The samples, whose dimensions were 125 mm x 13 mm x 1.5 mm, were clamped in the upper 10 mm from a long stand and hung in the vertical direction. A compressed methane gas burner with a gas flow rate of 105 ml/min was used in this test. The flame with its height, 20 ± 1 mm, was applied to the bottom of the sample for 10 sec at two times, maintaining the distance, 10 ± 1 mm, between the bottom and the top of the flame. After the test, the samples were cut into three parts. The first piece was obtained from the bottom of the sample, which was closest to the flame. The second one was taken 30 mm away from the first cut in the sample. The last one was cut 30 mm away from the second cut in the same sample. The samples were then cut by a microtome and floated onto carbon coated grids for transmission electron microscope (TEM) analysis.

2.2.3. Nanocomposite Characterizations

2.2.3.1. Morphological Measurements:

Transmission electron microscopy (TEM) was conducted with samples obtained from before or after the vertical burning test. The cross sections whose thickness was 70-80 nm were cut by a Reichert-Jung Ultracut E Ultramicrotome and then were placed on coated copper mesh grids. Morphology of the sections was viewed from a FEI Tecnai12 BioTwinG^2 TEM at 80 kV and digital images were acquired with an AMT XR-60 CCD digital camera system. The FR agents in the polymer matrixes were identified by an energy dispersive X-ray spectroscopy (EDXS) in the scanning electron microscope (SEM) (LEO-1550) with a Schottky field-emission gun where the specimens (10 mm x 10 mm x 2 mm), burned as a function of time at the high temperature of 650 °C in Lindberg SB. Type 167 oven chamber, were mapped for 10 min. The SEM was also performed with the residues after the cone calorimetry test. A few micrometers of gold were coated on the surface of the residues in order to make the specimens conduct.

2.2.3.2. X-ray Scattering Measurements:

Small angle X-ray scattering (SAXS) was performed with all samples (2 mm in thickness), which were annealed at different temperatures for 5 min, to analyze microstructures, where peaks corresponded to interlayer spacings within the clays. The SAXS was conducted at a beam line X10A at National Synchrotron Light Source (NSLS) at Brookhaven National Laboratory. The wavelength used in the beam was 1.09 Å. The q range was from 0.04 to 0.58 $Å^{-1}$. The distance between the samples and the detector was 81.20 cm. An extended X-ray fine absorption structure (EXFAS) was performed in order to verify a change of the chemical molecular structure of Br-containing particles occurring in the condensed phases. The Br K-edge XFAS data was collected from all specimens (0.5 mm in thickness) containing the clays and without the clays. The specimens for EXFAS were burned at different temperatures for 20 sec in the oven chamber. The X-ray beam, X11B at the NSLS, prepared from the Si (111) double crystal monochromator was used to scan a range of X-ray energy from 150 eV below the Br K-edge (13,474 eV) to 1000 eV above it. After three scans were averaged, the data were processed with the IFEFFIT package [48].

2.2.3.3. Thermodynamic and Thermal Stability Measurements:

Mechanical property of the samples was analyzed by a Mettler Toledo DMA/SDT 861e in the single cantilever mode. The dimensions of the samples were 10 mm x 10 mm x 2 mm. Storage modulus and tan delta were measured as a function of temperature, where temperature increased to 180 °C from room temperature at a frequency of 1 Hz with a heating rate 2 °C /min. A differential scanning calorimeter (DSC) was used in order to measure the specific heat of the chars. The DSC measures the heat flow of the chars as a function of time and temperature. The mass of the samples, which is required in order to correctly figure out the specific heat, was used and input into the formula,

$$Cp = \frac{\Delta \mathrm{H}}{\Delta \mathrm{T} \times \mathrm{M}} = \left(\frac{d\mathrm{H}}{dt}\right)\left(\frac{dt}{d\mathrm{T}}\right)\left(\frac{1}{\mathrm{M}}\right)$$

,where ΔH is the enthalpy change, ΔT is the temperature change, dH/dt is the heat flow difference between the blank and the sample, dt/dT is the reverse of the heating rate (20 °C /min) and M is the mass of the sample. A thermogravimetric analysis (TGA) of

using a Mettler-Toledo instrument was used to compute the mass loss in a sample as the temperature steadily increases. A small mass of a sample was measured and then inserted into a crucible. The crucible with the sample was inserted into the furnace and then the temperature was increased from 30 °C to 850 °C at a rate of 10 °C/min. The TGA measured was normalized in a percentage of mass loss or was derivatived to mass loss versus temperature for further study.

2.3. Results

2.3.1. Microstructures of Nanocomposites.

The dispersion of FR formulation when clays are present is shown in figure 2.1. for the PMMA homopolymer. The dark particles in the figures are the DB/AO particles, which are electron dense. From the figures it is very easy to discern that the particle size is smaller and the particle distribution is more uniform when 5 % Cloisite 20A clay is added. In figure 2.1b we can see that the FR particles are adsorbed onto the surfaces of the clay platelets. Since the clays are well dispersed inside the PMMA matrix, the FR formulation associated with the clay platelets is also dispersed better. In figure 2.2 we compare the TEM micrographs of a 70-30 weight percent PS/PMMA/FR blend with and without 5% clay. From the figures we can see several main effects; (a) the clays are segregated primarily into the PMMA domains which is consistent with the previous results of Hu *et al.*[23] that indicated that PMMA polymer chains in a PS/PMMA melt matrix adsorbed preferentially to Cloisite 20A clay surfaces. (b) The FR agents are also segregated primarily into the PMMA domains, which are slightly more polar than the PS. In the absence of clays, the PMMA domains are a few microns in diameter, which also define the cluster size of the FR. As a result, comparing figure 2.1 and 2.2, it is clear that the dispersion of the FR is even worse in the blends than in the homopolymers. With the addition of clays, the domain sizes are drastically reduced. Furthermore, as was shown in figure 2.1b, the FR is still attached to the clay surfaces, resulting in smaller particles and better dispersion within the domains. Inspection of figure 2.2c also shows that the clays segregated to the interfacial regions between the PS/PMMA domains. This segregation was previously explained to occur from *in situ* graft formation on the clay surfaces, which greatly reduced the interfacial tension, resulting in the compatibilization properties of the clays [31]. Careful inspection, though, of the images also shows that the FR agents absorbed into the clays surfaces that have segregated to the interfacial regions. This effect also increases the dispersion of the FR agent within the PS phase, and hence helps the FR agent work more effectively.

Si *et al.* has shown that the ability of clays to compatiblize blends is fairly non-specific, as long as the clays exfoliated in one or both of the polymers. The PS/PMMA

system was an example of the first case, while PC/SAN24 was an example of the second case where they showed that the degree of compatibilization was even higher and a single T_g could be achieved. In the case of the PC/SAN24 blend, the microstructure of the domains becomes more complicated when the FR formula is added. In figure 2.3 we show TEM images of a PC/SAN24/FR blend. Since the X-ray contrast between the polymers is low, we also performed scanning transmission X-ray microscopy (STXM) in order to identify the phases and plot the STXM images alongside the TEM figures. In figure 2.3a and 2.3c, we show the blend with the FR, but without clay. Comparing the STXM image with the TEM image shows that the FR is segregated almost completely inside the SAN phase. The blend with the added clays and the FR is shown in figure 2.3b and 2.3d. Comparing with the previous data of Si *et al.* we find that the degree of compatibilization is not as good as that reported in the absence of the FR agent. Closer examination of the figures reveals one possible explanation. In this case we can see that FR agent is now segregated to the clay surfaces, which are clearly preferred over the SAN phase. The FR agent therefore competes more effectively than the polymer chains for the clay surfaces, reducing the ability of the clay to form *in situ* polymer grafts, which in turn reduces the interfacial activity of the clays. It may be confirmed by the fact that there are still two T_g, one at about 125 °C and the other at about 148 °C, compared to one T_g in PC/SAN24/Cloisite 20A, which was reported in the previous paper [31], even though the storage modulus increases from 2.75 to 3.75 GPa, which is shown in Figure 2.4a and 2.4b. Hence the addition of the clay greatly increased the dispersion of the FR agent in spite of the poor degree of compatibilization.

The degree of compatibilization can be indirectly predicted by how well the clays are exfoliated and/or intercalated in the presence with the FR particles. In order to determine the degree of exfoliation and/or intercalation of the clay, we performed SAXS on PMMA/DB/AO/Cloisite20A, PS/PMMA/DB/AO/Cloisite 20A, and PC/SAN24/DB/AO/Cloisite 20A nanocomposites. The spectra are shown in figure 2.5. where the peak positions are marked by the vertical lines so that they can be directly compared. From the figure we can see that the trace of pure Cloisite 20A clay has two peaks at $q = 0.2319$ Å^{-1} and $q = 0.4638$ Å^{-1}, where $q = 4\pi\sin\theta/\lambda$. Using the relationship,

$d_{001} = 2\pi/q$, we obtain the interlayer spacing in the direction of [001] and [002], which are listed in table 2.2.

In the case of the pure Cloisite 20A, these values are 2.70 nm and 1.35 nm, respectively. After blending with PMMA/DB/AO, the d spacing increases to 4.10 nm, which indicates that polymer chains are intercalated into the clay galleries. This behavior is in contrast to that reported by Si *et al.* for PMMA/SPN without the FR formulation, where no peaks are observed and where TEM images indicate nearly complete exfoliation [20]. In this case, even though the scattering is low and only the primary peak is observable, we find that the clay is partially exfoliated. This result is also consistent with the TEM images shown in figure 2.1 where only partial exfoliation is observed. From figure 2.1 we can also see that the FR formulation is adsorbed to the clay platelets and tactoids, indicating that it may compete with the polymer chains for the clay surface and hence it can hinder the penetration of the polymer chains into the galleries and the exfoliation process. In the case of the PS/PMMA/DB/AO/Cloisite20A, the peak intensity is larger, indicating that an even smaller fraction of the clay is exfoliated. The clay peaks are visible at q values corresponding to d_{001} = 4.05 nm and d_{002} = 2.03 nm, indicating a large degree of intercalation. Comparing the TEM micrographs of the PMMA homopolymer in figure 2.1 with that of the PS/PMMA blend in figure 2.2 we see that the clays are localized at the blend interfaces. Since Cloisite 20A is known to partially exfoliate only in PMMA and only barely disperses in PS, the localization at the interfaces can only occur if individual clay platelets do not cross into the PS phase. This relationship favors intercalation, rather than exfoliation.

In the case of the PC/SAN24/Cloisite 20A nanocomposite, the clays were shown to exfoliate in both phases, and Si *et al.* showed that above 3 % clay, the two polymers became completely miscible [31]. Here we show that this is no longer the case when the FR formulation is added. In the inset of figure 2.3 we show the STXM images of a cross section from the PC/SAN24/DB/AO (50/50/15/4/5 wt %) blend, with and without 5 % of Cloisite 20A clay. From the images we see that the continuous phase (bright) is PC, while the discontinuous phase is SAN24. In the TEM images there is not much density contrast between the two polymers and only a faint outline of the discontinuous phase can be seen. The degree of miscibility does not seem to be much affected by the clays, when the

FR is also added. This result is consistent with the SAXS data, where we can see that in the PC/SAN24/DB/AO/Cloisite 20A nanocomposite, the clays are intercalated rather than exfoliated in figure 2.3. Closer examination of the TEM images (figures 2.3c and 2.3d) shows that in the absence of clays the FR components, which appear as dark electron dense regions, are localized in the SAN24 discontinuous phase. When the Cloisite 20A clay is added we see that the clay platelets prefer the continuous PC phase, but a large fraction are also localized at the interfaces between the PC and SAN24 phases. In this blend as well, the FR particles are observed to be adsorbed to the clay platelet surfaces, which results in a better dispersion and reduction of the particle size. But in contrast to the images observed for the PS/PMMA blend, the FR coated clay platelets are not confined in the PC phase, but are clearly segregated along the interfacial regions. Even though the clay tactoids along the interfaces and in the PC regions appear smaller than those in the PMMA phase, the interlayer spacing between clay platelets is clearly smaller. As a result of that, the spectra of SAXS in figure 2.5 shows that the intercalation of the clays in the PC/SAN24/DB/AO blend is less than that of the clays in PS/PMMA/DB/AO blend, which are d_{001} = 3.57 nm and d_{002} = 1.79 nm in table 2.2. Therefore, when halogenated FR formulations are mixed with Cloisite 20A clays, the FR components are seen to be attracted to the clay platelets surfaces, and compete effectively with the polymer chains for adsorption sites. While this effect increases their dispersion, it also decreases the ability of the platelets to exfoliate in the polymers or produce the *in-situ* grafts with the polymers, which were shown by Si *et al.* to be responsible for the compatiblization mechanism in polymer blends.

2.3.2. Burned Microstructures in PS/PMMA with FR and Clay Nanocomposites.

Even though the compatibilization is not optimal, addition of the FR formulations does not prevent the clay platelets from being localized along the interfaces. Hence a more relevant question becomes whether the clay platelets can stabilize the internal microstructures against further phase separation when the blend is exposed to flame. We first examined the PS/PMMA blend samples after they were exposed in a small scale of flame and passed a mock UL-94 V0 test, as described in the illustration 2.1. Here the

samples are suspended and exposed to the flame at the bottom for 10 seconds. We then cross sectioned the samples and examined three regions, 10 mm, 40 mm and 70 mm away from the flame. The results are shown in figure 6 and 7. The top portion, which is furthest away from the flame, is seen to be relatively unchanged from the images of the unexposed composites shown in figure 2.6a and 2.7a. As before, we see distinct PMMA domains in which both the FR particles and the clay platelets are visible. PMMA phases are well dispersed and their size varies from a few micrometers to about a hundred nanometers. The clay platelets reside in PMMA phases or on the interfaces between PS and PMMA phases, which is shown in figure 2.7a. The morphology of the PMMA domains begins to change in the figures. The outlines of the domains remains fixed, but the actual PMMA appears to disintegrate. This is consistent with the fact that PMMA polymer begins to unzip and sublime at the temperature of the flame. Yet, it is interesting to note that the outlines of the domains remain fixed and the overall phase separated morphology does not change. In figure 2.6c and 2.7c we show images of the section that was in direct flame. Here we also see the outlines of the PMMA phases are preserved, and we find that the clays remain concentrated in the PMMA domains.

Hence the clays at the periphery stabilize the domains against coalescing, before disintegrating. Closer examination of the clays left behind in the PMMA domains show that they coalesce into small tube like formations, at temperatures where it was previously shown that the surfactants molecules charge-exchanged onto the clay surface begin to decompose. This response is further confirmed by SAXS data of the nanocompsite samples annealed in air for approximately 5 min at different temperatures. From the figure 2.8 we can see that the position of the SAXS scattering remains fairly unchanged for the samples heated to 350 ºC. Above that temperature we can see an abrupt shift to smaller q values indicating that the interlayer spacing has decreased. From previous measurements, we know that above 250 °C the quaternary amines on the clays become unstable thereby removing the intercalating agents in the clays.

2.3.3. Thermogravimetric Analysis.

In order to have a better understanding of the chemical processes which occur when the samples are heated, we performed separate step by step TGA measurements of

the PS, PMMA homopolymers, and the inorganic additives, individually and in different combinations. In figure 2.9 we show the TGA data from PMMA with and without the addition of 10 % Cloisite 20A clay. The derivative of the spectra is plotted in the inset, and is useful in visualizing the onset of a vaporization process. In the absence of the clay we find that the PMMA decomposes in two steps. The first decomposition occurs from around 250 °C to 325 °C and then the second decomposition occurs from 350 °C to 450 °C. These two peaks have been previously identified as degradation of the unsaturated end groups followed by the depolymerization of random scission [32-33]. When the clay is added, the first peak is greatly reduced, corresponding to a much smaller fraction of the chains undergoing scission, while a larger peak is observed at T = 397 °C which is higher than the decomposition peak corresponding to the depolymerization of the random scission.

Hence the effect of the clay is to raise the temperature at which PMMA undergoes thermal decomposition. This behavior may be due to the fact that the clay adsorbs strongly to the PMMA surfaces, as was shown by Hu *et al.*[23]. Hence additional energy corresponding to the desorption energy of the chains from the clay surfaces may be needed before vaporization occurs. No effect is expected for PS, where the interactions with the clay surfaces are minimal. In figure 2.10 we show the TGA spectra of a 70/30 weight percent blend of PS and PMMA. The red solid line is a calculated TGA spectrum if the PS and PMMA would go into the vapor phase separately. From the figure we can see that the TGA data for the PS/PMMA blend is different than the calculation, indicating that PS does have a synergistic effect on PMMA, and the two components go into the vapor phase at similar times. We do not yet fully understand the mechanism for this synergy. In particular, since the polymers are immiscible, as is shown in the TEM figures, their phases separate into micron sized domains. In figure 2.10 we show the change in the TGA traces which occurs when the data is obtained from the blend, but now with Cloisite 20A clay added. The green solid line corresponds to the expected trace if all the individual components were to vaporize independently. The TGA data can also be simulated by adding the experimental trace for PMMA/ Cloisite 20A and the independent trace of PS (black solid line). From the figure we can see that this fits the experimental trace of PS/PMMA/Cloisite 20A blend much better than the independent addition of the

three components (green solid line) or the addition of the PS/PMMA experimental data followed by the clay trace (blue solid line). This behavior is consistent with the strong adsorption of clay to PMMA and the observation from the TEM micrographs that the clay is mostly segregated in the PMMA phase. Hence, despite the increased compatibilization and the decrease in the individual domains produced by the clay, the two phases, namely PS and the PMMA/clay combination vaporize individually. This result was quite surprising, given the synergy observed above for the PS and PMMA phase separated blend. In figure 2.11 we plot the TGA data for the PS/PMMA blend when DB is added. Here we see that the simulation which best fits the data corresponds to the PS/PMMA vaporization combined with the separate traces of DB and AO (green solid line). This indicates that the DB does not have any special synergy with either the PS or PMMA, which prefer to associate with each other, rather than with the DB. Examination of the DB distribution in the blend from the TEM image in figure 2.2 clearly shows that no DB is found in the PMMA phase, while very large clusters are observed in the PS phase. This distribution is consistent with the DB being immiscible in both polymers, while slightly preferring the PS relative to the PMMA.

In figure 2.12 we plot the TGA data for the formulation for which Si *et al.*[8] reported a UL94-V0 result. The derivatives of the traces are plotted in the inset. In the absence of clay we can see that the traces have multiple peaks in the derivative plot, indicating that vaporization for the different components occurs at different temperatures and times. Consequently the components of the gas phase reaction may not arrive simultaneously at the sample surface and decompose individually. The trace produced after the addition of clay shows vaporization starts at a lower temperature, but from the derivative trace, we find that most of the sample mass vaporizes at the same time and temperature. This makes the gas phase reaction much more effective and hence may be a possible explanation for the synergy reported between the clays and the DB formulation. This can also be seen in the TEM micrographs, where DB particles are observed within the PMMA domains. Higher magnification images show that the DB is adsorbed to the clay platelets, which in turn forms much smaller aggregates that segregate into the PMMA phase. This kind of mixtures aids the synergy observed in the coordinated vaporization of the components. In figure 2.13 we plot the TGA trace of the PS/PMMA

blend with the FR formulation with and without the addition of 10 % clay. In this case, there are several possibilities for the vaporization process. In the figure we show the calculation for PMMA/Clay/DB/AO plus the PS. This would be a probable mixture since from the TEM images we see that the clay/DB is now concentrated in the PMMA domains which are quite distinct from the PS phase. From the TGA trace though, we find that the agreement, which the PMMA/Clay/DB/AO and the PS are decomposed separately, is poor.

We also experimented with others, less likely combinations such as PMMA/C20A plus PS/DB/AO,(red solid line), PS/PMMA plus DB/AO/C20A(green solid line), PS/PMMA/C20A plus DB/AO(purple solid line), PMMA/DB/AO plus PS/C20A(light red solid line), and individually separated PS/PMMA/DB/AO/C20A (blue solid line). In all cases we can see that, as expected, the agreement is not good. The TGA data indicates that a synergy must exist between the PS and PMMA/clay/FR phases, which produce a distinct sequence of vaporization. Since many components are involved it is difficult to determine a unique sequence of decomposition of the PS/PMMA/DB/AO/C20A polymer blend from these traces. On the other hand, by examining the derivative plots in the insert we find that a large peak occurs in the same region as was observed for the PMMA/DB/AO/C20A combination, and an additional plateau is observed which is stable to 450 °C, or the temperature at which the PS was observed to decompose. As we will show below, this blend also satisfies the UL-94 V0 rating and forms a char upon burning. Hence part of the blend produces an efficient flame retardant vapor phase where DB is consumed, while another part, which is PS rich, the benzene rings of the PS polymer chains may be decomposing more slowly and possibly adsorbing onto the clay surfaces, which we will show later, also help formation of the char.

2.3.4. EXAFS and Mass Spectroscopy.

EXAFS technique examines the solid samples after the volatile gases are removed. In figure 2.14 the data were taken using the Br absorption coefficient, which is related to the interference caused by backscattering in its neighboring atoms and hence is sensitive to the chemical nearest neighbor environment of the Br atoms in the solid phase. In this experiment we only probed the solid samples that remained after annealing for 20

seconds at different temperatures. In each case the data indicate that no change in the nearest neighbor configuration of the DB molecule has occurred, despite the fact that the TGA analysis shows that a large fraction has vaporized at these temperatures. These data are consistent with the established pathways in which the DB reacts with the volatile products in the vapor phase. Hence no observable the changed DB molecule occurs with the addition of the clays. The samples were also examined with mass spectroscopy in order to quantify the amount of Br that remains in the samples after the annealing process. The data for the 70/30 PS/PMMA blends are tabulated in table 2.3. From the data we can see that, for the same annealing times and temperature, the samples with 10 % clay had significantly less bromine than those without clay. These results are consistent with SEM/EDAX analysis of the blend samples after annealing for different times at 650 °C in a tube oven. The images for Br mapping are shown in figure 2.15, where we can clearly see that the amount of Br remaining in the solid phase decreases more rapidly in the samples with clay, such that after annealing for 15 sec. no Br is discernable in the clay samples, while a significant amount still remains in the samples without clays. Hence the elemental mapping, TGA, and mass spectroscopy indicate that the addition of clay enhances the vaporization rather than retard vaporization.

2.3.5. Cone Calorimetry.

The heat release rate (HRR) and mass loss rate (MLR) of these polymer blends were measured using cone calorimetry. In order to separate the effects of thermal decomposition and combustion, we first studied the thermal response of the PS/PMMA blends when heated under nitrogen atmosphere in the controlled atmosphere cone calorimeter at NIST. The MLR data are shown in figure 2.16, where we can see that the values for the sample without clay increase rapidly and then abruptly drop to zero within the first 300 seconds. The shape of the curve for the sample without clay is consistent with the rapid unzipping of the PMMA molecules superimposed on the decomposition of the PS polymer. This is a typical feature of MLR in pure polymer resins, where char is not produced during the exposure to the heat source and the HRR and MLR increase and then drop abruptly when the material is completely consumed. When the clay is added, the onset temperature of decomposition remains unchanged but the MLR of the blend

with 5 wt % clay is seen to decrease by nearly a factor of two and the decrease is only somewhat larger when 10 % clay is added. The MLR has a relative plateau till about 140 sec, at which point the decrease becomes steeper. The addition of clay seems to have the largest impact in this region where the rate of decrease is inversely proportional to the clay concentration. This behavior is consistent with two regions in the mass loss rate: (1) a non-charring region, where the net heat flux determines the mass loss rate. (2) A region where char begins to form and the mass loss rate is controlled by the rate of char formation. This behavior is characteristic of polymer/clay nanocomposites, where the clay was either intercalated or exfoliated [8, 34-36]. Since the sample was mounted on an insulated load cell which prevented heat and mass loss from the bottom of the loaded cell we can model the thermal behavior using a one dimensional transient burning equations. Quintiere and co-workers [38-39] proposed a relationship between mass loss rate and the net heat flux;

$$\dot{m}'' = \frac{\dot{Q}''_{net}}{L_g/(1-y)} \qquad (1)$$

, where Q''_{net} is the net surface heat flux into the surface (note: double prime signifies per unit area). It is composed of an external heat flux, a flame heat flux, and a re-radiation from the surface. □" is the mass loss rate per unit the surface area of volatiles, L_g is heat of gasification, and 1-y is a fraction of char residue. Since the PS/PMMA blend is non-charring the mass loss rate increases with increase of the net heat flux as shown in figure 16, where only an net heat flux without flame heat flux exists in the inert gas condition. Hence the slope, 1/Lg, when the char yield is zero in the equation, can be regarded as degree of flammability. Moreover, in the figure we can see the slope slightly changes around 100 sec. This indicates that there could be the two different heats of gasification involved in the decomposition of the PS/PMMA blend. Hence some of PMMA first vaporizes and then PS and the rest of PMMA volatilizes into gas phase when the vaporization surface, which is continuously decomposing down to the bottom of the loaded sample, exists in the one-dimensional steady state burning. In the figure, although there is one small dips around 100 sec. in case of the blend with the addition of clays, which may be caused by a initial char formation, it is seen that there are two different

slopes until the mass loss rate starts decreasing around 150 sec. The two different slopes are an evidence of the fact that the blend is partly compatibilized by the addition of clays.

The two distinct slopes are also consistent with the TGA traces of PS/PMMA/Clay, where proposed scenario to vaporization of PS and PMMA/Clay separately. After reaching the peak MLR in the polymer blends with the clay, where physically the surface of the sample in the blend is covered by a protective layer composed of clay platelets and carbonaceous char, mass loss rate continuously decreases even though there is somewhat a constant region of mass loss rate in both the 5 % clay case and the 10 % case. In particular, the mass loss rate in the 5 % clay case occurs from 250 sec. to 370 sec. The constant region could be caused by a result when the amount of char yield becomes constant in the equation. These distinct regions also appear in PS/PMMA/C20A under the air condition, which is shown in the figure 2.17. In the figure 2.17a PS/PMMA polymer blend is flammable enough to completely burn away, releasing the highest the peak heat release rate (PHRR), 1507. 8 kW/m^2 observed in this study. However, addition of 10 % clay reduced the peak HRR of this composition to 563.1kW/m^2 which occurs after 75 seconds. The same observation of reductions happens in its mass loss rates (MLR) as shown in figure 2.17b. Hence it is believed that the clays intercalated in pure polymer blends play an important role in the changes of HRR and MLR either in the inert gas or air condition.

Furthermore, in order to demonstrate an effect on HRR and MLR when the clays are combined with the conventional FR particles, cone calorimetry was conducted in the air condition. Data are summarized in table 2.4. In the figure 2.17a addition of 13 % FR particles reduces as much as half of the PHRR in the virgin polymer blend, and even more reduction with the addition of 19 % FR particles in the blend. It is common that the FR particles are decomposed into hydrogen halide at the gas phase so that the volatile products of incomplete combustion, such as soot and CO, release in the phase [40]. In the figure these exothermic reaction with oxygen in air are dominant at time just after ignition is shown by heat release, which leads to a big reduction in the HRR. This reduction of HRR can be explained using χ, gas-phase combustion efficiency since flame heat flux is involved in air condition. Tewarson *et al.*[41] proposed that when incomplete

combustion products are released into the gas phase, there is an efficiency reduction in the net heat flux. Hence the heat release rate is described as:

$$HRR = \chi(1 - Y)\frac{H_c}{L_g}\dot{Q}''_{net} \quad (2)$$

,where H_c is heat of combustion and χHc/Lg is defined as the heat release parameter (HRP). This expression depends on the combustion efficiency and the char yield because the mass loss rate is directly proportional to HRR in a steady state burning. Although the reduction of HRR is observed in the blend with FR particles, it is interesting that the addition of the FR particles in the blend does not change its MLR during combustion, and even slightly higher peaks are seen with PS/PMMA/DB/AO compared to PS/PMMA polymer blend, as is shown in the figure 2.17. Hence in the equation HRR decreases with increase of the halogen FR particles because the halogen particles produce incomplete volatile products and char yield is increased insufficiently. Furthermore, there is a difference in the PMMA homopolymer system, where was shown in the previous paper that there was some reduction on MLR in that polymer system [8]. This may be explained by the TGA curves, where the PMMA decomposes with the FR particles separately at different times and temperatures.

In order to obtain an elimination of PHRR of the PS/PMMA/DB/AO composites, combining the FR particles with the clays could be a method. In the figure 2.17a the PHRR exists at 721.0 kW/m^2 in PS/PMMA with 10 % DB and 3 % AO composite and then the PHRR is eliminated after addition of 5 % clay in the system. This tendency also occurs in the PS/PMMA with 15 % DB and 4 % AO when 10 % clay is added. However, it is not enough for 3 % clay in the polymer blend to achieve the UL-94 V0, in spite of a huge reduction of its HRR. Another important observation regarding the HRR of PS/PMMA/DB/AO/C20A nanocomposites is that it is clearly seen to have a plateau of HRR. Furthermore, the length of the plateau mainly depends on the amount of clay in the polymer blend. This dependence may be explained by a fact that the net heat flux is consumed to volatilize the FR particles into the gas phase, while the char yield is constant, which means that in the equation the average HRR could be determined by the HRP, where ratio of the heat of combustion to heat of gasification is constant when the

efficiency is a known parameter. In the figure 2.17a it may be confirmed by the fact that a small plateau appears in a very beginning part after ignition in PS/PMMA/C20A and then it disappears around 75 sec., at which point is that the ratio is constant when the amount of char production changes during combustion. This is also really seen in MLR of polymer blends with the clay. The only difference between PS/PMMA/C20A and PS/PMMA/DB/AO/C20A on MLR and HRR is a magnitude, which is seen in the figure 2.17a that the magnitude of the HRR of PS/PMMA/C20A is higher than that of the HRR of PS/PMMA/DB/AO/C20A overall combustion time. However, the magnitude of the MLR in PS/PMMA/C20A is lower than that of the MLR of PS/PMMA/DB/AO/C20A, which can be explained by a synergy of the combination FR particles with clays, which is seen in the equation that the HRR is reduced when there is an increase of FR particles and char formation.

On the other hand, in the case of PC/SAN24 polymer blend, although the clays in the blend with the halogen compound cause a good distribution of the FR compound and obtain in good compatibility, the same effect on removal of the peaks in HRR and MLR does not occur at the blend during combustion, which is shown in figure 2.18. A reason of this result may be explained by the fact that the surfactants in the clay hinder the chain scission process of PC, which otherwise would lead to the high production of chars during combustion [40]. In figure 18a, the adding 5 wt % of Cloisite 20A reduced the PHRR from 516.90 to 390 kW/m^2. It is believed that this effect is not contributed by addition of clays but the breakdown products of DB in the gas phase. It is a good agreement with the fact that the MLR showed in figure 2.18b that the clays did not affect the reduction of MLR.

2.3.6. Analysis of Chars.

Characterization of structures of char formation was conducted after decomposition in N_2 and combustion in air since many research groups reported a barrier effect formed from the decomposition of the clay layers, which had been intercalated and/or exfoliated in the matrix.[34-36, 9, 43-46] In order to investigate the effect of char formation on MLR and HRR, in figure 2.19 we first studied the residues from PS/PMMA with 5 % and 10 % clay after the decomposition in the inert gas atmosphere. In figure

2.19a and 2.19b the residue of 10 % clay has fewer cracks compared to that of the 5 % clay. This result is consistent with the previous result reported by Si *et al.*[31], where more segregation was observed with increase with the amount of addition of clay. Furthermore, both residues cover over the whole sample surface in the aluminum sample holder, which leads to the reduction on MLR and HRR. This reduction may be explained by the interruption of diffusion of heat flux caused by the barrier effect from char formation. Actually, Kashiwagi *et al* [34] studied the relationship between amount of residues and their structures, which was seen to explain the flame retardant mechanisms. In particular, he found that the clay platelets were accumulated on the sample surface during decomposition in the nitrogen condition, which could be explained by mass transportation of the clay platelets in polyamide 6 matrix. This was further studied by Tang *et al.* [45, 47] where the exfoliated clay could migrate into the surface of the nanocomposite at the beginning of decomposing temperatures. Although the mass transfer is essentially necessary to make appropriate barriers on the surface of the samples, it does not provide enough explanation of how a self-extinguishing nanocomposite is achieved in our system. Therefore, we believe that a major factor of obtaining self-extinguishing may be a dependence on relationship between evolution of the clay and physical structures of the residues during and at the end of combustion. In order to demonstrate the relationship, we gathered and scrutinized the residues after combustion in the cone calorimeter.

In the figure 19 % FR agents is much left in carbonaceous char, which are black particles seen in the aluminum sample holder, compared to the resides of 13 % FR agents or the blend with the FR agent. In figures 2.19c-e the amount of residues without the clay is not enough to cover the surface of the samples. On the other hand, in figure 2.19f-h the residues with the clay appear to be well-established char, which are composed of clay platelets and a little carbonaceous chars. It is believed that increasing amount of the clays could make the polymer matrix stiffer. This fact may explain that during combustion, more cracks occurred on the surface, as more was clay added. In addition, there may be a pathway to emit reaction products from interaction the FR particles and the clay. In contrast, the low flammability of the PC/SAN24/DB/AO blend with and without clay could be determined by their residues, which is shown in figure 2.19i and 2.19j. Hence it

is believed that char formation is an essential ingredient to elucidate the mechanism of the self-extinguishment of the nanocomposite. However, a more important factor in understanding the mechanism is the effect on MLR and HRR when the clay is added in terms of the dynamic relationship between microstructures in the system and char formation in condensed phase. Hence further study follows in the discussion section.

2.4. Discussion

In figure 2.20 we show SEM images following cone calorimetric combustion, in air, of two residues, (a) PS/PMMA/DB/AO and (b) PS/PMMA/DB/AO/C20A, where the latter corresponds to the compound that passed the UL-94-V0 criteria. If we compare the two images we find that the appearance of the carbonaceous chars is similar, except that in the case of the flame retardant formulation, the surfaces of the char are covered with clay platelets. This is consistent with previous models where it was proposed that clays retard the HRR and the MLR by migrating to the sample surface and modifying the heat transport properties [34, 44-47].

In figure 2.20b we show a high resolution image corresponding to the area outlined in figure 2.2b, where we can see the details of the clay platelets morphology. From the figure (circles) we can see that many of the clay platelets are bent and some have even formed what appears of be short hollow nanotubes. In contrast, we show in figure 2.20c the SEM image of the char obtained from gasification of a PS/Cloisite 15A nanocomposite. Here we also see the clay platelets on the surface, but the platelets look flat and not bent. This observation is also consistent to the appearance of the clays prior to burning. In homopolymer nanocomposite the clays were highly oriented along the shear direction [20]. Hence they remain flat in the char, after the polymer has degraded. From figure 2.2 we showed that in blends the clays were mostly segregated to the polymer interfaces and remained there despite the large shear imposed in the Brabender. In this case, the heat capacities and the thermal energies can differ greatly between the polymers in the two phases. This can create large local thermal gradients across the two surfaces of the clays, resulting in additional curvature of the platelets towards the softer of the two phases (see illustration 2.2). In contrast, the thermal properties of the matrix are uniform in the case of the homopolymers and no local gradients are formed which would produce curvature of the otherwise rigid platelets.

Another source of structures in the char is the agglomeration of the clays into the long ribbons, which were previously reported by Si *et al*. to form at the decomposition temperature of the di-tallow surfactants coating the clays [20]. In order to determine if these structures also formed in the polymer/clay blend nanocomposites with progressive

heating, a series of TEM images were obtained in for a blend of PS/PMMA with 5 % of the clay, that was annealed at 300 °C, 450 °C, and 500 °C for 5 min and 550 °C for 3 min. The results are shown in the TEM images of figure 21, where we can see that after annealing at 300 °C the clays began to form small tactoid structures. This result is in a good agreement with the SAXS at 300 °C, which are d_{001} = 3.91 nm and d_{002} = 1.95 nm in Figure 2.22. However, the tactoid structures became weaker as the temperature increased up to 450 °C, having a long tactoid line left in the TEM image at that temperature. It may be explained by the fact that the second peak becomes smaller and smaller. At 450 °C the second peak almost disappeared. As temperature increases higher, the long tactoid lines disintegrates into a lot of small pieces of the stacked structure, which are shown in the figure TEM image at 500 °C and 550 °C. Since these ribbons can be several microns in length and since they are formed equally in homopolymers and blends, they are probably not the source of the much smaller tube-like structures observed.

On the other hand, since these very long ribbons can form networks scaffolds to support the hot polymer matrix, they may cause a change in specific heat (C) of the system the during combustion. For example, they can lower the local temperature by more efficient heat dissipation across the sample. We therefore propose an internal energy equation, which is required to vaporize unit mass. Since we showed that there could be two different heat of gasification, hence the total heat of gasification may be expressed as:

$$L_g^{Total} = L_g^A + L_g^B \quad (3)$$

,where the total heat of gasification is a sum of heat of gasification of each component in a system. Due to the fact that heat of gasification equals to a sum of internal energies this equation can be replaced by the equation:

$$L_g = \sum \left[\int_{T_0}^{T_m} C_s \, dT + \Delta H_m + \int_{T_m}^{T_v} C_m \, dT + \Delta H_v + \int_{T_0}^{T_v} C_Y \, dT \right] \quad (4)$$

, where C_s is a specific heat of solid, C_m is a specific heat of an intermediate state, such as a molten solid. T_m is a temperature of melting or decomposition, T_v is a temperature of vaporization, and T_o is an ambient temperature. ΔH_m is heat of melting or decomposition and ΔHv is heat of vaporization. C_Y is a specific heat of charring, which is a new factor in this internal energy equation and could be dependent on the morphology of charring. Therefore, this equation can be applied to the polymer blends in our study. Tewarson *et al.* [41] found that PS mainly combusts as a liquid surface, while PMMA burns as a solid surface. This means that PS needs more the internal energy than PMMA does. He determined that the heat of gasification of PS was slightly higher than that of PMMA. Therefore, according to the equation (1) of mass loss rate above this can explain that the first part of the slope (1/Lg) belongs to PMMA and the second part of the slope is PS in regard to the MLR and the HRR because the mass loss rate is inversely proportional to the heat of gasification. Another interesting aspect is that the last term in the internal energy equation is contributed from charring. In our study the charring is mainly caused by the addition of clay. As shown in the TEM and SEM images above, a clay platelet could be formed in a tubular-like rod as temperature increases, which may be inferred that the specific heat of the clay platelet changes as the temperature rises. Hence the change of the specific heat of the clay platelet can affect on thermal diffusivity in the equation below:

$$\alpha \approx \frac{\kappa}{\rho(C_{clay\ platelet} + C_{carbonacous\ char})} \qquad (5)$$

, where α is thermal diffusivity, κ is thermal conductivity, ρ is density, $C_{clay\ platelet}$ is the specific heat of clay platelet, $C_{carbonecous}$ is the specific heat of carbonaceous char. In the equation, when κ and ρ are constant, thermal diffusivity is directly proportional to $1/(C_{clay\ platelet} + C_{carbonecous\ char})$. Hence the addition of clay can decrease more the thermal diffusivity compared to the case without clay. This is confirmed by a result of specific heat of residues of PS/PMMA/DB/AO and that of PS/PMMA/DB/AO/Clay. In Figure 2.23, C for the system with the clays is always higher than that of the system without the clays over all temperatures, which means that the clays act as heat sinks. Moreover, If $C_{clay\ platelet} \ggg C_{carbonecous\ char}$, $\rho C_{clay\ platelet}$, the volumetric heat capacity, could be

determined by a thermal expansion term. Si *et al*. proposed that a volume of a domain in the blend surrounded by the clays could be described as:

$$V \approx m(2rl^2) \tag{6}$$

,where m is a number of clay platelets in a domain, r is a radius of the domain, and l^2 is the surface area of a clay platelet. If we assume that only one clay plate would be surrounded along the interface in a domain, the volumetric heat capacity can be expressed as:

$$\rho C_{clay\ platelet} \approx \Delta V \approx A_{\text{clay platelet}}(2rl^2)\Delta T \tag{7}$$

,where, $A_{\text{clay platelet}}$ is a typical thermal expansion coefficient of the clay platelet. In this expression, the radius of a domain could be inversely proportional to the temperature difference. Therefore, when the temperature difference is constant, the radius of the domain decreases as the clay platelet is formed into a nanotube-like rod because PMMA inside the domain decomposes away as the temperature goes up. It could lead to decrease of the volumetric heat capacity, which could increase the thermal diffusivity. In the figure 2.16 this relationship could have an impact on the slopes of MLR after around 350 sec., where the slope of 5 % clay is higher than that of 10 % clay. Hence the blend with 5 % clay could burn away rapidly compared to the 10 % clay in the blend. This result may be contributed to a formation of a network structure with the tubular-like rods. In spite of the fact that 5 % clay and 10 % clay both produce the ribbon-like and tubular-like structures, which are shown in figure 2.24, the blend with 5 % clay may not form enough of the structures to produce an effective heat conducting network.

2.5. Conclusion

We have shown that the addition of nanoclays is also effective at enhancing the flame retardant properties of polymer blends. In the case of PS/PMMA blends, we have shown that addition of Cloisite 20A greatly enhances the dispersion of the FR agent, which becomes adsorbed onto the clay platelets. Hence the clays prevent thermally induced phase segregation and disperse the flame retardant. As a result, the blend of PS/PMMA/DB/AO/Cloisite 20A is able to pass the UL-94-V0 test. For the PC/SAN/DB/AO/Cloisite 20A nanocomposite, addition of the clays did not enhance the flame retardant properties. In this case, the relative attraction of the FR formulation for the clay surface was larger than that of the polymers, and hence the FR coated platelets were not as efficient in compatibiliziang the blend, as the platelets in the nanocomposite which did not contain FR.

The thermal behavior of these blends was also studied. TGA measurements indicated that the thermal decomposition of the blends was not a simple superposition or addition of the decomposition behavior of the two polymers. Addition of clay to the PS/PMMA blend caused all the individual components to vaporize at the same time. This coordination of the combustion time appears to be crucial in imparting flame retardance with halogenated formulations. Since the FR chemical reactions are in the gas phase, all the components must enter the gas phase simultaneously for optimal efficiency. These results indicate that the clays may be catalyzing the decomposition of the halogenated FR agent.

The internal structure of the clays was studied by obtaining cross sections from a sample that was annealed for 3 minutes in a tube oven at different temperatures, ranging from 250-550 °C. From the TEM images we can see that when the temperature exceeds 400 °C, the functional groups desorb from the surfaces and then the clays coalesce into long fibers. The desorption is confirmed by SAXS, where the characteristic x-ray peaks of clays disappear at $T < 250$ °C, where the clay is dispersed. As the temperature increase pass 300 °C the charactering peaks of clays re-appear, indicating that the exfoliation is reversing.

Examination of the chars, using SEM, revealed unusual features where the clay platelets were folded forming short nanotubes. The folding of the clay platelets is induced by differential thermal response between the two polymers phases across the interfacial regions where these platelets are segregated. Some of these platelets are so tightly folded that they resemble Halloysite, a naturally occurring, tube-like clay formations. These "nanotubes" do not appear to have any special function in the flame retardant properties. On the other hand, examination of the nanocomposite after heating to 550 °C shows that long ribbon like aggregate structures, approximately 100 nm in width, consisting of multiple clay platelets, have begun to form. These ribbons can now form an entangled network within the char, similar to the one reported for carbon nanotubes, which may improve the mechanical properties and the thermal diffusivity. A model is presented that brings together the two most important elements, the thermal diffusivity and the simultaneous vaporization, to explain the observed synergy.

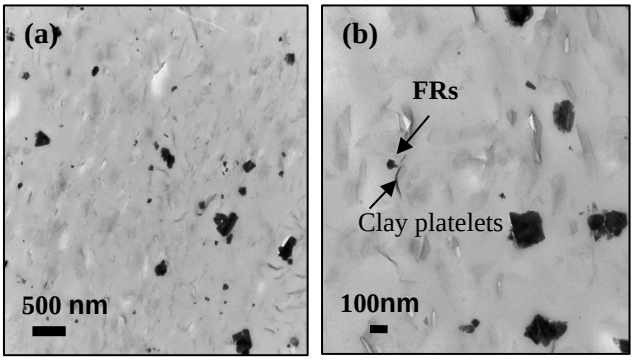

Figure 2.1. TEM images: (a) PMMA/DB/AO/Cloisite 20A (75/20/5 wt%), (b) PMMA/DB/AO/Cloisite 20A(70/20/5/5 wt%).

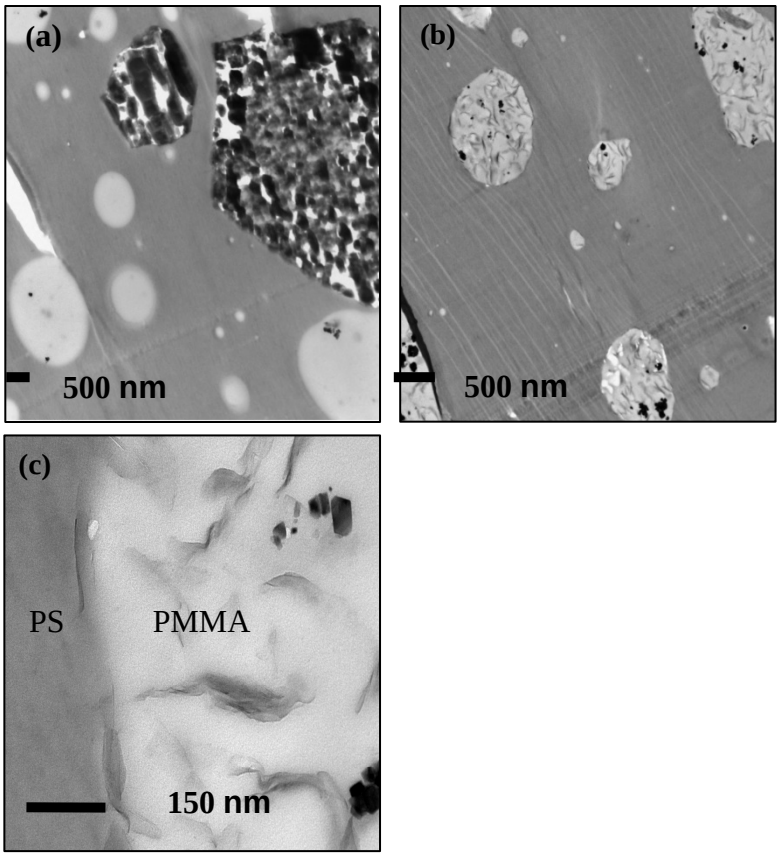

Figure 2. 2. TEM images: (a) PS/PMMA/DB/AO (70/30/15/4 wt%), (b) PS/PMMA/DB/AO/Cloisite 20A(70/30/15/4/5 wt%), High Magnification; (c) PS/PMMA/DB/AO/Cloisite 20A(70/30/15/4/5 wt%).

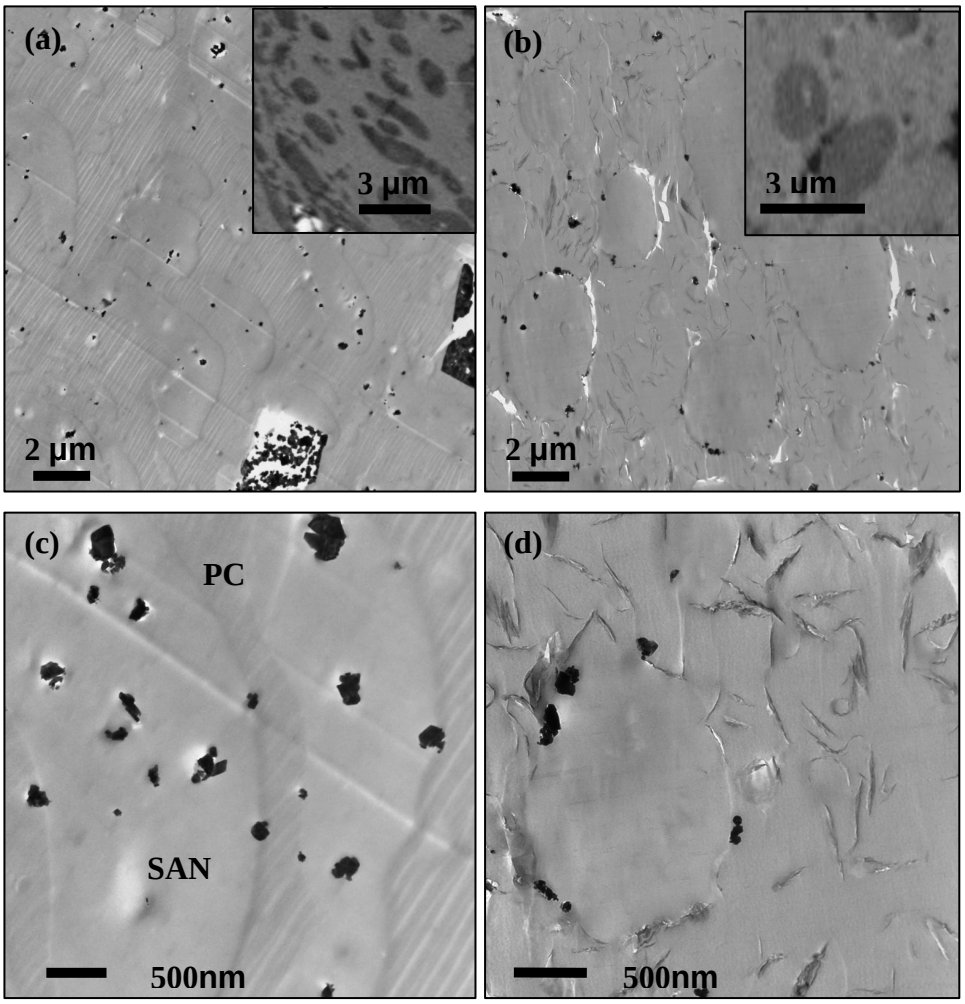

Figure 2.3. Scanning transmission X-ray microscopy (STXM) images; taken at 286.8eV, the absorption of the energy of SAN24, SAN24 is dark, which is shown in the inserted images. TEM images: (a) PC/SAN24/DB/AO (50/50/15/4 wt%) and (b) PC/SAN24/DB/A0/Cloisite 20A (50/50/15/4/5 wt%). High Magnification: (c) PC/SAN24/DB/AO (50/50/15/4 wt%) and (d) PC/SAN24/DB/A0/Cloisite 20A (50/50/15/4/5 wt%).

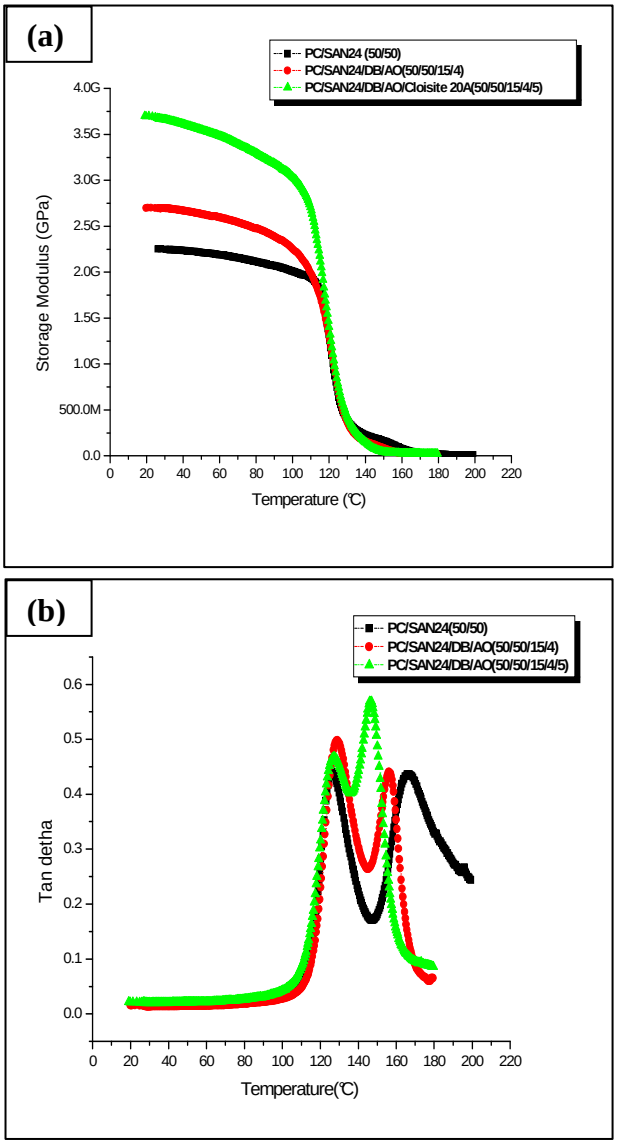

Figure 2. 4. (a) Storage modulus and (b) Tan delta in PC/SAN24 (50/50 wt%), PC/SAN24/DB/AO (50/50/15/4 wt%), and PC/SAN24/DB/AO/Cloisite 20A (50/50/15/4/5 wt%).

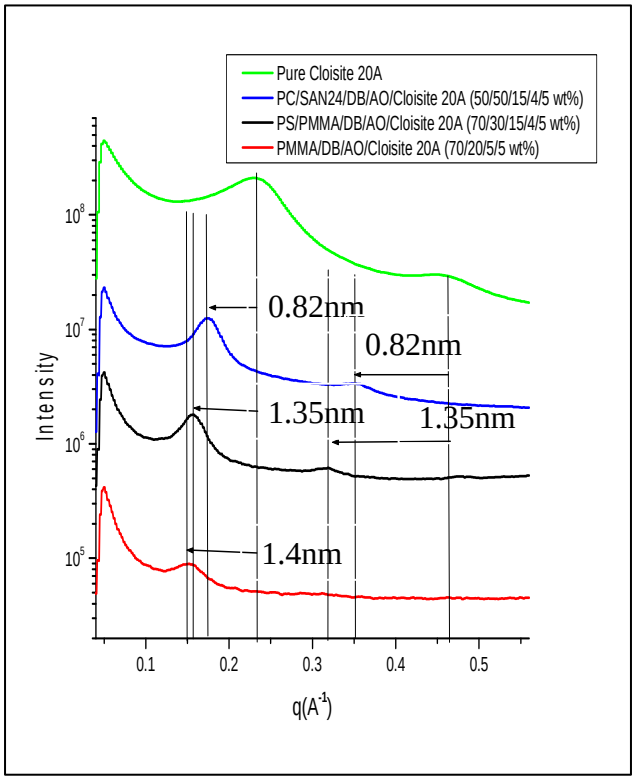

Figure 2. 5. SAXS spectra of pure Cloisite 20A-(green line), PC/SAN24/DB/AO/Cloisite 20A (50/50/15/4/5 wt%)-(blue line), PS/PMMA/DB/AO/Cloisite 20A (70/30/15/4/5 wt%)-(black line), and PMMA/DB/AO/Cloisite 20A (70/20/5/5 wt%)-(red line).

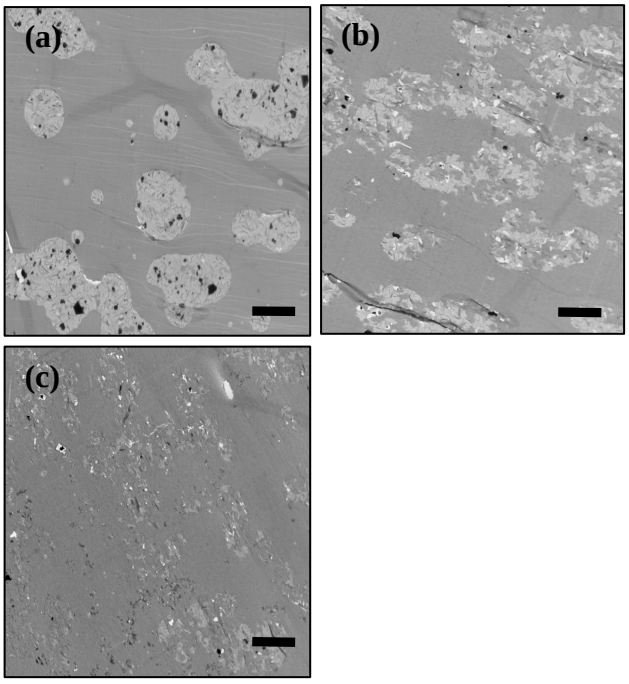

Figure 2.6. Low resolution (4800x) TEM images of a series of burning Bar (a)-Top, (b)-Middle, (c) -Bottom of PS/PMMA/DB/AO/Cloisite 20A(70/30/15/4/5 wt%). (scale bar = 2 μm).

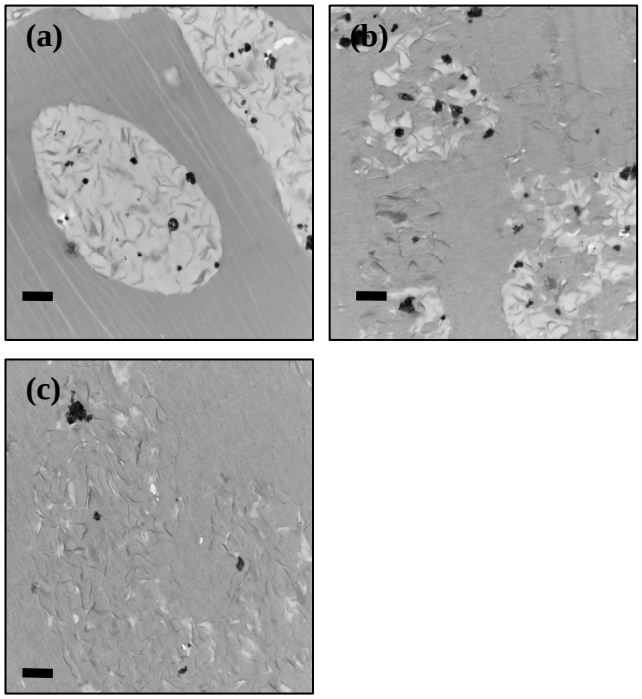

Figure 2.7. High resolution (18500x) TEM images of a series of burning Bar (a)-Top, (b)-Middle, (c)-Bottom of PS/PMMA/DB/AO/Cloisite 20A(70/30/15/4/5 wt%). (scale bar = 500 nm).

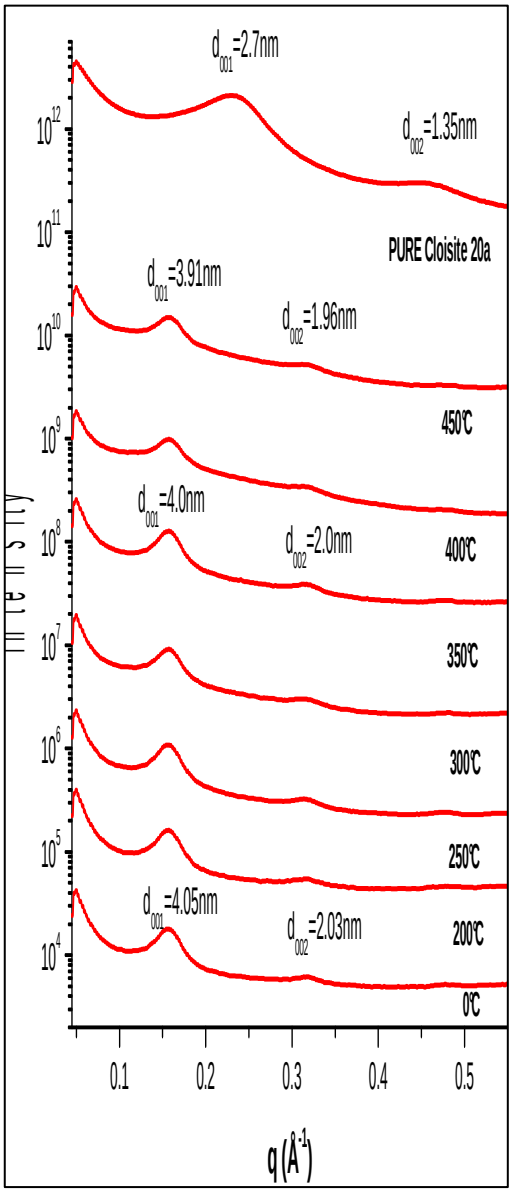

Figure 2. 8. SAXS data of PS/PMMA/DB/AO/Cloisite 20A (70/30/15/4/5 wt%) as a function of temperature.

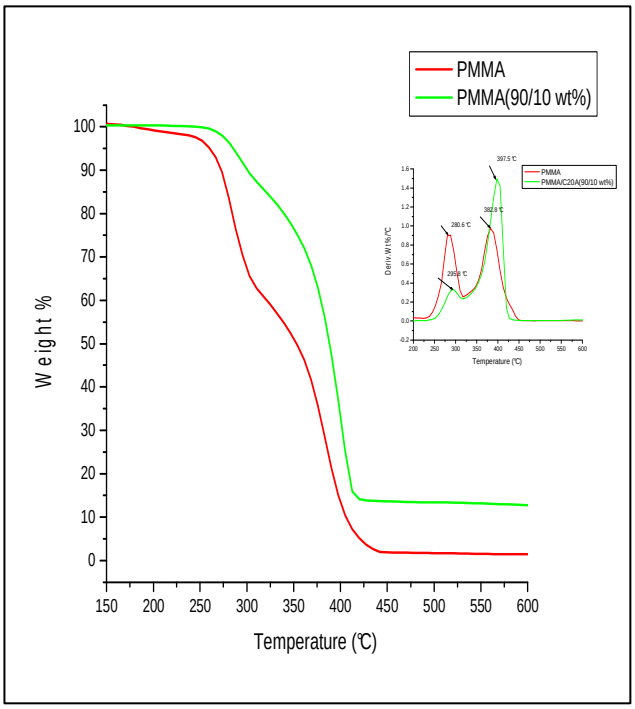

Figure 2. 9. Curves of TGA and DTG (an insert image) as a function of temperature from PMMA and PMMA/Clay nanocomposites.

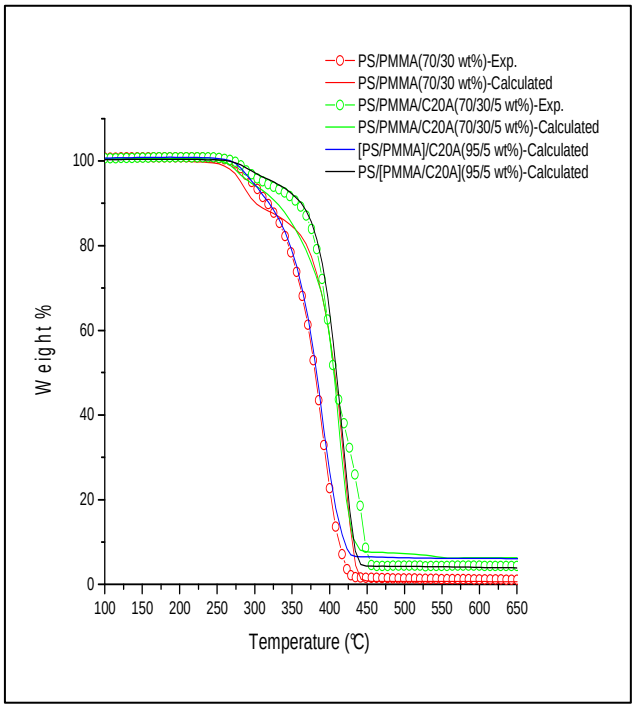

Figure 2. 10. Experimental and calculated curves of TGA from PS/PMMA and PS/PMMA/Clay nanocomposites.

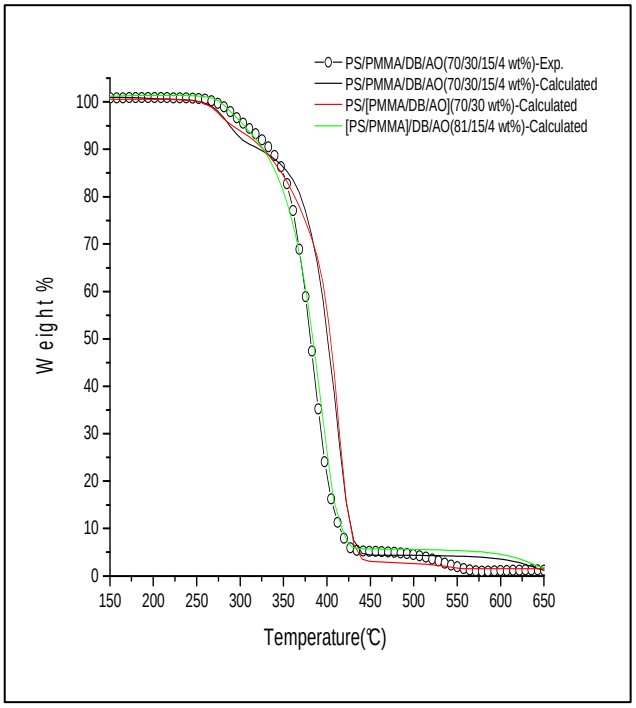

Figure 2. 11. Experimental and calculated curves of TGA from PS/PMMA/DB/AO Nanocomposites.

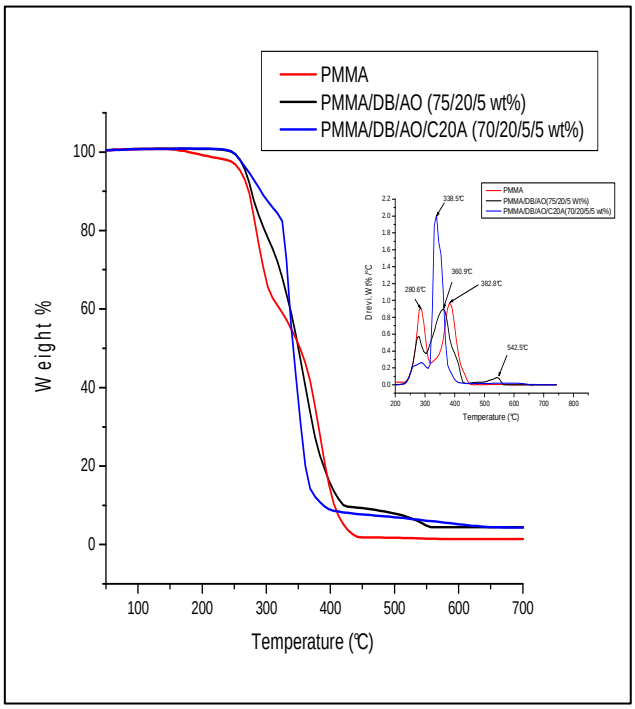

Figure 2.12. Curves of TGA and DTG (an insert image) as a function of temperature from PMMA and PMMA/DB/AO without and with clay nanocomposites.

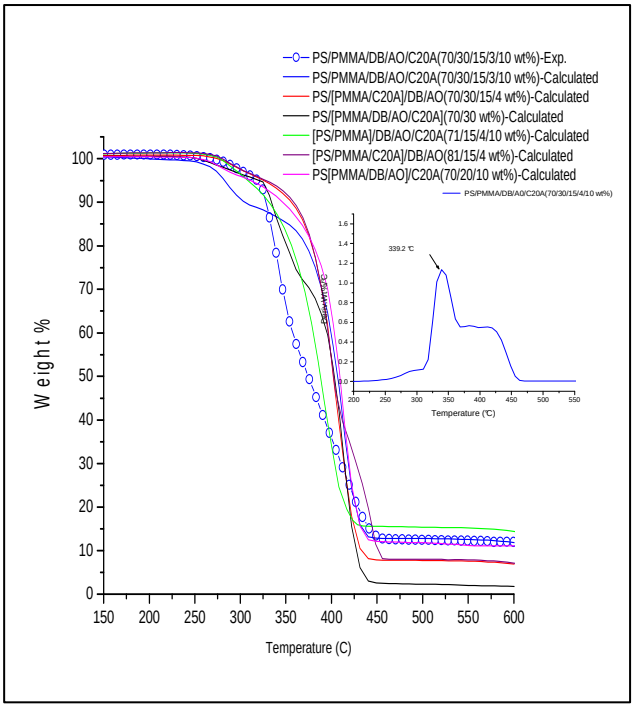

Figure 2.13. Experimental and calculated curves of TGA from PS/PMMA/DB/AO/C20A nanocomposites and DTG (an insert image).

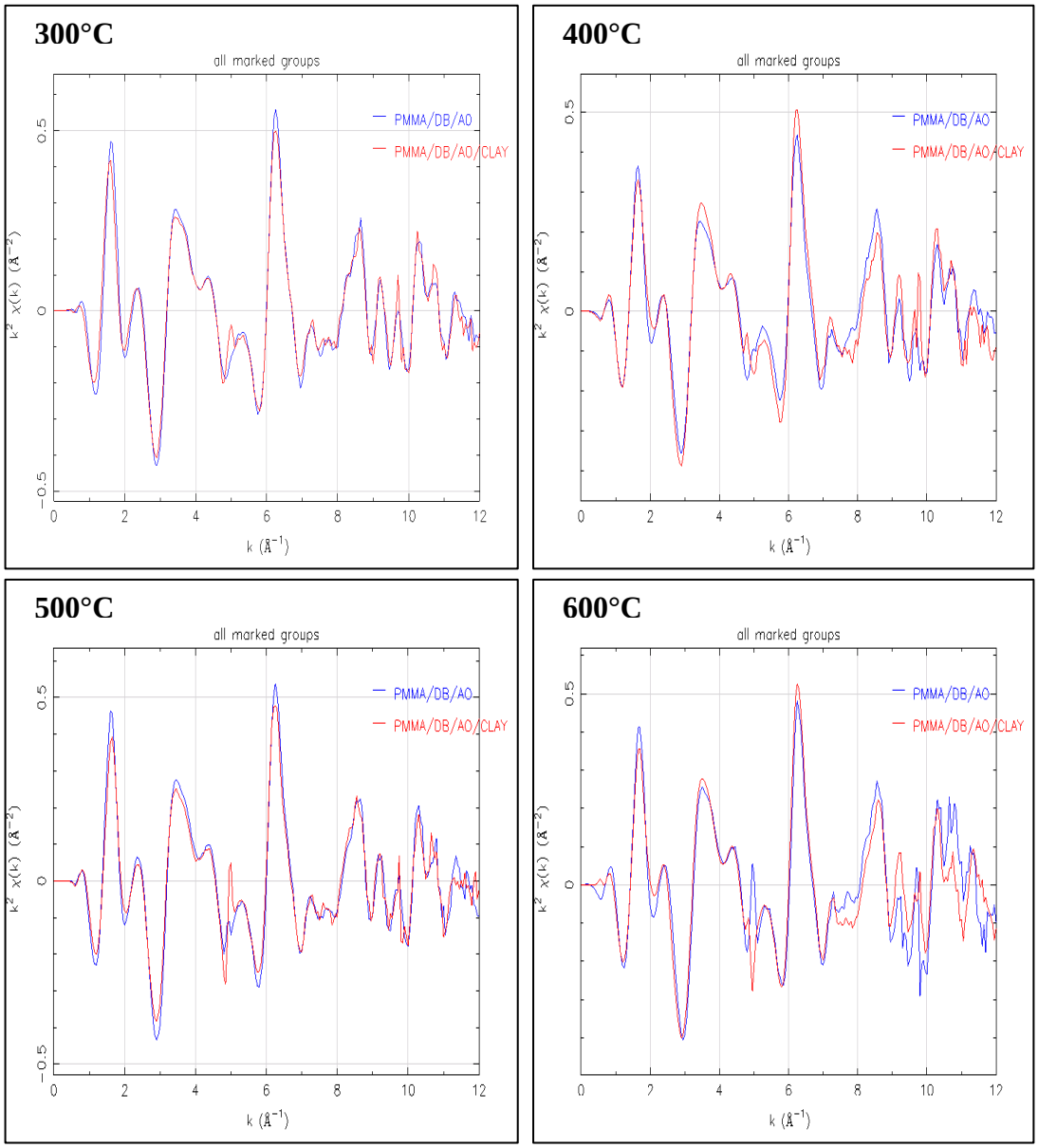

Figure 2.14. EXFAS data of Br particles in PMMA/DB/AO (70/20/5 wt%) burnt samples without or with Cloisite 20A(5 wt%) as a function of temperatures.

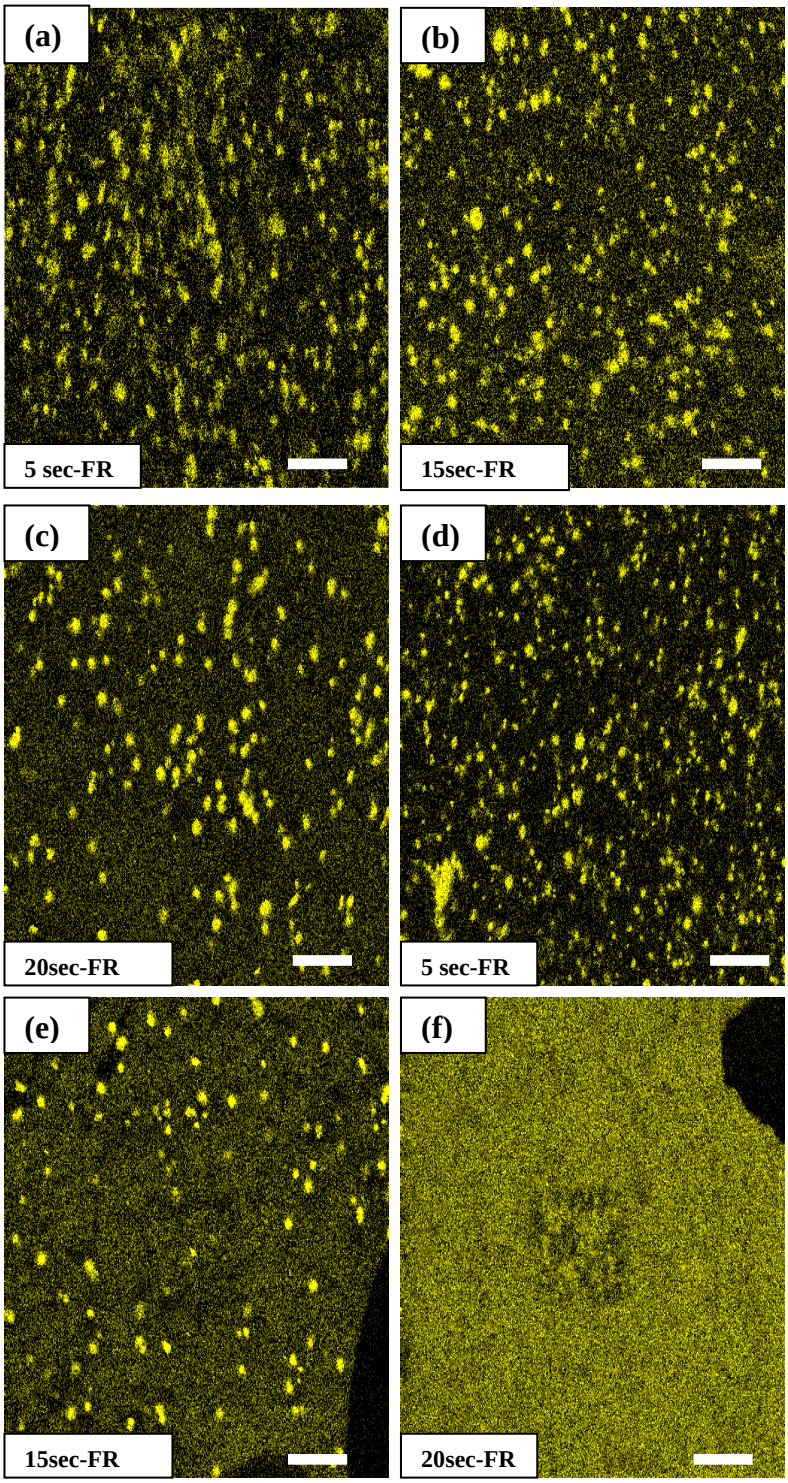

Figure 2.15. Maps of Br particles (yellow dots) in a series of burning time at 650 °C in the oven: (a)-(c) from the PS/PMMA/DB/AO(70/30/15/4) samples, (d)-(f) from PS/PMMA/DB/AO/Cloisite 20A (70/30/15/4/3) samples. (scale bar = 2 µm)

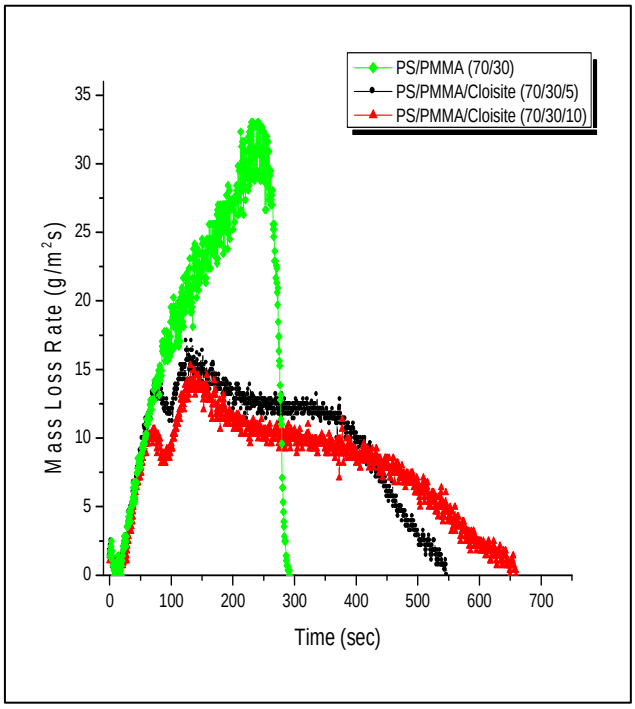

Figure 2.16. The effects of addition of Cloisite 20A on MLR of PS/PMMA at 50KW/m2 in nitrogen.

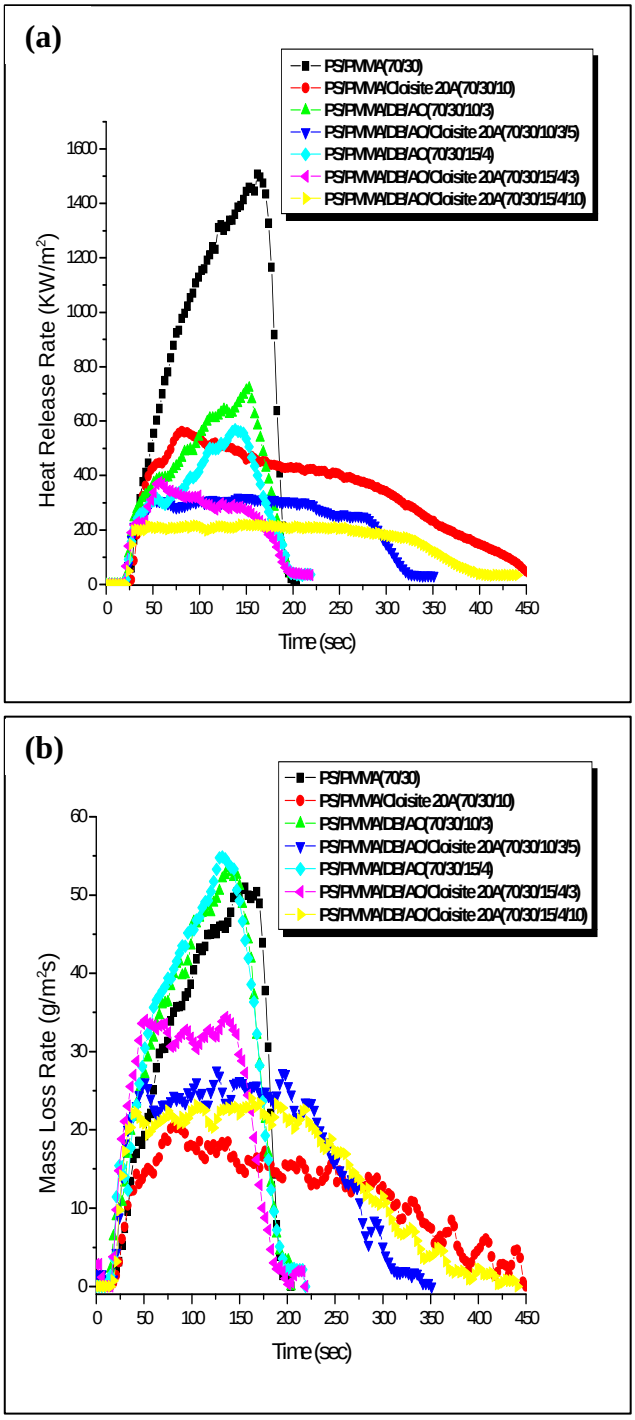

Figure 2.17. The effects of addition of DB, AO and Cloisite 20A on HRR(a) and MLR(b) in PS/PMMA/DB/AO at 50kW/m2 under air.

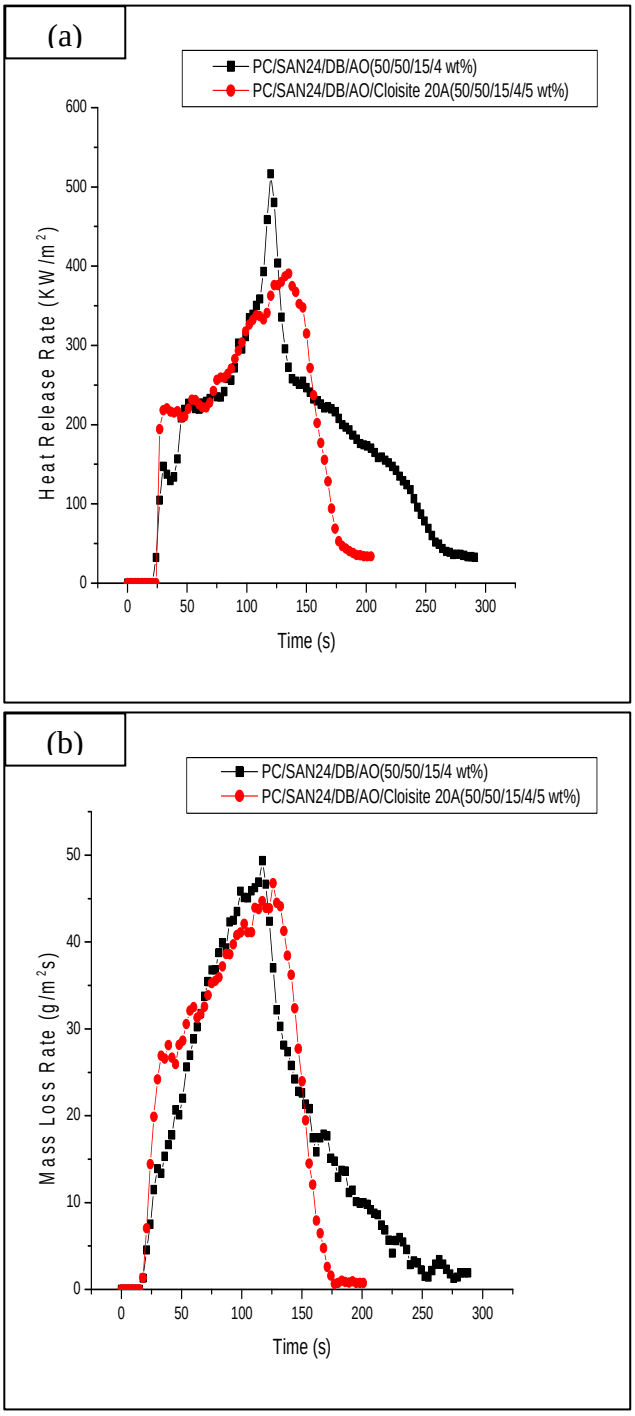

Figure 2.18. The effects of addition of DB, AO and Cloisite 20A on HRR(a) and MLR(b) in PC/SAN24 at 50KW/m2.

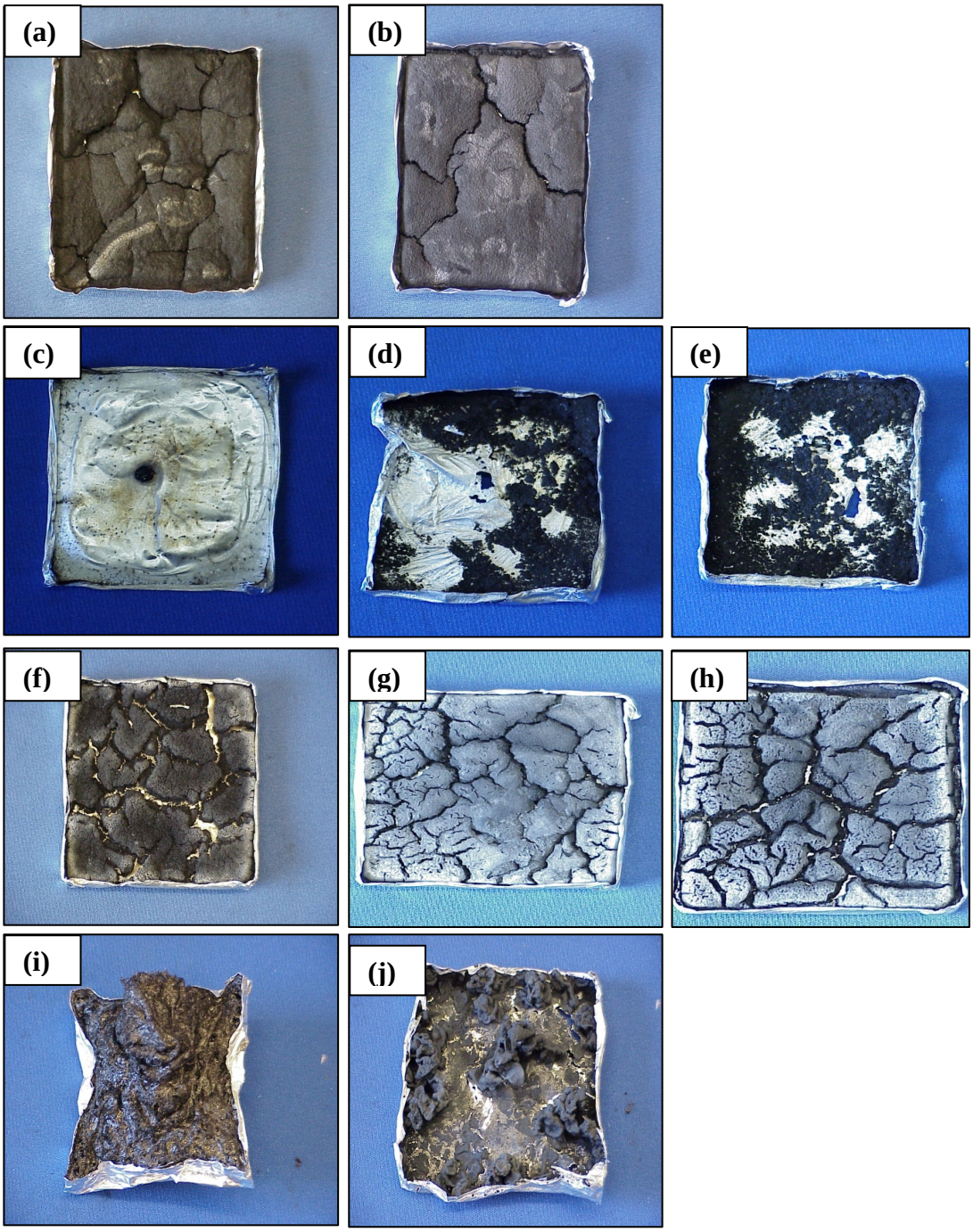

Figure 2.19. Images of residues after cone calorimetry under N2 : (a) PS/PMMA/C20A (70/30/5 wt%), (b) PS/PMMA/C20A(70/30/10 wt%); The images of residues after cone calorimetry under air: (c)PS/PMMA(70/30wt%),(d)PS/PMMA/DB/AO(70/30/10/3wt%),(e)PS/PMMA/DB/AO(70/30/15/4wt%),(f)PS/PMMA/DB/AO/C20A(70/30/15/4/3wt%),(g)PS/PMMA/DB/AO/C20A(70/30/10/3/5wt%),(h)PS/PMMA/DB/AO/C20A(70/30/15/4/10wt%),(i)PC/SAN24/DB/AO(50/50/15/4wt%),and(j)PC/SAN24/DB/AO/C20A (50/50/15/4/5 wt%).

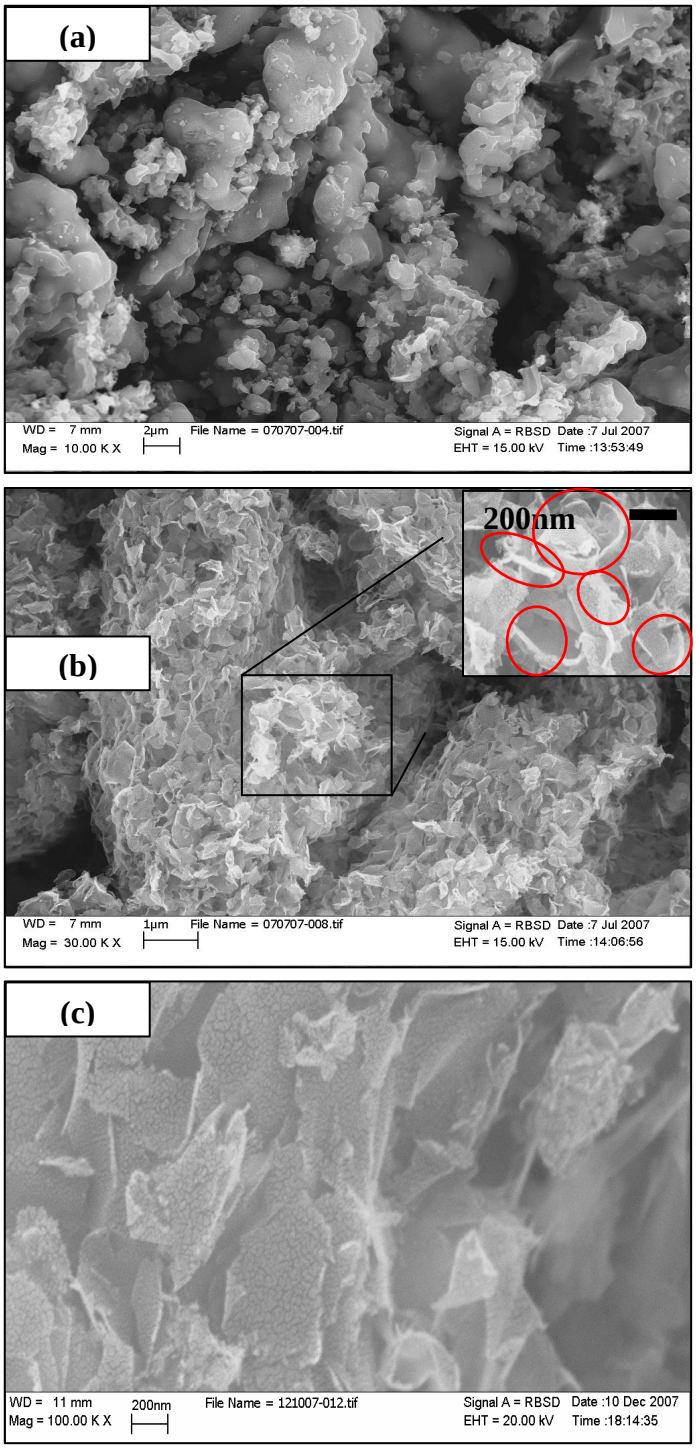

Figure 2.20. SEM images of residues from (a) PS/PMMA/DB/AO (70/30/15/4 wt%) and (b) PS/PMMA/DB/AO/C 20A (70/30/15/4/3 wt%), and a high magnification of PS/PMMA/DB/AO/C 20A (70/30/15/4/3 wt%)-the red circular lines indicate ribbon-like and tubular-like clay platelets, (c) PS/Cloisite 15A(90/10 wt%); flat-like clay platelets.

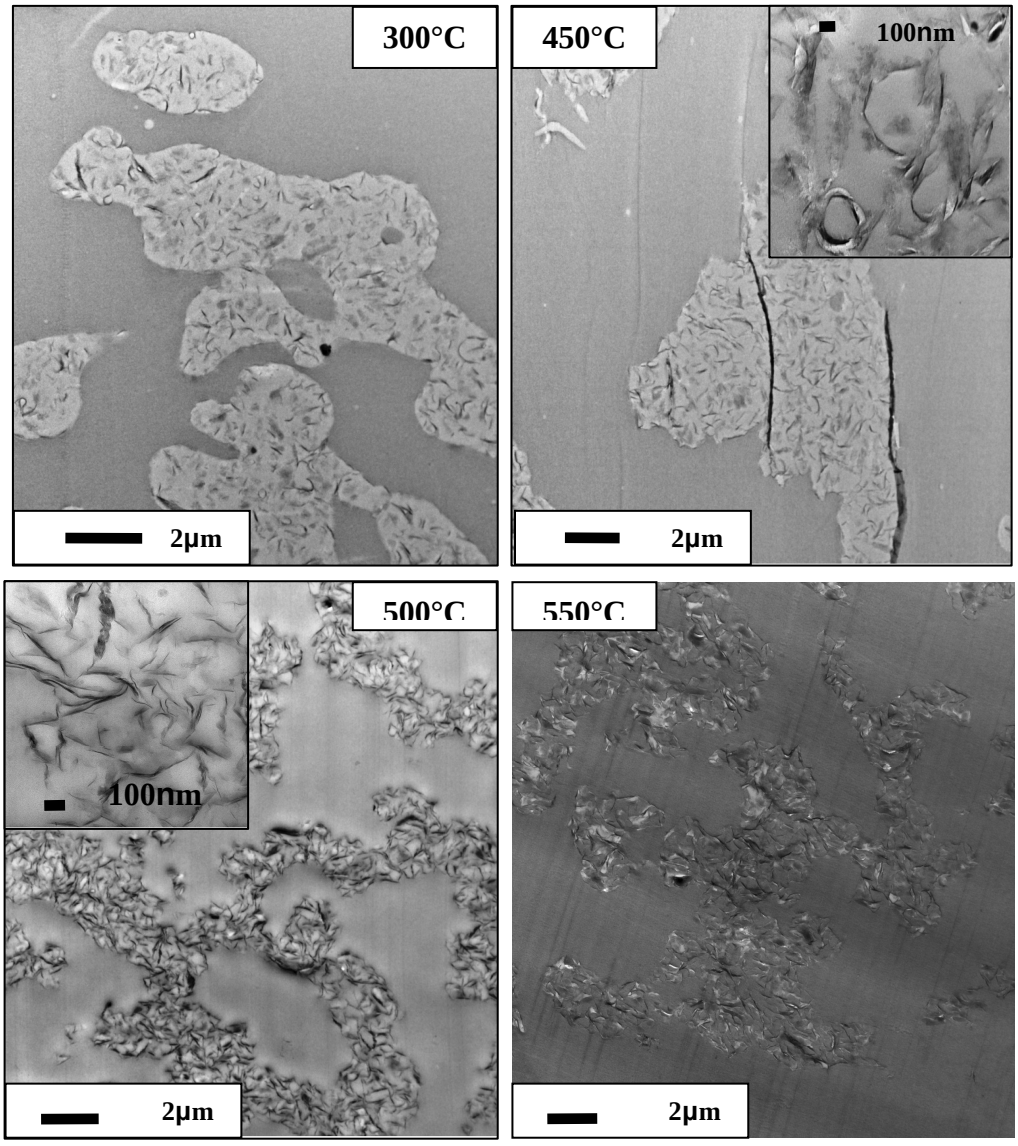

Figure 2.21. TEM images of PS/PMMA/Cloisite 20A (70/30/5 wt%) at different temperatures; (a) 300 °C, (b) 450 °C, (c) 500 °C, and 550 °C. Two high magnification images are inserted in 450 °C and 500 °C.

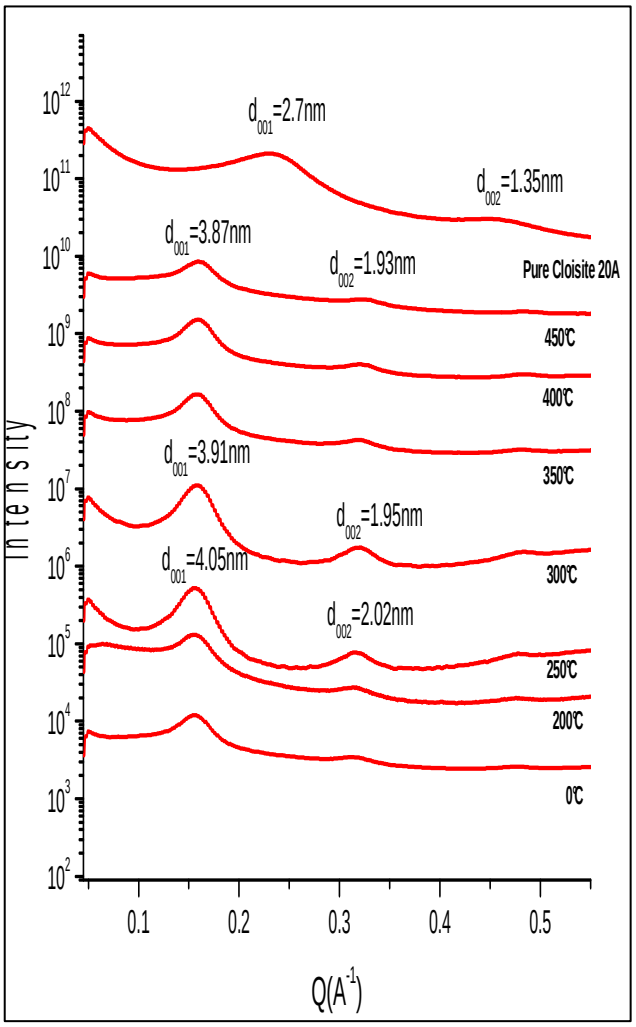

Figure 2. 22. SAXS data of PS/PMMA/Cloisite 20A (70/30/5 wt %) as a function of temperature

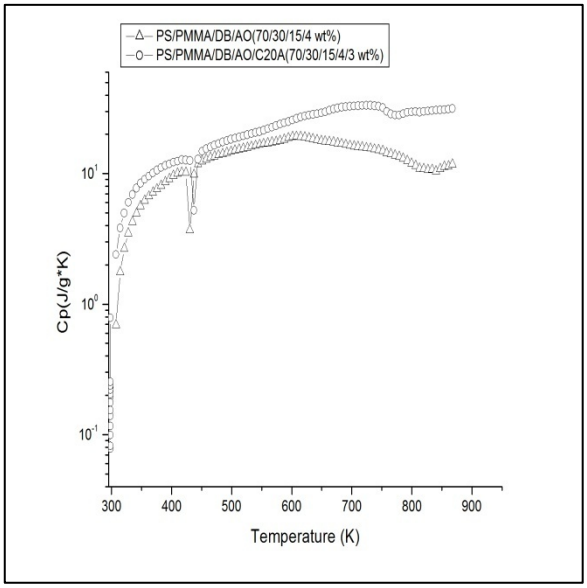

Figure 2. 23. Comparison of specific heat C with and without C20A in PS/PMMA/DB/AO polymer blend.

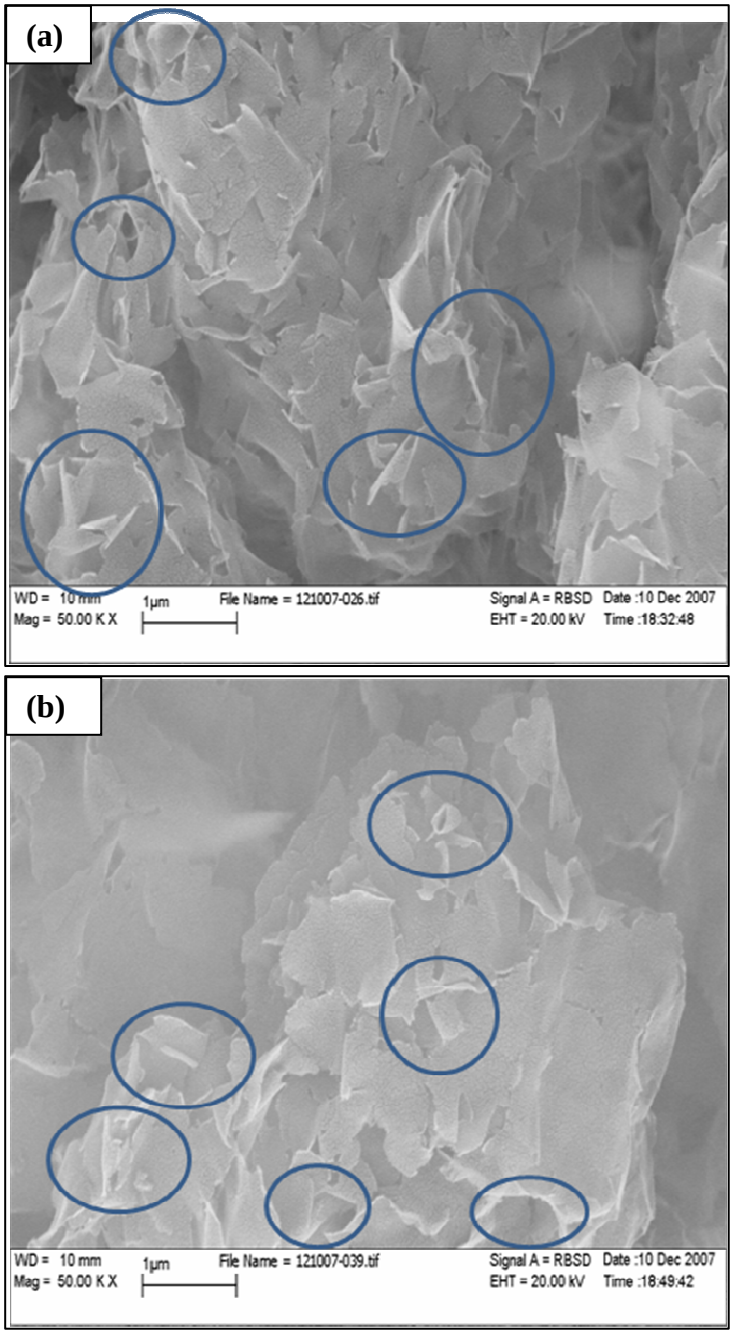

Figure 2.24. SEM images of residues from (a) PS/PMMA/C20A (70/30/5 wt%) (b) PS/PMMA/C20A (70/30/10 wt%) after N2 cone calorimetry; the red circular lines indicates nanotube-like clay plates.

Polymer	Mw or grade	Supplier
Polystyrene	280k	AMCO Plastic Materials Inc.
Poly(methyl methacrylate)	120k	AMCO Plastic Materials Inc
Polycarbonate	23k	Mitsubishi Engineering Plastic
Poly(styrene-co-acrylonitrile)	Luran 358N	BASF

Table 2.1. Polymers used in this study.

Sample	*Cloisite 20A*	*PMMA/DB /AO*	*PS/PMMA/DB /AO Cloisite 20A*	*PC/SAN24/D B/AO/Cloisit e 20A*
d_{001} Spacing (nm)	**2.70**	**4.10**	**4.05**	**3.57**
d_{002} Spacing (nm)	**1.35**	**-**	**2.03**	**1.79**

Table 2.2 d_{001} and d_{002} of Nanocomposites with FR and Cloisite 20A.

Time (Sec.)	*PSPMMA/DB/AO (70/30/15/4 wt%) Br w%*	*PS/PMMA/DB/AO Cloisite 20A(70/30/15/4/10 wt%) Br wt%*
0	**9.59**	**9.56**
3	**8.90**	**8.72**
9	**9.13**	**6.20**
12	**7.25**	**5.60**

Table 2.3. Quantitative determination of bromine (Br wt%) after different times by ion chromatography. (Formulations are based on per hundred resins.)

Sample (concentration wt%)	Peak HRR (KW/m2)	Average HRR(kW/m2)	Average MLR (g/s)	Ignition Time(sec)
PS/PMMA (70/30)	1507.8	792.9	0.123	25±1
PS/PMMA/Cloisite 20A(70/30/10)	563.2	288.6	0.050	21±2
PS/PMMA/DB/AO(70/30/10/3)	721.0	386.2	0.123	15±1
PS/PMMA/DB/AO/Cloisite20A (70/30/10/3/5)	320.2	228.7	0.072	18±2
PS/PMMA/DB/AO(70/30/15/4)	570.0	287.5	0.116	12±2
PS/PMMA/DB/AO/Cloisite20A (70/30/15/4/3)	375.0	211.5	0.111	15±2
PS/PMMA/DB/AO/Cloisite20A (70/30/15/4/10)	219.0	157.8	0.057	18±2

Table 2.4. Results of cone calorimeter of PS/PMMA or in PS/PMMA/DB/AO without the clay and with the clay nanocomposites. (Formulations are based on per hundred resins.)

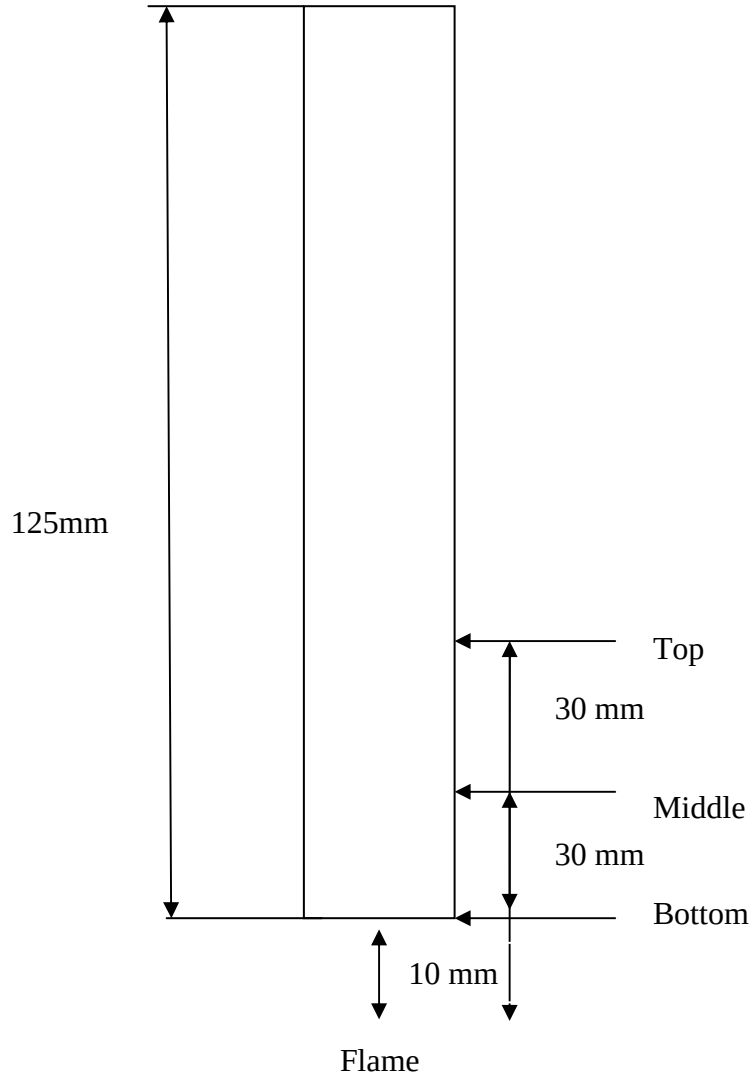

Illustration 2.1. Burning the bar and indexes of cutting for cross-sections.

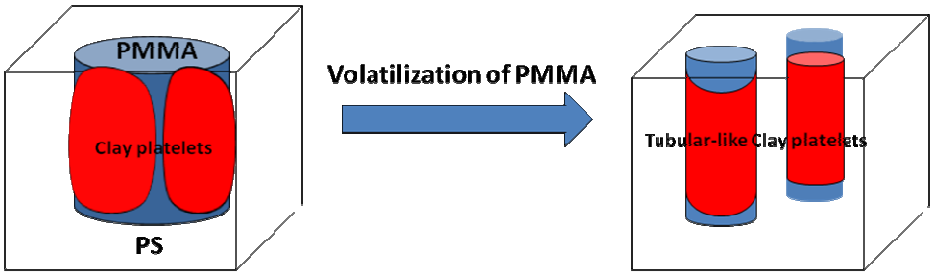

Illustration 2.2. The tubular-like clay platelets forming as PMMA volatilizes.

Chapter 3: Segregation of Carbon Nanotubes/Organoclays Render Polymer Blends Self-extinguishing.

3.1. Introduction

It has recently been demonstrated that the addition of as little as 0.5 wt % multi-walled (MWCNTs) or single-walled carbon nanotubes (SWCNTs) to a polymer matrix can affect the mass loss rate during decomposition, when the nanotubes are well dispersed within the matrix [7, 12, 34]. Recently, Kashiwagi *et al.*[12, 34] found that when either 1.0 wt % MWCNTs or 0.5 wt % SWCNTs was added to poly(methyl methacrylate) homopolymer, continuous network-like protective layers were formed. Hence they hypothesized that the network-like layers were to be the factor responsible for the reduction in the mass loss rate (MLR) between the filled and the unfilled homopolymers [7, 49]. In an earlier work, Si *et al.*[20] reported an increase in the flame retardant properties of PMMA when functionalized clays were added. This phenomenon was attributed to the long ribbon-like structures which formed spontaneously when the surfactants on the surfaces of the clays evaporated during heating. Later, they reported that when both the flame retardant (FR) additives and clay nanoparticles were added, a synergy was established where the heat release rate (HRR) and MLR were reduced by more than half as compared to the neat homopolymer [8].

Recently, Pack *et al.*[37] have shown that the synergy can be even greater when applied to polymer blends. In the case of polymer blends, the thermal properties can be very complicated because phase separation occurs continuously with different temperatures of thermal degradation. This thermal behavior is also difficult to predict since the distribution of the components in blends is continuously changing during

heating. Pack *et al.*[37] have argued that the inclusion of large aspect nanoparticles may be one solution to predict thermal responses in morphology of polymer blends since it was previously shown that they segregate to the interfacial regions, thereby stabilizing the blends against further thermal decomposition. Furthermore, since the FR particles adsorbed on the surfaces of the clay platelets, the high aspect ratio platelets also functioned as dispersants of the FR particles. The optimal clay loading to achieve these properties was approximately 10 % by weight, which is also sufficient to embrittle the polymer matrix and impact the ductility and fracture toughness. Since carbon nanotubes also have a high aspect ratio and an affinity for the flame retardant components, we therefore postulate that an additional synergy may exist when the two types of nanoparticles are combined. This would allow us to obtain superior flame retardant properties, but at a much lower particle loading and hopefully better mechanical properties. Since the aspect ratio of the MWCNTs is much larger than that of the clays, a much smaller loading can yield the mechanical properties which prevent dripping in the molten phase, without embrittlement in the solid phase.

Hence we decided to focus on PS and PMMA homopolymers and their blends, since they already were well characterized and the results could be directly compared to those already in the literature using Cloisite clays alone [49, 36-37, 50]. We then used a series of complementary techniques, in order to determine the relationship between the thermal properties, as measured by cone calorimeter, differential scanning calorimetry (DSC), and thermogravimetric analysis (TGA), with the blend and char microstructures as determined by transmission electron microscopy (TEM), energy dispersive x-ray spectroscopy (EDXS), scanning electron microscopy (SEM), and rheology, as determined by dynamic mechanical analysis (DMA).

3.2. Experimental Section

3.2.1. Materials and Nanocomposites Preparation:

The multi-wall carbon nanotubes (MWCNTs) were purchased from Helix Material Solutions, Inc. The lengths of the MWCNTs used in this study were 0.5~40µm purchased as a long carbon nanotube (*l*-MWCNT) and 1~2 µm as a short carbon nanotube (*s*-MWCNT) in the same diameter, 10~30nm. (The product IDs of the long and short MWCNTs were MWNT-12950030-00 and MWNT-129500-01, respectively. The batch numbers of both MWCNTs were BMCC05510017 and BMCC05510001.) Electron microscopy images of both types of MWCNTs were shown in figure 3.1. Polystyrene (PS) with an average molecular weight of 280K, and poly(methyl methacrylate) (PMMA) with an average molecular weight of 120K, were purchased from Sigma Aldrich. Cloisite 20A was provided by Southern Clay Products Inc. The flame retardant (FR) compound was decabromodiphenyl ether (DB), purchased from Sigma Aldrich and the synergist, antimony trioxide, Microfine® AO3, (AO) was purchased from Great Lakes Chemical Corporation. A C.W. Brabender, Type EPL-V501, with a direct current drive (type GP100) was used to blend the nanocomposites. The blender was equipped with two screw-type roller blades in a heating chamber. The polymer pellets were first added to the chamber at a rotation speed of 20 rpm and temperature of 170 °C. The FR agents were then inserted and mixed at the same rpm for 2 min. Either the MWCNTs or the Cloisite 20A clay was gradually added into the chamber, while blending. The entire mixture was blended at 100 rpm for 15 min. under nitrogen gas flow, which prevented degradation of the mixture from heat-induced oxidation. The mixture was allowed to cool at room temperature in the chamber, and then small pieces of the mixture were molded in a hot press into the different shapes required for the various mechanical tests and flame tests that were performed.

3.2.2. Flammability Measurements

The heat release rate (HRR) and mass loss rate (MLR) measurements of each sample were performed using cone calorimetry at the National Institute of Standards and

Technology (NIST). The samples were made by molding 24 ± 2g of the composite into a 75 mm x 75 mm x 5 mm square. The samples were then wrapped on three sides with thin aluminum foil, exposing one side in the direction of the thermal radiation. The samples were exposed, in ambient atmosphere, to an external radiant flux of 50 kW/m^2, normal to the sample surface and the HRR and MLR were measured as a function of exposure time. The residues in the thin aluminum foiled containers were collected and their morphology was characterized by scanning electron microscopy (SEM). The standard uncertainty of the measured heat release rate (HRR) was ± 10%. The cone calorimetry test was conducted by ASME/ISO 5660.

3.2.3. UL-94 V0 test

A vertical burning chamber purchased from Underwriters Laboratories Inc. was used to assess flammability. Samples of dimensions 125 mm x 13 mm x 1.5 mm were molded and tested using the protocol established by ASTM D3801/ISO 1210 UL 94 V0. The test to probe flame retardancy was conducted by first clamping the samples approximately 10mm from the top edge and suspending them, with the long axis pointing down, from a ring stand. A compressed methane gas burner with a gas flow rate of 105 mL/min was then placed 20 mm beneath the lower edge of the samples. A flame, 20 ± 2 mm, high was applied to the sample for 10 sec. and then t_1, the time that it took to extinguish the flame was measured. The flame was then reapplied and t_2, the time to extinguish the flame again was measured. If either t_1 or t_2 was less than 10 sec., then the sample was classified as V0 in the UL-94 test. Furthermore, it was also recorded whether the nancomposites dripped and /or ignited a wad of cotton placed under the holder. Table 3.1: results of UL-94V0 test from nanocomposites.

3.2.4. Morphology of Nanocomposites

In order to analyze the internal structures before and after exposure to the flame, transmission electron microscopy (TEM) and scanning electron microscopy (SEM), were used to characterize the morphology of samples. Transmission electron microscopy (TEM) was conducted with cross-sections of samples obtained fr**o**m before or after the vertical burning test. In particular, the vertically burned samples were cut into three parts.

The first piece was taken from the bottom of the sample, which was closest to the flame. The second one was chopped 30 mm away from the first cut in the sample. The last one was obtained 30 mm away from the second cut in the same sample. The cross sections were cut to a thickness of 70-80 nm using the Reichert-Jung Ultracut E ultramicrotome and then they were floated at the water surface on coated copper mesh grids. Morphology of the cross-sections was viewed from a FEI Tecnai12 BioTwinG^2 TEM at 80KV and digital images were acquired with an AMT XR-60 CCD digital camera system.

The elemental distribution of Br, or the flame retardant agent was imaged using an energy dispersive X-ray spectroscopy (EDXS) attachment on the SEM (LEO-1550) with a Schottky field-emission gun. The SEM/EDXS measurements were conducted on (5 mm x 5 mm x 2 mm) samples that were heated for different times in air at a temperature of 650 °C in a Lindberg SB Type 167 oven chamber. The SEM was also conducted with the residues after the cone calorimetry test in air. A few micrometers of gold were coated on the surface of the residues in order to make the specimens conduct.

3.2.5. Thermodynamic and Thermal Stability Measurements

Dynamic modulus of the samples was measured by a Mettler Toledo DMA/SDT 861e in the single cantilever mode. Elastic modulus and tan delta of samples, molded into bars of dimension 10 mm x 10 mm x 2 mm, were measured as a function of temperature, where the temperature was raised from room temperature to 180 °C at a rate of rate 2 °C /min from room temperature at a frequency of 1 Hz. A differential scanning calorimeter (DSC) was used to calculate the specific heat of chars. The DSC measured the heat flow of the char as a function of time and temperature. In order to correctly determine the specific heat, the mass of the samples is required and then input into the formula:[57]

$$Cp = \frac{\Delta \mathrm{H}}{\Delta \mathrm{T} \times \mathrm{M}} = \left(\frac{d\mathrm{H}}{dt}\right)\left(\frac{dt}{d\mathrm{T}}\right)\left(\frac{1}{\mathrm{M}}\right)$$

,where ΔH is the enthalpy change, ΔT is the temperature change, dH/dt is the heat flow difference between the blank and the sample, dt/dT is the reverse of the heating rate (20 °C /min) and M is the mass of the sample. Thermogravimetric analysis (TGA) was

performed using a Mettler-Toledo 2000 analyzer in order to determine the time/temperature sequence of mass loss in the decomposition. A small mass of a sample (10-15 mg) was measured and then inserted into an aluminum crucible. The crucible with the sample was put at the small dish in the furnace and then the temperature was increased from 30 °C to 800 °C at a rate of 10 °C/min. The TGA data was normalized in a percentage of mass loss and the first derivative of the spectrum was obtained in order to clearly indicate the transition points. Rheology measurements were carried out using a Bohlin Gemini HR Nano rheometer from Malverm instruments. A constant strain amplitude (0.5%) was applied for frequency sweep ($0.01 < \omega < 100$Hz) in oscillatory shear. All samples were run at 200 °C on a 20 mm under the flow of nitrogen to avoid degradation of the samples.

3.3. Results and Discussions

3.3.1. Morphology of Microstructures in Nanocomposites

3.3.1.1. Homopolymer Nanocomposites:

TEM cross-sections from the nanocomposites are shown in figure 3.2. From the figure we can see that both short and long MWCNTs are well dispersed in PMMA/DB/AO matrix by melt blending. The FR particles, which are electron dense and appear darker in color than the surrounding polymer matrix, are also seen to be much better dispersed when the MWCNTs are present. Analysis of the average FR particle size indicates that, in the absence of MWCNT's, large, micro-scale particles are present, with a mean size of 2 ± 0.5 µm. Addition of the MWCNTs is seen to dramatically decrease the size of the particles to 500-300 nm or 300-50 nm when *l*-MWCNTs or *s*-MWCNTs are added, respectively. In the inset we show higher magnification TEM images where we can see that the FR particles are preferentially attracted to the MWCNT surfaces, which increases their dispersion in the matrix. A similar result was also reported by Si *et al.* for the PMMA/DB/AO nanocomposites when Cloisite 20A were added [8].

In order to determine the effects of the dispersion on the mechanical properties of the polymer we also performed DMA and rheology tests. In figure 3.3a we show the tan delta plots of the nanocomposites, where we can see that the addition of either MWCNTs or FR particles increases Tg of the matrix from 125 °C to around 136 °C or 138 °C, respectively. However, the addition of both types of the MWCNTs together with the FR particles increases Tg of the matrix by 15 ^{o}C to 140 °C. This indicates that strong interactions exit between the matrix polymer chains and both the FR and the MWCNT particles. The slight additional increase in Tg when both particles are added can be explained by the additional surface area created for polymer adsorption sites when the diameter of the FR particles is decreased even further caused by the adsorption of FR particles onto the MWCNT surfaces. Hence, when PMMA is blended with other polymers, both the FR particles and MWCNTs will likely be segregated in the PMMA phase. Furthermore, the ability of the MWCNTs to better disperse the FR particles produces the synergy to which the enhanced mechanical properties shown in figure 3.3 can be attributed. In figure 3.3b we also plot the storage modulus of the nanocomposites

formed with *s*-MWCNTs or *l*-MWCNTs and PMMA/DB/ AO matrix, together with data for the unfilled PMMA matrix and the matrix with just the MWCNTs without the FR particles. From the figure we can see that the modulus of either the *l*-MWCNTs or *s*-MWCNTs filled nanocomposite samples are reduced about 20 % as compared to the modulus of pure

PMMA sample for T < 90 °C. Above that temperature the modulus of both the MWCNTs increase, which would predict the enhancement of impact toughness when the carbon nanotubes are added. The addition of FR particles (25 % by weight) increases the magnitude of the modulus by 35 % relative to that of pure PMMA. This may lead to an increase of brittleness and would reduce the impact toughness. However, the addition of both types of particles; FRs (25 wt %) and MWCNTs (0.5 wt %) increases the modulus by 70 % relative to that of pure PMMA for T < 90 °C. This increase of the modulus may produce overall a tougher material [58]. In figure 3.4 we show the elastic modulus versus frequency plots for the PMMA nancomposites. From the figure we see that the addition of 0.5 wt % MWCNTs produces only a slight enhancement of the storage modulus, in agreement with the previous results of Kashiwagi [12] with only a negligible difference between the long and short nanotubes. The addition of FR particles to PMMA increases the modulus by a factor of less than half. On the other hand, the addition of both FR and MWCNTs particles produces a dramatic increase by nearly one and half orders of magnitude at frequencies below 1 Hz. This indicates that by themselves, neither low concentrations of MWCNTs or FR particles produce a network structure. On the other hand, together, they also establish a synergy in the dynamical properties corresponding to the formation of internal networks. The percolation of the networks at smaller MWCNTs concentrations may also be due to the strong interactions with the matrix by the DB/AO particles and the increased surface area available for the adsorption of polymer chains, which is a result of the improved dispersion. Network formations were previously reported to correlate with improved flame retardant properties, due to the improved structure of the char layer. In the previous case, the improvements were observed only after the addition of at least 2 % MWCNTs. This was the minimum concentration of MWCNTs which formed a dense network, smooth char layers, and the reduced MLR. In our case, the combination of particles produces an even larger decrease in the HRR,

which is not surprising given the UL-94 V0 response to heating in an open flame. Hence the superior flame retardant properties can be also being directly attributed to the synergy with the MWCNT that produces the enhanced dispersion of the FR particles. In figure 3.5 we show a series of TEM images taken from segments obtained at different distances from a flame. From the figure we can see that the dispersion of both MWCNTs and FR particles is similar in all frames, indicating that it is not affected by the flame, which was applied during the UL-94V0 testing time of 20 seconds. The network formed by the MWCNT prevented the polymer/DB/AO melt from dripping, while the FR particles remained uniformly distributed, since it was adsorbed to the nanotubes, and did not flow with the polymer.

3.3.1.2. Polymer Blends Nanocomposites

Improving the flame retardant properties in immiscible polymer blends is considerably more complex than in homopolymers. In this case, the polymer/ FR composites form a complicated three phase system with unpredictable behaviors when heat is applied. We have previously shown that the addition of 5 % Cloisite 20A to PS/PMMA/DB/AO system can stabilize the system against further phase segregation and disperse the FR particles inside the PMMA phase, which resulted in improved flame retardant properties such as the reduced MLR and HRR, (and passing the UL-94 V0 test). Si *et al* [31] had also shown previously that clays added to immiscible polymer blends can form *in situ* grafts which segregate to the polymer interfaces and promote compatibilization. When the FR formulation was added though, the FR also segregated to the clay surfaces, displacing the polymer and interfering with the ability of the clays to act as interfacial tension reduction agents [37]. We have also shown previously that other large aspect ratio particles can also compatibilize polymer blends [52]. Hence we postulated that the addition of MWCNTs may enhance the compatibilization of the blend and thereby improve its thermal and rheolocical properties, while decreasing the total concentration of particle additives. We therefore reduced the amount of Cloisite 20A clay from 10 % to 3 % and added 2 % MWCNTs. TEM cross-sections of the nanocomposites blended with *l*-MWCNT and *s*-MWCNT are shown in figure 3.6, which is included with the image of cross-section obtained from the polymer blend without the nanoparticles

additives. From the figure we can see that the FR particles segregate in the PMMA phase, while the clays, which also segregate in the PMMA phase, are present at the interfaces. Comparing the images of the *s*-MWCNTs with those from the *l*-MWCNTs, we find that the FR particle size is significantly smaller in the blend with the *s*-MWCNTs, which is shown in figure 3.6b. Furthermore, we find that in the case of the *s*-MWCNTs, all tubes are present both in PMMA and PS phases, while in the case of *l*-MWCNTs most of the tubes are in PS phase. In the inset we show a higher magnification images where we can more clearly resolve the MWCNTs. From the images we can see that the FR particles are preferentially segregated on the *s*-MWCNT rather than the clay surfaces. The presence of some of the *s*-MWCNTs in the PMMA phase then assists in the dispersion of the particles.

Furthermore, as can be seen in the figure, the clay platelets are again localized at the polymer interfaces, as previously shown by Si *et al* [31], since no FR particles are present to screen the surface interactions. The surface interactions also impact the rheological properties of the blend. In figure 3.7 we show the DMA data obtained for the polymer blends with FR particles, Cloisite 20A, and both types of MWCNTs. The moduli at T = 50 °C and the values of T_g obtained from the Tan delta measurements are tabulated in table 3.2. From the table we can see that the addition of FR particles to the blend lowers the modulus by nearly 26 percent. In the case of the homopolymer FR particles increased the T_g of the compound indicating that they interacted favorably with the matrix, and the increased interfacial adhesion with the inorganic particles enhanced the mechanical strength of the micro-composite. In the case of immiscible polymers, the unfavorable interactions between the two components decrease the interfacial penetration between domains which reduces the mechanical integrity of the blend [52]. The FR segregates exclusively into the PMMA domains and hence do not reinforce the blend. In fact an increased T_g is likely to be accompanied by a decreased diffusion coefficient and as has been previously observed for carbon nanoparticles in a PB blend, decreases the interfacial width between domains [52]. This phenomenon would be consistent with the further decrease in modulus resulting from addition of the FR particles. Addition of the Cloisite clays somewhat restores the modulus of unfilled blend since, as was previously shown, the clay platelets are positioned at the blend interfaces, reducing the interfacial

tension. But, as was shown in ref.[37] when FR particles are present they compete with the polymer chains for the clay surfaces, thereby reducing the efficiency of the clay to form grafts and reduce the interfacial tension.

A significant improvement is observed when the MWCNTs are added, with the short MWCNTs being even more effective than the long MWCNTs. Examination of figures 3.2 and 3.6 provides a possible explanation for the observed synergy. As we discussed for the case of the homopolymer, the FR particles prefer the carbon nanotube surfaces to those of the clays. Hence even in the blend, the carbon nanotubes are decorated with the FR particles within the PMMA phase domains. As a result, the clay platelets can now form in situ grafts thereby reducing the interfacial tension, improving the adhesion between the components, and increasing the modulus, as was shown by Si et al for the blend without the FR particles [31]. As a result of the increased interfacial area, the mean size of the FR particles is slightly smaller and the dispersion is improved in case of the addition of short MWCNTs, which is confirmed by the figure 3.5b. Hence the major difference between the two types of MWCNTs appears to be in the dynamical response of the matrix to the addition of the tubes. This can further be probed with greater accuracy by comparing the frequency responses of the moduli of the two different types of samples.

3.3.2. Rheological measurements

The frequency dependence of storage modulus also provides a sense of internal dynamics of a polymer blend. In figure 3.8 we plot G' vs ω for the different nanocomposites, and compare them to the unfilled polymer blend. From the figure we can see that the overall frequencies the pure polymer blend follows the classical scaling behavior for a ($G' \sim \omega^2$) viscous liquid, as expected at T = 200 °C. The temperature is sufficiently high that no plateau is observed even at 100Hz, indicating that 1/frequency is still long enough that the polymer chains are rearranged in their configuration. When the FR particles is added we find that G' still obeys the liquid like relationship at low frequencies, but the absolute value is nearly an order of magnitude higher, which is consistent with an increase in "rigidity" due to an increase in T_g caused by the attractive interactions between PMMA phase and the FR particles. The addition of Cloisite 20A

with the FR particles does not affect the rheological responses significantly; hence no change has occurred in the polymer dynamics. Even though the Cloisite 20A has previously been shown to decrease the diffusion coefficient of PMMA and hence increase the viscosity [23], in this case, the clay platelets are covered with the FR particles and hence do not interact effectively with the polymer chains, confirming the observations of Pack *et al*.[37] A significant change occurs with the addition of MWCNTs. At low frequencies the response with both types of nanotubes is identical. A small flat region is observed initially indicating the formation of a weak network of entanglements. At approximately 1Hz the response of the samples with the two types of MWCNT begins to diverge. G′ for the *s*-MWCNTs continues to increase till about 10 Hz, when a sharp decrease is observed. In the case of the *l*-MWCNT a plateau occurs at 1 HZ, indicating the formation of an entangled network. The plateau extends till 10 Hz when a sharp decline is observed. The sharp decrease in both cases is indicative of a breakdown in the melt at these higher frequencies which occurs only upon introduction of the nanotubes.

3.3.3. Thermal Properties

In order to examine the evolution of the microstructures after flame testing, samples (125 mm × 13 mm × 1.5 mm) of PS/PMMA/DB/AO/Cloisite 20A with the *l*-MWCNTs or the *s*-MWCNTs were exposed to a flame as shown in figure 3.9 for a total time of 20 sec. (following the UL-94 V0 test protocol). Each sample of the bar was then divided into two sections. The middle section was 20 mm away from the flame, and the top was another 30 mm away, (or 50 mm) away from the center of the flame as shown in figure 3.9 (top). The lowest segment that was in the flame contained mostly char and is not shown. TEM images of the cross-sections obtained from the *l*-MWCNTs and the *s*-MWCNTs nanocomposites are shown in figure 3.9a-b and 3.9c-d, respectively. The major difference between the two types of samples is in the distribution of MWCNTs. In the case of the *l*-MWCNTs, a large fraction of the tubes can be seen in PS phase, and this fraction is nearly the same between the top and bottom portions of the sample. In the case of the sample containing *s*-MWCNT, a few nanotubes are seen in the PS phase in the top image, but all the nanotubes are now in PMMA phase in the middle image.

In figure 3.9b-1 and 3.9d-1 we show magnified sections of a PMMA segment in each of the images. Here we can see that in the case of the *l*-MWCNT sample, the FR particles are clustered around clay platelets in the PMMA phase. A few nanotubes can be seen at the PS/PMMA interfacial region, but most tubes remain in the PS phase. In the case of the s-MWCNTs, many the nanotubes can be seen segregated in the PMMA phase, including a large fraction of nanotubes that are at the PS/PMMA interfaces. As shown previously, the FR particles appear adsorbed to the carbon nanotube surfaces, even in the middle segment. In figure 3.9e we also plot the mean FR particle sizes obtained from both types of samples, and compare the sizes in the top and middle segments.

From figure 3.9 we can see that the clays in both types of samples have begun to form the characteristic ribbon like structures that were previously reported to form when the samples were heated to the decomposition temperature (T > 250 °C) of the di-tallow surfactants on the Cloisite 20A clays. In the top part of the samples, the average FR particle size however did not change significantly from the value found in the unheated samples (fig. 3.5), indicating that the ambient temperatures in this region were below 350 °C, the decomposition temperature of “decabrom”. In both cases we can see that the average particle diameter decreases significantly in the mid-portion of the samples. The rate of decrease however seems to be significantly larger in the *s*-MWCNTs sample, which is consistent with the smaller initial particle size, where the rate of decrease is a function of both temperature and particle diameter.

3.3.4. Energy dispersion analysis X-ray (EDAX)

In order to confirm this observation the two types of samples were also imaged using SEM with energy dispersion analysis X-ray (EDAX) mapping which provides elemental specificity for higher Z elements. *l*-MWCNT and *s*-MWCNT samples were heated to 600 °C in air for different times and cross-sectioned. The SEM scans of both samples are shown in figure 3.10. From the figure the bright regions correspond to the FR particles which have higher Z than the matrix and scatter more electrons. The yellow images were obtained by setting a window on the Br l-edge peak obtained from the EDAX spectra of the samples and scanning. Since the x-rays come from a broad internal region, the intrinsic spatial resolution of EDAX is approximately one micron. Hence, to

obtain enough intensity, the scale bar in these images is 10 microns, and the bright regions correspond to entire PMMA *domains* where the FR particles are segregated. From the figure we can see that in the case of the *l*-MWCNTs, the FR domains, are initially bright after heating for 5 seconds, somewhat less bright after 15 seconds and disappear 20 seconds after heating. Hence, the Br is no longer visible after 20 seconds. In contrast, for the case of the *s*-MWCNT, the bright domains disappear faster, or after 15 seconds of heating, hence the smaller particles are more easily converted to the vapor phase. The more efficient vaporization of Br particles improves the ability of the formulation to act as a flame retardant and react in a vapor phase with the gaseous degradation products of polymers that are emitted sooner than those of the inorganic components.

3.3.5. Thermogravimetric Analysis (TGA)

In order to investigate the effects of the nanotubes on the thermal stability of the melt we also performed TGA measurements on the nanocomposites. The results for the homopolymer are shown in figure 3.11. In contrast to the results reported in Pack et al, where clay was seen to increase the thermal stability, the addition of MWCNT in PMMA/DB/AO blend appears to be no change in the trace of the blend, which indicates that the addition of MWCNTs mainly act as a physical barrier in the molten polymer matrix. This is also consistent with the results that there was no dripping in the UL94 V0 flame test. Another interesting fact is to note that the decomposition temperatures of both formulations are symmetrically located around the decomposition temperature T = 350 °C of DB. Furthermore, we can also see that both formulations have only one decomposition temperature, as opposed to the two step process observed with the PMMA polymer. Hence the precise order to the decomposition is not as important as the proximity to the decomposition temperature of the DB in facilitating the gas phase reaction which stabilizes the polymer matrix from decomposition, and quenches a flame.

The effect is even more dramatic in the case of the blend. Here we find that the addition of PS moves the degradation temperature of the blend to T = 375 °C, which is significantly higher than that of the DB. Furthermore, as reported in the previous paper, there is still the separated decomposition of component at around 500 °C. The addition of

both types of nanotubes reduces the decomposition temperature of the blend, to T = 350 °C which is in the "operating" range of the ability of the DB vapors to react with the polymer blend and quench the flame. Hence the addition of MWCNTs renders the blend flame-resistant and self-extinguishing under the UL-94 condition, whereas simply the addition of clays does not.

3.3.6. Cone Calorimetry

Flammability measurements were performed in the cone calorimeter, where the heat release rate (HRR) and the mass loss rate (MLR) represent that the heat is measured by measuring oxygen concentration in the exit gases, and that the mass is lost as a function of combustion times. The results form analysis of the data from the cone calorimetry experiments are tabulated in Table 3.3 and Table 3.4.

PMMA homopolymers: From figure 3.12 we can see that the peak HRR is 1440 kW/m^2 for the homopolymer. When FR particles are added, the peak is reduced to a steady plateau at about 490 kW/m^2. Similarly, in the absence of FR, a peak observed in the MLR which corresponds to the peak in the HRR. When the FR is added the MLR also becomes nearly constant in time. This large reduction of the PHRR by the addition of FR is not surprising and results primarily in chemical reactions as the FR particles go into the gas phase [14]. When only (0.5 wt%) of the *l*-MWCNTs are added in the PMMA/DB/AO nanocomposite, the flame retardant properties are not improved. In fact we can see that the time to ignition is decreased from 18 to around 10 seconds. Increasing the fractions of *l*-MSCNT to 1.5% does not alter the ignition time, and only slightly alters the MLR and HRR.

Kashiwagi *et al.* reported similar results for the PP/MWCNT systems where they also observed a sharp decrease in the ignition time with only 0.5 % MWCNT. When the MWCNT concentration was increased to 2 % or higher, the time of ignition changed as well, and became more similar to the value of the unfilled PP. Rheological measurements performed on PMMA melts indicated that 2 % was the percolation threshold for the formation of an entangled network of MWCNTs where physical contacts of the tubes was obtained [34]. We therefore postulate that these contacts are also effective at improving the thermal conductivity of the melts. The thermal conductivity of MWCNTs is 750

W/mK, which is much higher than that of clays or polymer, which are respectively, 1.1 W/mK and 0.5 W/mK [54-56]. Hence when the concentration of MWCNTs is low, the tubes are surrounded only by the polymer matrix, which forms an insulating layer. As the thermal front advances, the tubes heat up faster than the surrounding polymer, igniting the matrix at earlier times. However, when the tubes are percolated, then they can also rapidly dissipate the heat throughout the sample, thereby potentially increasing the time to ignition.

PS/PMMA Polymer Blends: In figure 3.13 we show the cone calorimetry data for PS/PMMA blends. From the figure we can see that in contrast to the PMMA melts, the addition of FR agents does not significantly improve the flame retardant properties. The FR agents decrease the peak HRR, but do not make a steady plateau at HRR. The addition of the FR increases the MLR and moves the peak to earlier times. The addition of only 3 % Cloisite 20A produces the largest decrease in HRR and MLR. But as, previously reported, the blend is not self-extinguishing, according to the UL-94 V0 criteria. The addition of 2 % MWCNTs and 3 % Cloisite clays does produce the blend which passed the UL-94 V0, but as can be seen from figure 3.13, the thermal properties of two types of MWCNTs are different. The short nanotubes appear to be the most effective at reducing the MLR and HRR, while the long MWCNTs produce results which are worse than those of the clays alone.

In figure 3.14 we show the times to ignition, where we find that the clays decreases the time of ignition, but both types of MWCNTs decrease it even more. Increasing the MWCNTs concentration even to 6 % fails to further increase the ignition time. This is in sharp contrast to the PMMA melts, where 6 % is far above the percolation concentration in a homopolymer-MWCNT matrix. From figure 3.6 we found that both clays and MWCNTs were segregated preferentially in the PMMA phase. Hence we postulate that in this case the clays may be interfering with the contacts between the tubes achieved at a percolation. Hence the effective percolation may be occurring at even higher concentrations.

3.3.7. Analysis of Char:

Neither PS nor PMMA form char when burned. A formation of rigid chars when functionalized clays are added to either the homopolymer or the blend may be one of the most important factors explaining in the large reduction of HRR and MLR. The formation of chars sets up a thermal barrier which dissipates heat from the burning gases and the external heat flux. We have previously shown that when the surfactants on the clays disintegrate, the clays form the long ribbon-like structures and in the case of the blends, even tube-like structures, which enhanced the thermal dissipation through contacts between the clay surfaces. The higher thermal conductivity of MWCNTs can, in principal, also improve the thermal properties of chars, if good physical contacts are achieved between the tubes.

In figure 3.15 we plot the specific heat, Cp is inversely proportional to thermal diffusivity, of the chars as a function of temperature. From the figure we can see that the Cp of the blend with long nanotubes is even higher than that of the blend without the MWCNTs. Furthermore, the Cp remains fairly constant with temperature. On the other hand, the Cp of the blend containing the short nanotubes, is initially the same as that of the blend with just the clays, but as temperature increases above 600 K, the Cp is sharply reduced. Comparing this data to the one in figure 3.13 we find that the addition of *l*-MWCNTs also increases the MLR and HRR over the values of the samples containing just the clays, while the addition of *s*-MWCNT reduces these quantities. We can then propose the following model to explain the enhanced flame retardant properties achieved only with the addition of the short nanotubes.

In figure 3.16 we show SEM images of the three types of chars. From the figure we can see that the char with *l*-MWCNTs contains many clay platelets entangled among the MWCNTs. The clay platelets interfere with the ability of the MWCNTs to form good thermal contacts with each other which are required to dissipate the heat by conduction. Furthermore, we can see that both types of MWCNTs interfere with the production of the clay ribbons or tubes reported previously.[37] Hence the improvement in the HRR and MLR obtained by adding the clays is reduced when the *l*-MWCNT are added. As, we discussed previously, the long MWCNTs are entangled and remain fairly stationary

within the polymer blend, while the *s*-MWCNTs are mobile and can segregate into different areas in the molten polymer blends. Examination of the char containing the *s*-MWCNT in figure 3.16c shows that most of the nanotubes are now segregated from the clays and into separate clusters where they can improve the physical contacts with each other and conduct heat more efficiently. The model is confirmed from measurement of the Cp of the chars in figure 3.15 where we find that the value for the one with s-MWCNTs is the lowest.

In summary, good heat dissipation is crucial in improving the flame retardant properties of materials. The low thermal conductivity of MWCNTs in a polymer matrix can be of advantage when good thermal contacts between the tubes are possible. At early stages, when the polymer matrix is present, the *l*-MWCNTs provide a better thermal pathway, which helps in raising the ignition time by conductively dissipating heat, while at longer times, the ability of the *s*-MWCNT to segregate allows more thermally conducting chars to form, thereby reducing the HRR and MLR. Hence a combination of the two types of MWCNTs would probably provide the best thermal properties.

3.4. Conclusion

We have shown that the addition of certain nanoparticles mixtures can enhance flame retardancy to a greater degree than the addition of either of the particles alone. The effect is particularly efficient in polymer blends, where more variables need be considered in the flame behavior. We studied PS/PMMA blends and the respective homopolymers. In this paper we focused on the combination of MWCNTs with clays. We found that the FR particles segregate to the MWCNTs preferentially, thereby allowing the clays to segregate to the blend interfaces. In this manner the clays are more efficient at stabilizing the blend against phase segregation during burning, while at the same time dispersing the FR particles uniformly. An important consideration in flame retardancy is the time to ignition as well as the HRR and MLR. Addition of either clays or MWCNTs can drastically lower the time to ignition, even though they have been shown to improve the HRR and MLR once ignition has started. The high thermal conductivity and low specific heat of the nanoparticles allows them to heat up faster than the surrounding polymer and reach the ignition temperature of the matrix sooner than the unfilled compound. If the nanoparticles form a percolating structure, such as that formed by the l-MWCNTs, which can entangle with each other, the heat is conducted away towards the sample surfaces, explaining the observation that with increasing concentration of the MWCNTs, the time to ignition increases (figure 3.12 and ref.[34]) In the case of the blend, the situation is more complex.

Here we also added clays to stabilize the compound against phase separation. The clays were interspersed between MWCNTs, preventing good contact, and as a result, no improvement in ignition time was observed even for concentrations as high as 6 %, where percolation was shown to occur in homopolymers.[34] Even though the HRR and the MLR of the compounds containing l-MWCNTs and clays, were lower than those of the unfilled compound, they were higher than those of the compound containing only clays. The addition of short MWCNTs, on the other hand, did not affect the time to ignition but significantly reduced the HRR and the MLR. Prior to ignition, the s-

MWCNTs were also separated by the clays, and had poor conduction properties, but as the polymer was heated, the s-MWCNTs became mobile and we observed that they segregated together both in the char and in the compound. This resulted in a percolated phase which was able to reduce the specific heat at high temperatures. From these findings we conclude the flame retardant properties of nanocomposites depend on the organization, as well as the chemical nature of nanoparticles. In this manner combinations of nanoparticles can achieve a synergy which minimizes the total amount of fillers, and preserves the mechanical properties of polymer blends.

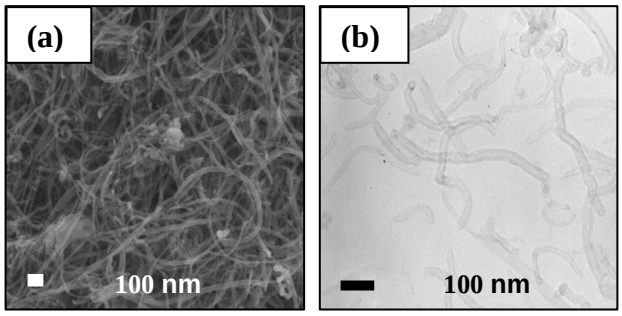

Figure 3. 1. (a) SEM image of *l*-MWCNTs (b) TEM image of *s*-MWCNTs.

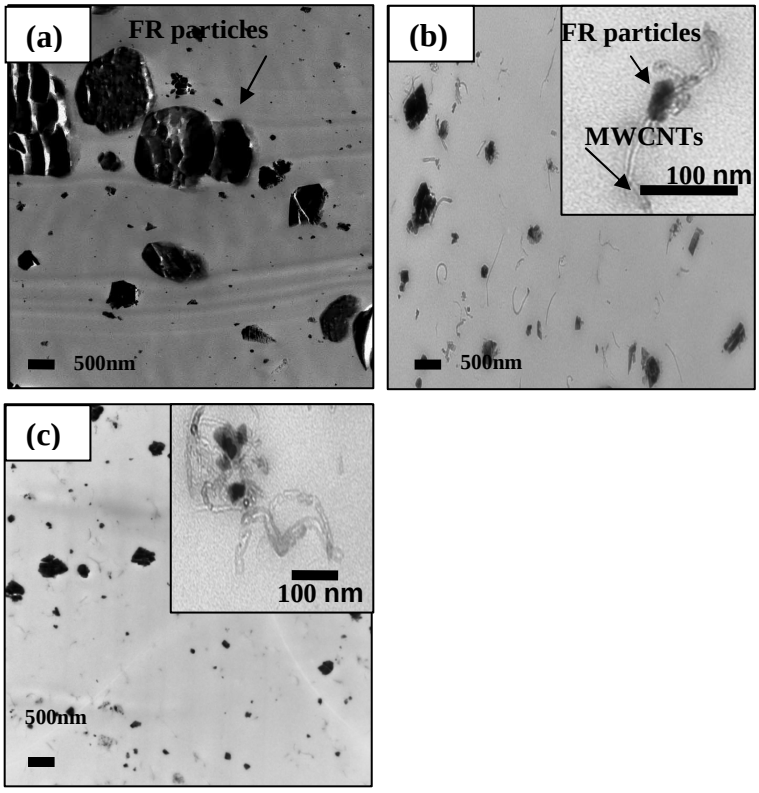

Figure 3. 2. TEM images: (a) PMMA/DB/AO(75/20/5 wt%), (b)PMMA/DB/AO/*l*-MWCNT(75/20/5/0.5 wt%), and (c) PMMA/DB/AO/*s*- MWCNT(75/20/5/0.5 wt%)

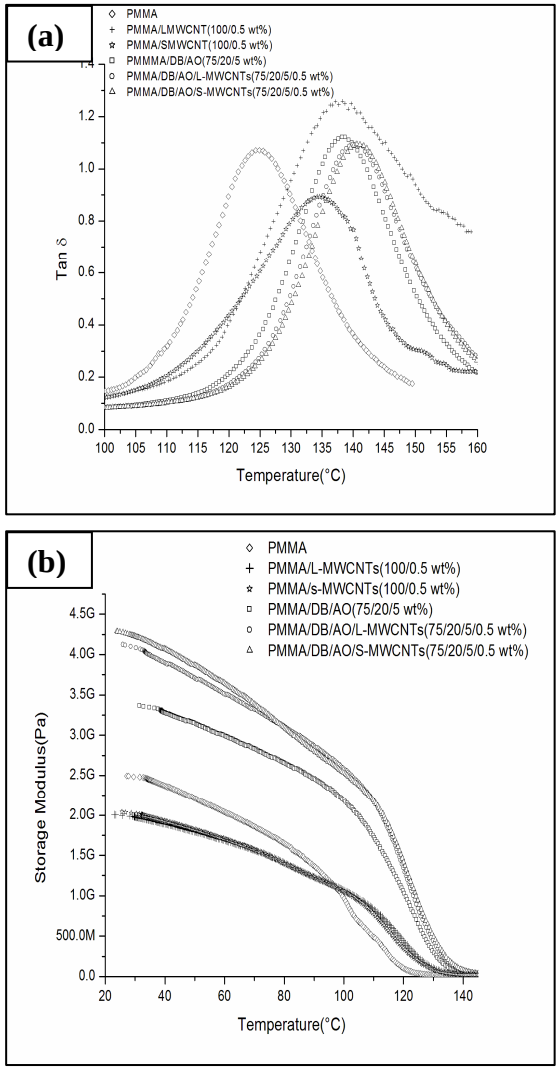

Figure 3. 3. Storage modulus and Tan δ vs Temperature curves: PMMA-unfilled diamond. PMMA/*l*-MWCNT(100/0.5wt%)-unfilled cross, PMMA/*s*-MWCNT(100/0.5wt%)-unfilled star, PMMA/DB/AO(75/20/5 wt%)-unfilled square, PMMA/DB/AO/l-MWCNT(75/20/5/0.5wt%)-unfilled circle, and PMMA/DB/AO/*s*-MWCNT(75/20/5/0.5wt%)-unfilled triangle.

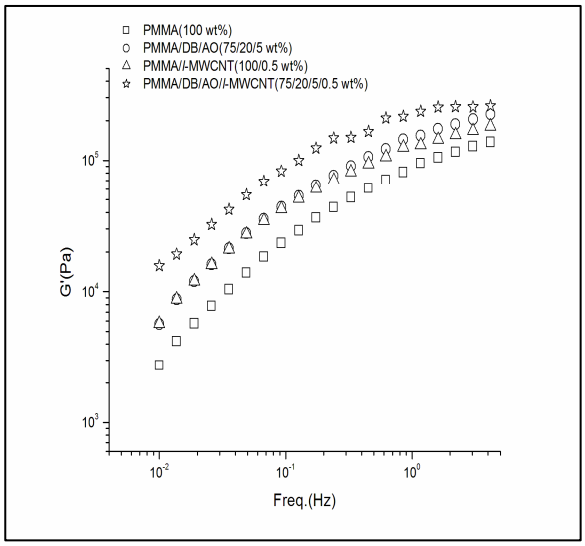

Figure 3. 4. G′ vs Frequency Curves: PMMA- unfilled square. PMMA/DB/AO(75/20/5 wt%)- unfilled circle, PMMA/*l*-MWCNT(100/0.5 wt%)- unfilled triangle, and PMMA/DB/AO/*l*-MWCNT(75/20/5/0.5wt%)- unfilled star.

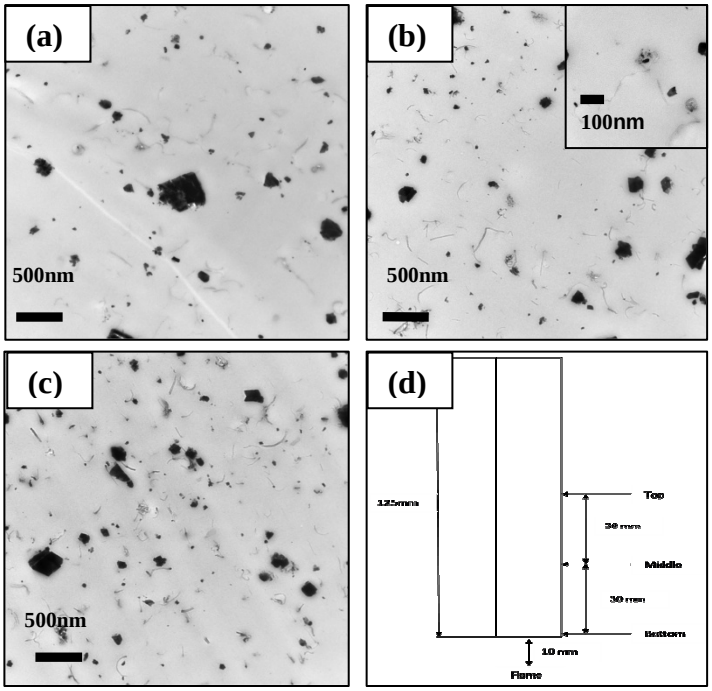

Figure 3. 5. TEM images obtained from a nanocomposite bar that was heated in a flame for the UL-94-V0 test : (a)-Top, (b)-Middle, (c)-Bottom of PMMA/DB/AO/*l*-MWCNT(70/25/5/0.5 wt%), and (d) Scheme of UL-94 V0 set.

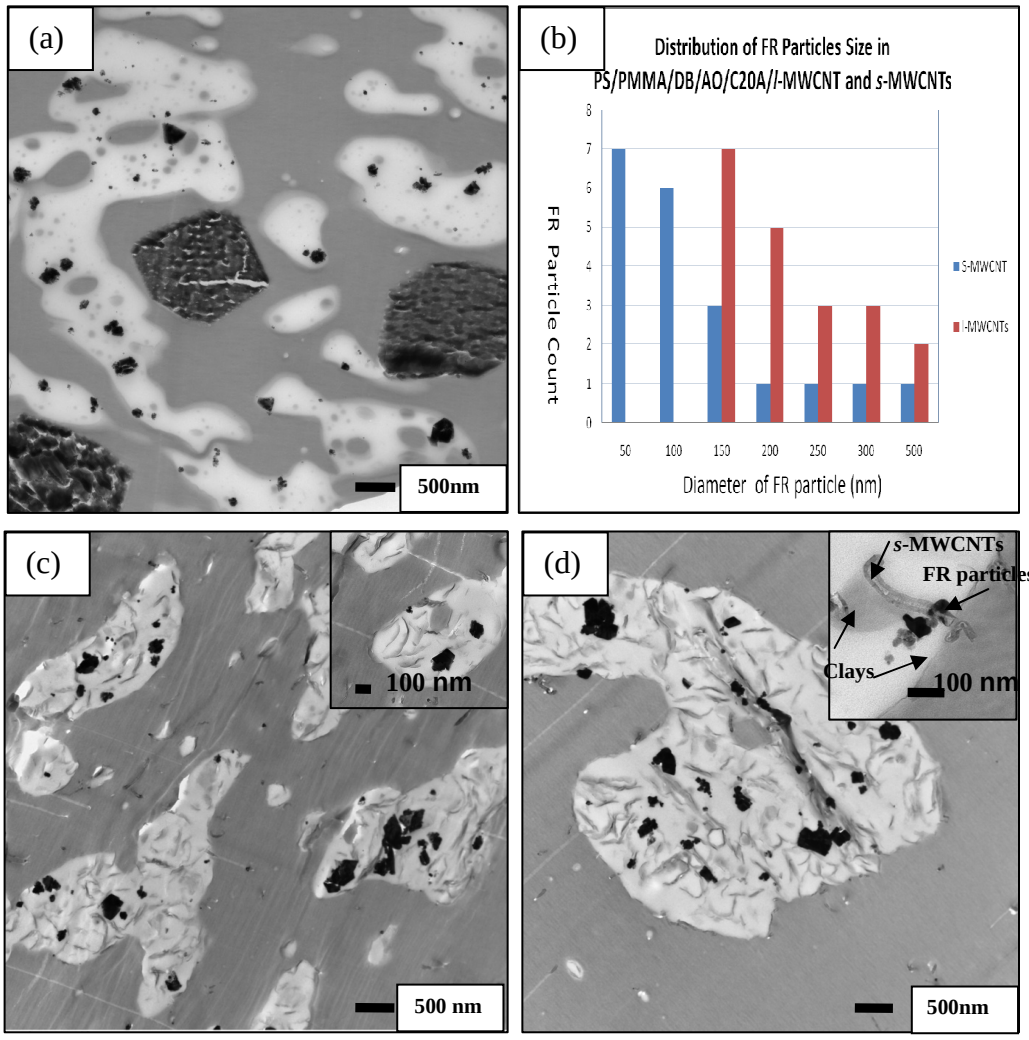

Figure 3. 6. TEM images: (a) PS/PMMA/DB/AO (70/30/15/4 wt%), (b) Distribution of FR particles Size in PS/PMMA/DB/AO/Cloisite 20A/l-MWCNT and s-MWCNT (c) PS/PMMA/DB/AO/Cloisite 20A/*l*-MWCNT (70/30/15/4/3/2 wt%), (d) PS/PMMA/DB/AO/Cloisite 20A/*s*-MWCNT (70/30/15/4/3/2 wt%).

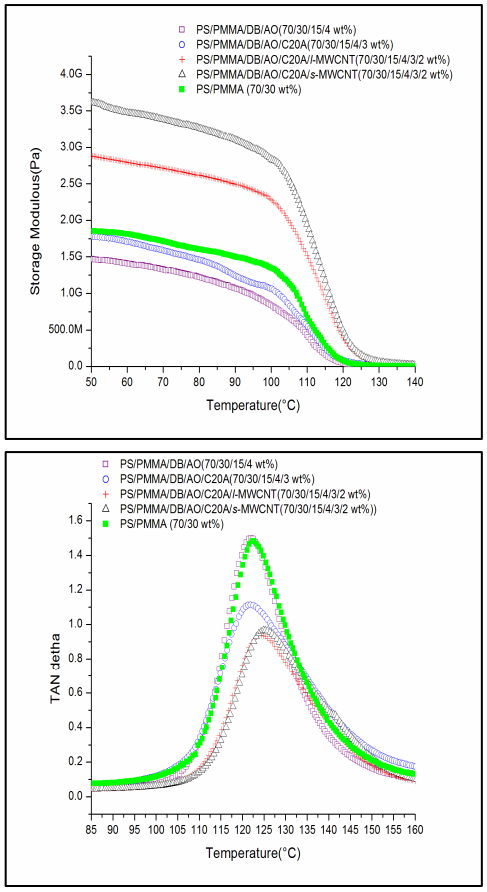

Figure 3. 7. Storage Modulus and Tan δ vs Temperature Curves: PS/PMMA/DB/AO(70/30/15/4wt%)-unfilled purple square PS/PMMA/DB/AO/Cloisite 20A (70/30/15/4/3 wt%)-unfilled blue circle, PS/PMMA/DB/AO/Cloisite 20A/*I*-MWCNT (70/30/15/4/3/2 wt%) –unfilled red cross, PS/PMMA/DB/AO/Cloisite 20A/*s*-MWCNT(70/30/15/4/3/2wt%)-unfilled black triangle, and PS/PMMA (70/30 wt%)-filled green square.

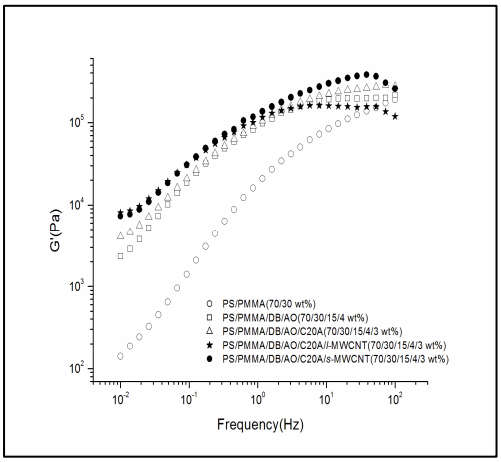

Figure 3. 8. G' vs Frequency Curves: PS/PMMA (70/30 wt%)-unfilled circle, PS/PMMA/DB/AO(70/30/15/4wt%)-unfilled square, PS/PMMA/DB/AO/Cloisite 20A (70/30/15/4/3 wt%)- unfilled triangle, PS/PMMA/DB/AO/Cloisite 20A/*l*-MWCNT (70/30/15/4/3/2 wt%) –filled star, and PS/PMMA/DB/AO/Cloisite 20A/*s*-MWCNT(70/30/15/4/3/2wt%)- filled circle.

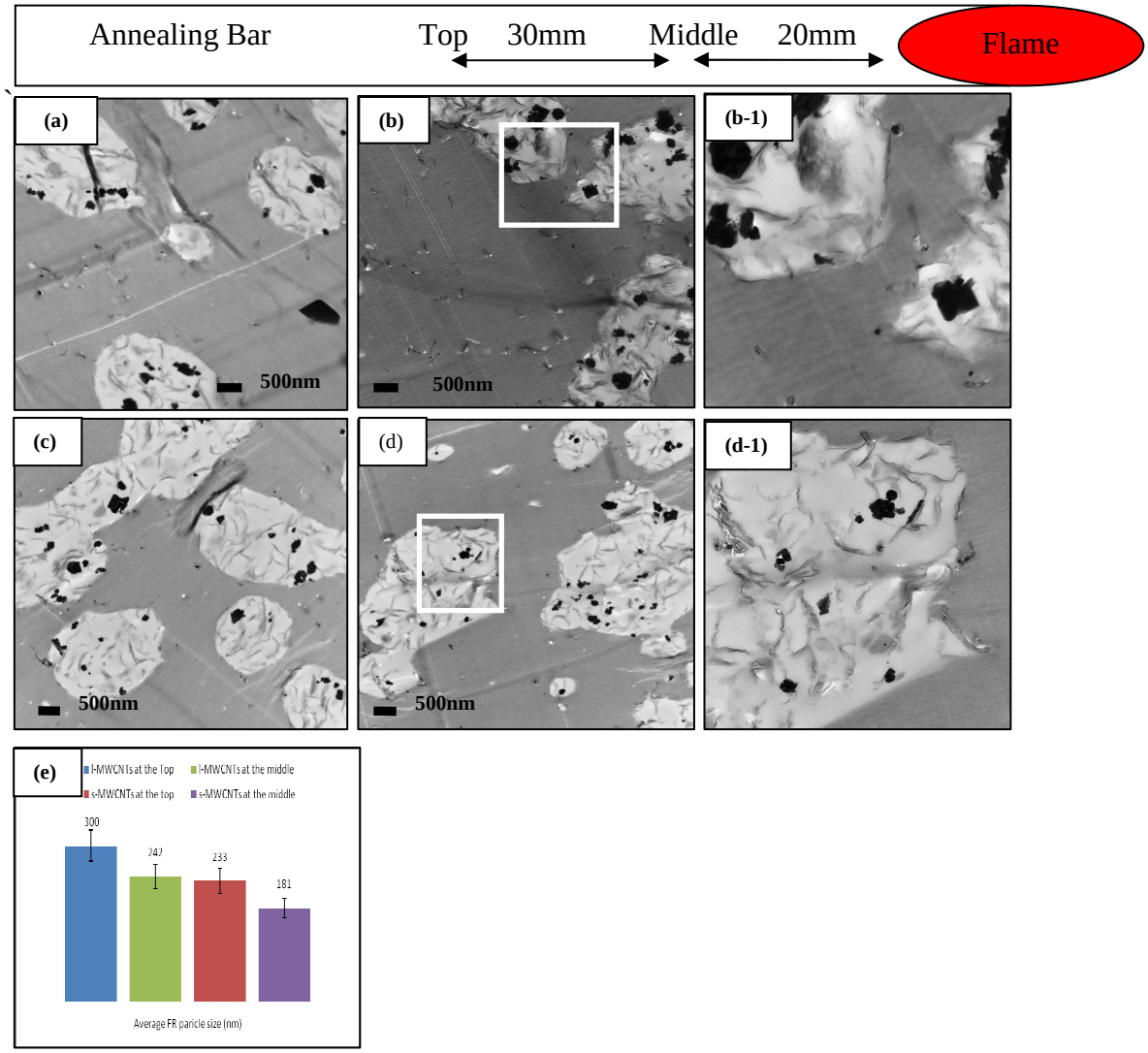

Figure 3. 9. TEM images of two series of *l* and *s*-MWCNTS annealing Bars: (a)-Top, (b)-Middle of PS/PMMA/DB/AO/Cloisite 20A/*l*-MWCNTs (70/30/15/4/3/2 wt%) Bar and (c)-Top, (d)-Middle of PS/PMMA/DB/AO/Cloisite 20A/*s*-MWCNT(70/30/15/4/3/2 wt%). (b-1) and (d-1): Higher magnification TEM images of (b) and (d). (e): The mean size of FR particles at each section in both the *l*-MWCNTs and the *s*-MWCNTs.

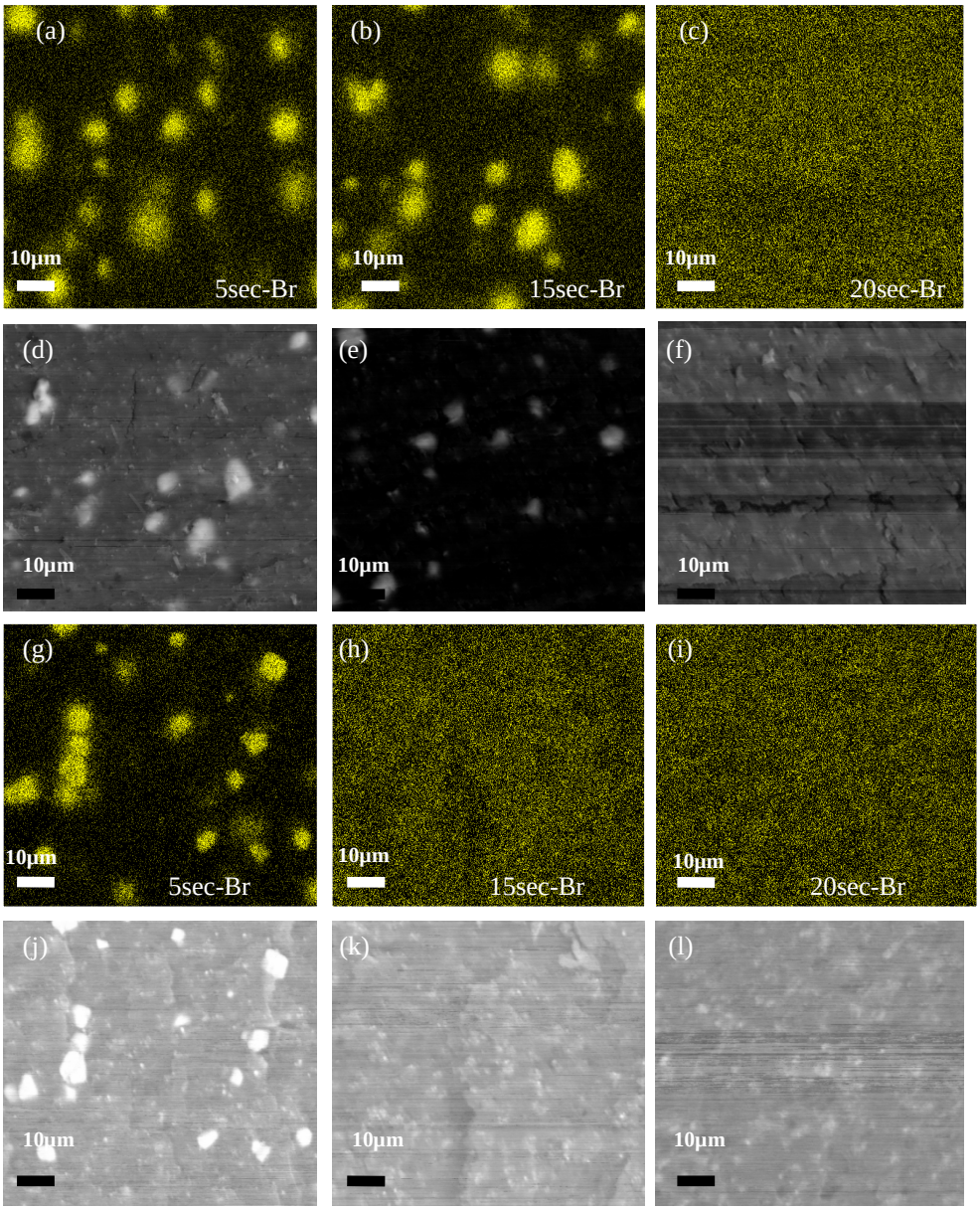

Figure 3. 10. Br Mapping and SEM images: (a)-(f) PS/PMMA/DB/AO/Cloisite 20A/*l*-MWCNT(70/30/15/4/3/2)samples, (g)-(l) from the PS/PMMA/DB/AO/Cloisite 20A/*s*-MWCNT(70/30/15/4/3/2) samples.

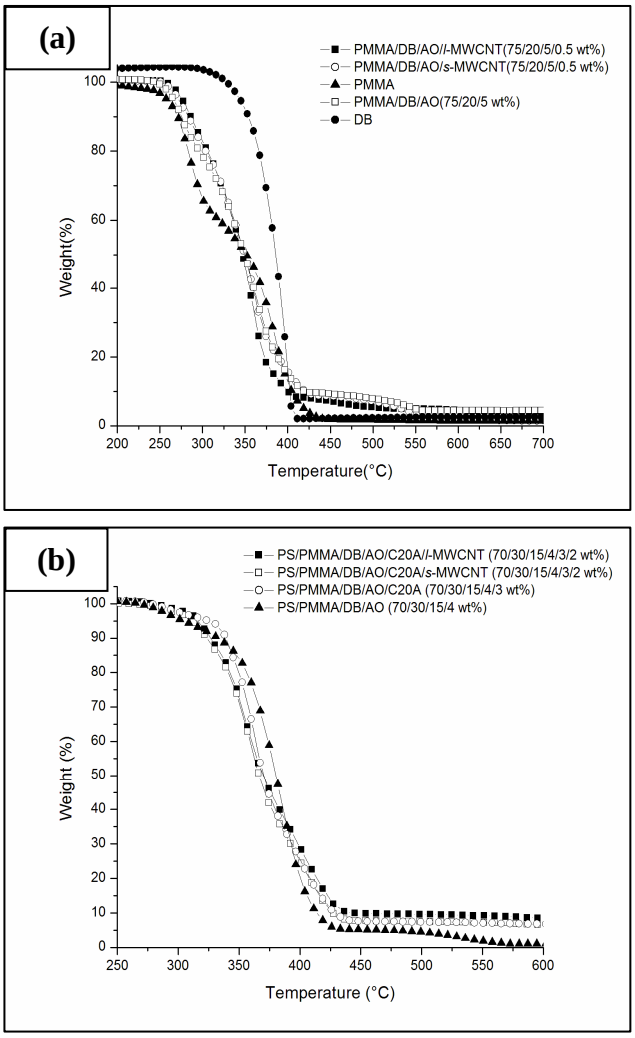

Figure 3. 11. (a) Curves of TGA from the PMMA polymer blends and (b) Curves of TGA from the PS/PMMA polymer blends.

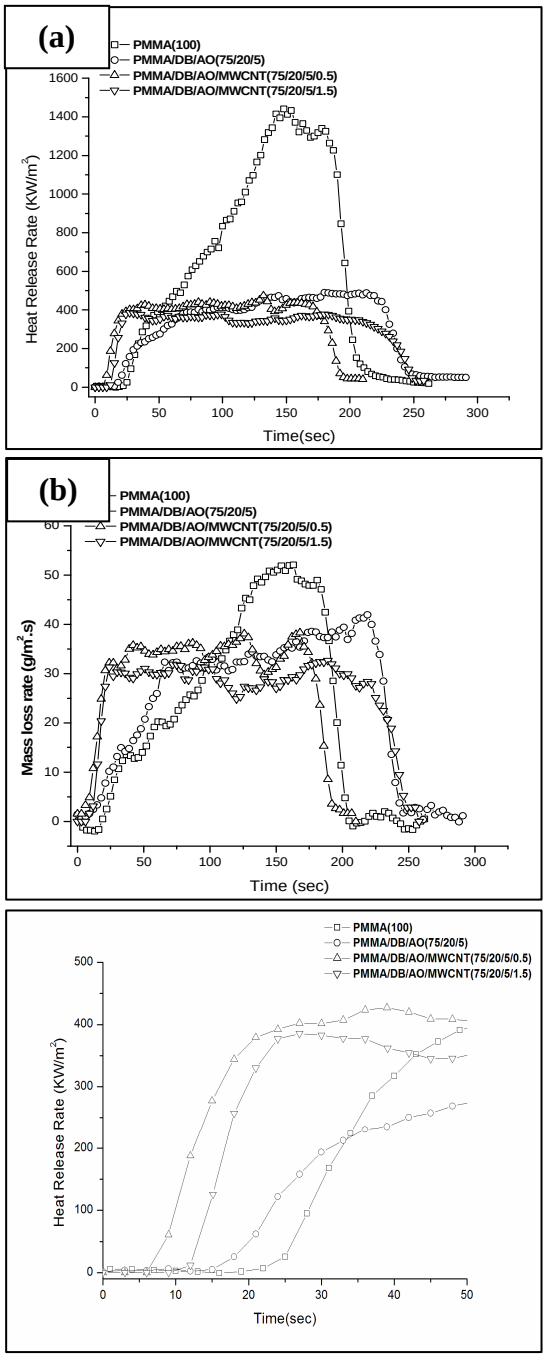

Figure 3.12. The Effects of addition of *l*-MWCNT on HRR and MLR in PMMA/DB/AO(75/20/5) at 50 kW/m^2.

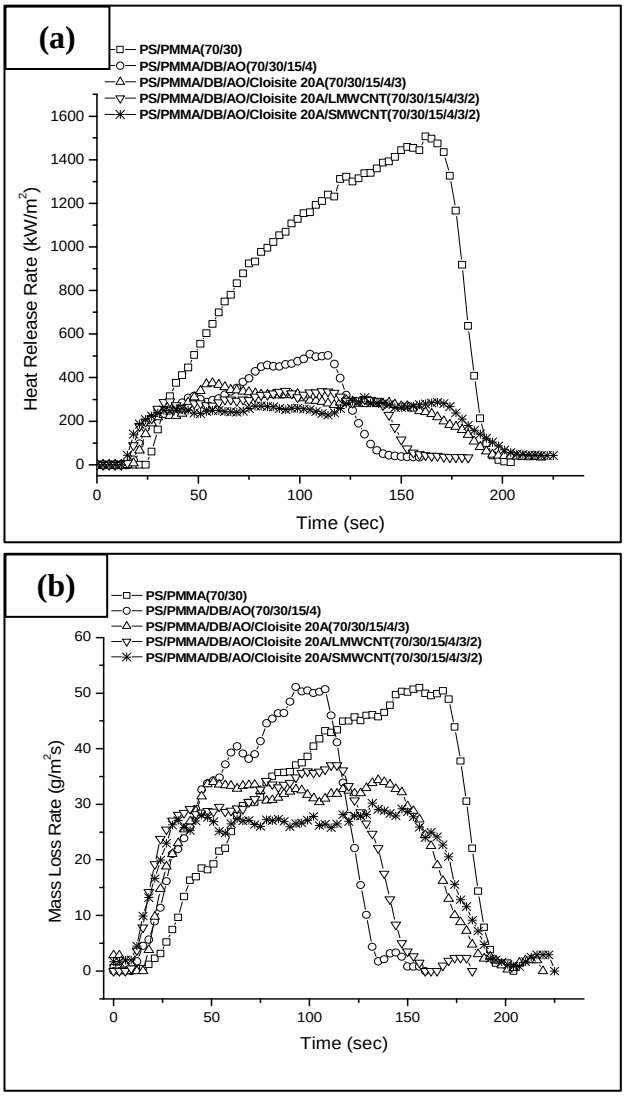

Figure 3.13. The Effect of MWCNTs and clays additives in HRR and MLR of PS/PMMA/DB/AO at 50 kW/m^2.

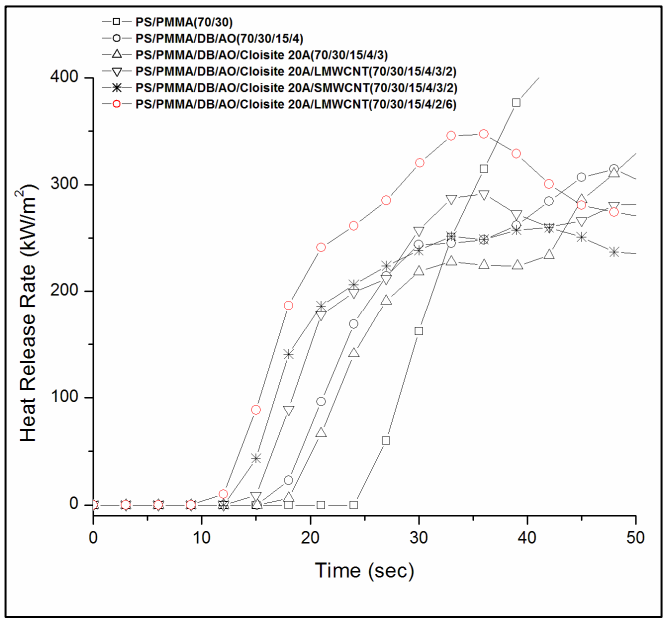

Figure 3. 14. The Effect of addition of MWCNTs and clays on time of ignition in HRR at 50 kW/m^2.

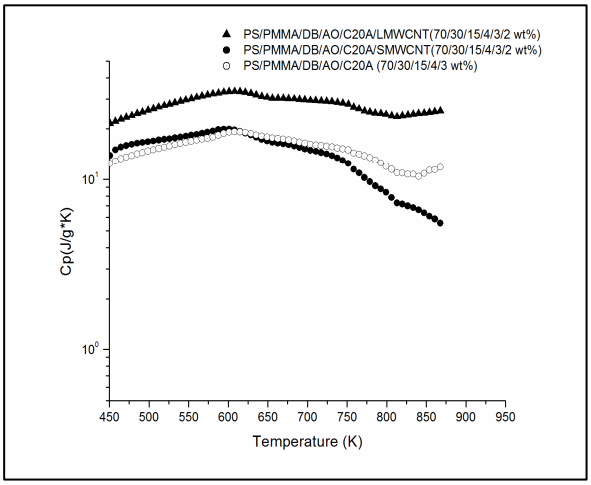

Figure 3. 15. Comparison of specific heat Cp of three different chars as a function of temperature: (1) PS/PMMA/DB/AO/C20A-unfilled circle, (2) PS/PMMA/DB/AO/C20A/*l*-MWCNT-filled triangle, and (3) PS/PMMA/DB/AO/C20A/*s*-MWCNT-filled circle.

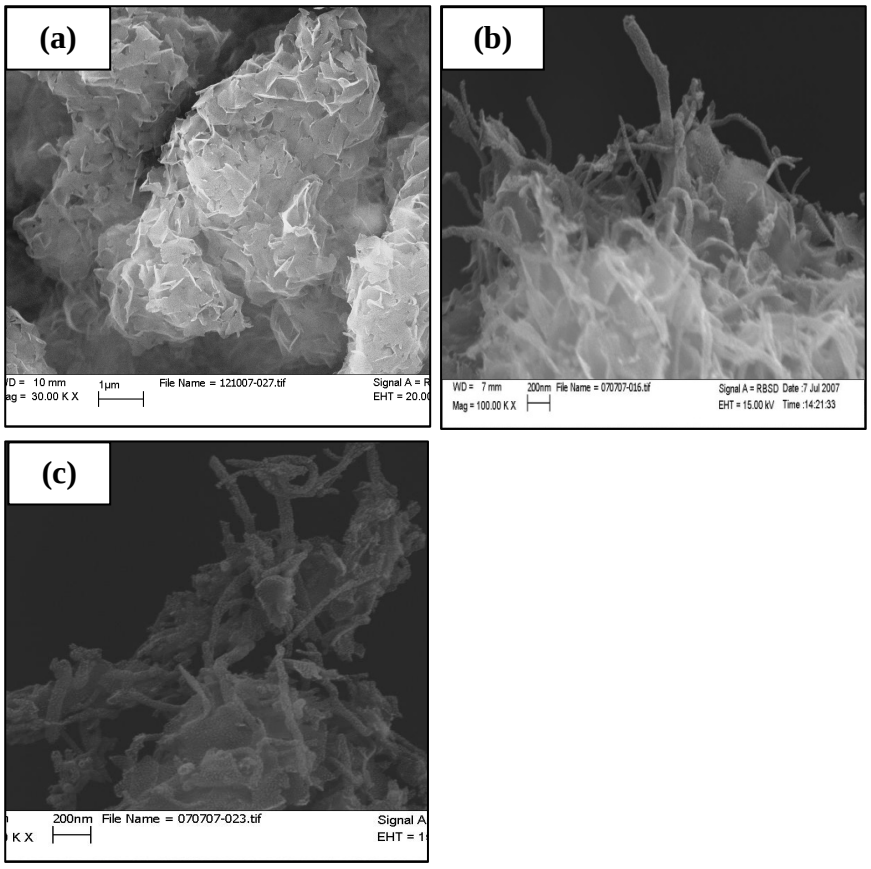

Figure 3. 16. SEM images of chars: (a)PS/PMMA/DB/AO/C20A/l-MWCNTs (b)PS/PMMA/DB/AO/C20A/l-MWCNTs, and (c) PS/PMMA/DB/AO/C20A/s-MWCNTs.

Sample (concentration wt%)	Dripping	UL-94VO	Sample burning total time (t_1+t_2)
PMMA (100)	Yes	NG	-
PMMA/DB/AO (75/20/5)	Yes	NG	-
PMMA/DB/AO/*l*-MWCNTs(75/20/5/0.5)	No	V0	<10sec
PMMA/DB/AO/*l*-MWCNTs(75/20/5/1.5)	No	V0	<10sec
PS/PMMA (70/30)	Yes	NG	-
PS/PMMA/DB/AO(70/30/15/4)	Yes	NG	-
PS/PMMA/DB/AO/Cloisite20A (70/30/15/4/3)	No	NG	-
PS/PMMA/DB/AO/Cloisite20A/ *l*-MWCNTs (70/30/15/4/3/2)	Yes	V2	<10sec
PS/PMMA/DB/AO/Cloisite20A/ *s*-MWCNTs (70/30/15/4/3/2)	No	V0	<10sec

* NG: No grading and burnt up to the upper clamp at the stand.

Table 3. 1. Results of UL-94V0 test from nanocomposites.

Sample (concentration wt%)	Tg(°C)	E'(Gpa) at T=35°C
PMMA (100)	125	2.44
PMMA /*l*-MWCNTs (100/0.5)	138	1.93
PMMA/*s*-MWCNTs (100/0.5)	135	1.97
PMMA/DB/AO (75/20/5)	138	3.34
PMMA/DB/AO/*l*-MWCNTs(75/20/5/0.5)	140	3.98
PMMA/DB/AO/*s*-MWCNTs(75/20/5/0.5)	140	4.15

Sample (concentration wt%)	Tg(°C)	E'(Gpa) at T=50°C
PS/PMMA (70/30)	122.7	1.85
PS/PMMA/DB/AO (70/30/15/4)	122	1.47
PS/PMMA/DB/AO/C20A (70/30/15/4/3)	121.9	1.77
PS/PMMA/DB/AO/C20A/*l*-MWCNTs(70/30/15/4/3/2)	124.3	2.87
PS/PMMA/DB/AO/C20A/*s*-MWCNTs(70/30/15/4/3/2)	125.3	3.61

Table 3. 2. Results of rheological properties from PMMA/MWCNTs nanocomposites and PMMA/DB/AO without MWCNTs and with MWCNTs nanocomposites.

Sample (concentration wt%)	Peak HRR (KW/m2)	Average MLR (g/s)	Ignition Time(sec)
PMMA (100)	1440.9	0.138	25±1
PMMA/DB/AO (75/20/5)	490.4	0.177	15±2
PMMA/DB/AO/*l*-MWCNTs(75/20/5/0.5)	436.7	0.172	5±1
PMMA/DB/AO/*l*-MWCNTs(75/20/5/1.5)	377.8	0.128	10±1

Table 3. 3. Results of cone calorimeter of PMMA/DB/AO without the clay and with the *l*-MWCNTs nanocomposites.

Sample (concentration wt%)	Peak HRR (KW/m2)	Average MLR (g/s)	Ignition Time(sec)
PS/PMMA (70/30)	1507.8	0.137	25±1
PS/PMMA/DB/AO(70/30/15/4)	570.0	0.131	18±2
PS/PMMA/DB/AO/Cloisite20A (70/30/15/4/3)	375.0	0.107	18±2
PS/PMMA/DB/AO/Cloisite20A/ *l*-MWCNTs (70/30/15/4/3/2)	338.4	0.113	15±2
PS/PMMA/DB/AO/Cloisite20A/ *s*-MWCNTs (70/30/15/4/3/2)	307.7	0.095	12±2

Table 3. 4. Results of cone calorimeter of PS/PMMA/DB/AO with the clay and with the clay and the MWCNTs nanocomposites.

Chapter 4: The Role of Surface Interactions in the Synergizing Polymer /Clay Flame Retardant Properties.

4.1. Introduction

The introduction of a solid particle in a polymer matrix can change the interfacial energy depending on the degree of interaction between polymer chains and the solid surface. As a result there have been numerous studies, both theoretical and experimental which have studied the effects of nanoparticles on the interfacial properties of binary polymer blend systems. In particular, if the particles have a sufficiently large aspect ratio, compared to the polymer chain diameters then adsorption could occur, leading to the reduction of the free energy of the entire system [59-68]. Theoretically, Lipatov et al, postulated that the energetic factors may be negative if the two polymers are strongly absorbed onto the surfaces of particles, thereby increasing miscibility [69-70]. Experimentally, Si et al.[31] demonstrated this principal using montmorillonite clays functionalized with dimethy-hydrogentated tallow, which they showed that the functionalized clays were able to partially compatibilize a large variety of polymer blends, and improved their thermal and mechanical properties. They explained their results in terms of the formation of in-situ grafts on the clay surfaces, which caused the platelets to segregate to the domain boundaries, thereby reducing the interfacial tension. The adsorption of incompatible polymers to clay surfaces was later explained by Koo et al.[71] to arise from only partial coverage of the platelet surfaces by the functional groups, resulting in the hydrophobic and hydrophilic areas.

However, this method of compatibilization has several disadvantages. The cation-exchange reactions used to mass produce the clays functionalized with alkyl quaternary ammonium chlorides involve the use of several toxic chemicals [11-12] and the degree of

surface coverage is not well known. The clays modified with quaternary amines are also known to be incompatible with styrenic monomers or the rapidly growing number of different bio-mass derived polymers, preventing their exfoliation when melt mixed with this rather large class of materials [31, 72-74, 49]. An alternate approach to inducing clay exfoliation is via the adsorption of oligomers into the clay galleries, screening the charges, and allowing for a shear-induced exfoliation. In this case, the requirements are that the oligomers, which are strongly adsorbed to the clay surfaces, interact favorably with mostly non-polar polymer matrices, and not be easily displaced when compounded in these matrices. These requirements can be contradictory and difficult to satisfy. For example, organic solvents, such as toluene and xylene, have been used to facilitate the exfoliation of clays in non-polar polymers such as polystyrene or polypropylene [75-77]. Due to the non-polar nature of the oligomers, this method was only used on di-tallow functionalized clays and the solvents used were even less thermally stable than the di-tallow surfactants, thereby increasing the thermal instability of the melts.

Here we show that resorcinol bis (diphenyl phosphate) (RDP), an oligomeric phosphate ester, can provide a good solution. The oligomer is a non toxic, easily soluble to both non-polar and polar solvents, and be having phosphory groups in its chemical formula, which can act as a strong hydrogen bonded accepters [78]. The material report has shown that it is thermally stable to above 300 degrees, and is in fact a component of some flame retardant formulations, where the content of phosphrous in the RDP oligomers is about 10.7 wt %. Thus, the oligomers have a surfactant nature, combining both polar and non polar moieties. As a result, we will demonstrate that they can be strongly absorbed to the unmodified Na+ clay surfaces, producing a uniform coating. Using complementary characterization techniques, we will show that these clays can be exfoliated, compatibilize blends, and reinforce their mechanical properties to the same degree as the clays functionalized with alkyl quaternary ammonium chlorides. In addition, we show that these clays can also have the same effects on styrenic polymer matrixes in which the functionalized clays have not been effective. Furthermore, since they are stable to high temperatures, the addition of RDP clays in where there is some degree of exfoliation, the polymers provide enhanced flame retardant properties.

4.2. Experimental Section

4.2.1. Materials

Cloisite Na^+, a montmorillonite (MMT-Na^+) clays, and Cloisite 20A (C20A) were purchased from Southern Clay Inc. The C20A was modified with a surfactant of dimethyldihydrogenated ammonium chloride. Its surfactant concentration is 95 meq/100g. Polystyrene and poly(methyl methacrylate) (PMMA) were purchased from Aldrich Sigma and Polysciences. Polycarbonate (PC), average Mw= 23K, and poly(styrene-co-acrylonitrile) (SAN with 24 wt % AN, known as Luran 358N) were obtained from Amco Plastic Materials Inc. A high impact polystyrene (HIPS) was received from BASF. The properties of polymers used in this study are tabulated in Table 4.1. A resorcinol di(phenyl phosphate) (RDP), known as Fyrolflex ® RDP, was used as a non-halogen flame retardant (FR) kindly provided from ICL-Supresta Inc.

4.2.2. RDP coated MMT-Na+ clays and nanocomposites preparation

In order to obtain the FR clays, the 20 wt% of RDP was first poured into a 200mL beaker and then the beaker was placed on a hotplate stirrer at a temperature of 80°C. Once the RDP in the beaker becomes liquid-like, the 80 wt% MMT-Na+ clays were inserted into the beaker. A mild stirring with a metal stick was performed for 15-20min.at the temperature in order to soak the clays with the liquid-like RDP effectively and then the beaker was stored in a vacuum oven at 100 ºC for 24 hours to completely soak the RDP onto the MMT-Na+. The final RDP clays were placed in a storage room before blending with polymers. As for the preparation of nanocomposites, a C.W. Brabender with two screw roller blades, Type EPL-V501, was equipped with a direct current drive (type GP100), where the heating chamber was used to mix polymers with nanoclays. The polymeric pellets were first inserted to the chamber at a rotation speed of 20 rpm at high temperatures. The nanoclays, such as C20A and RDP clays, were gradually added into the chamber and mixed at the same rpm for 2 min. The entire melt mixture was further blended at 100 rpm for 15 min. under nitrogen gas flow, which prevented degradation of

the mixture from heat-induced oxidation. The mixture was allowed to cool to room temperature in the chamber, and then using a hot press, small pieces of the mixture were molded into different shapes required for various experiments.

4.2.3. Small angle X-ray scattering (SAXS)

SAXS was performed with all samples (2 mm in thickness) to analyze microstructures of layered silicates. Since the silicates were a relatively rigid objects compared to the galleries, a strong scattering densities could be achieved when the galleries were fully intercalated into the layered silicates. The extended layered silicates with the galleries were corresponded to peaks in SAXS, where the scattering vector was only considered 1-dimensitonal to a normal direction of the incident beams because of the large density fluctuations from the rigid silicates in low scattering regions, which resulted in a circularly symmetric scattering. In the case of organoclays with polymer chains, the peaks could shift toward a lower scattering vector when the polymer chains were intercalated into the organoclays. Furthermore, when the polymer chains were more intercalated, the organoclays could be eventually delaminated into individual clay platelets, which was corresponded to no peaks. Thus, we could determine a degree of organoclays in terms of intercalation with polymer chains. The SAXS was conducted at a beam line X10A at National Synchrotron Light Source (NSLS) at Brookhaven National Laboratory. The wavelength used in the beam was 1.09 Å. The q range was from 0.03 to 0.58 $Å^{-1}$. The distance between the samples and the detector was 81.20 cm.

4.2.4. Transmission electron microscopy (TEM)

TEM was conducted with the cross sections from the nanocomposites. The thickness of the cross sections was 70-80 nm, which were cut by a Reichert-Jung Ultracut E Ultramicrotome and then were floated on deionized (DI) water surfaces. Later, few cross sections were placed on a coated copper mesh grid. The sections were directly viewed from a FEI Tecnai12 BioTwinG^2 TEM at 80KV and digital images were obtained from an AMT XR-60 CCD digital camera system. The RDP agents in the polymer matrixes were verified by an energy dispersive X-ray spectroscopy (EDXS) in the SEM

(LEO-1550) with a Schottky field-emission gun where the surfaces of RDP nanoclays were coated with a few micrometers of gold in order to make the specimens conduct.

4.2.5. Scanning transmission X-ray microscopy (STXM)

STXM was located at X-1A beam line at National Synchrotron Light Source (NSLS) at Brookhaven National Laboratory (BNL), was used in order to determine the chemical composition of polymer blends. The forced X-ray beam was confined into a 55nm Rayleigh resolution spot using a Fresnel zone plate.[79] The beam was able to scan the cross-sections with 70-80 nm thickness. The cross-sections were cut from the bulk compounds using a Reichert-Jung Ultracut E microtome and then they were lift on coated copper mesh TEM grids on DI water surfaces. The scanning process was performed outbound photo energies of components and the zone plate to the cross-section distance. Hence, the images and spectra were collected at the same time. The images at specific photon energies were representative to strong absorption of one of phases, where dark phases in the images were corresponded to high energy absorption and light phases were obtained at low energy absorption [80].

4.2.6. Atomic force microscope (AFM)

AFM was used to study for the surface morphologies of nanoclays. Since the clays and the substrates have different electron density functions as the tip was moved to the sample surface there was a good electron contrast between them. Thus, it was clear enough to observe the surfaces of clays. The AFM images were acquired with a Nanoscope IIIa from Digital Instruments. The measurements of contact angles with different polymer thin films were conducted in the contact mode. Si (111) substrates were prepared by a modified Shiraki technique, where small pieces of the Si substrates (0.5 x 0.5 inches) were immersed in a mixture of $H_2O/H_2O_2/H_2SO_4$ (3:1:1 vol.) for 15 minutes at 100 °C. After that, the Si substrates were washed with deionized (DI) water and then etched in HF/H_2O (1:4 in vol.) for 15 seconds at room temperature. The formation of monolayer clays were prepared by Langmuir-Blodgett (LB) technique. In the previous study [71], 20 mN/m was used as a surface pressure (π) in order to obtain a monolayer of

the clays on the etched Si substrates. The polymer solutions were spun-cast on glass substrates. The thin films (~100 nm) from the glass substrates were floated on the surfaces of DI water and then the thin films were lift on the Si substrates with monolayer clays.

4.2.7. Instrumented-indentation

Instrumented-indentation was performed using a nanoindenter (Micro Materials NanoTest) with a 5 µm radius of curvature diamond cone indenter. Depth controlled indentations were performed with the maximum depth set to 2 µm. Char samples were mounted with an epoxy adhesive to aluminum sample holders for testing. Due to the large variation in char topology, regions were identified using a light microscope, which were flat and free of pores. Load-displacement data was obtained using a constant loading and unloading rate of 0.1 mN/s. The typical maximum loads reached were on the order of 9 – 12 mN. A 5 sec. hold segment was taken at the maximum displacement before unloading to take into account creep effects. On each sample, three identical indentations were performed with a minimum spacing interval of 60 µm between successive indents to ensure no interaction between residual plastic deformations. To determine elastic modulus of the char material, the slope (S) of the initial unloading data in conjunction with the spherical contact area is used in the conventional Oliver and Pharr method to determine a reduced modulus [98]. The contact radius as a function of the plastic depth (h_p) of the char is given as:

$$a = \sqrt{2Rh_p - h_p^2},$$

where R is the radius of the indenter (5µm) and h_p is the average of the residual and maximum depth of the indentation. The reduced modulus (E_r) can be written as:

$$E_r = \frac{3}{4}\frac{S}{\left(2Rh_p - h_p^2\right)^{1/2}}$$

where S is the slope of the unloading curve, and E_r is represented by:

$$\frac{1}{E_r} = \frac{1-\nu_s^2}{E_s} + \frac{1-\nu_i^2}{E_i}$$

With knowledge of the elastic modulus and Poisson's ratio of the indenter tip (E_i = 1141 GPa, and v_i = 0.07) it is possible to determine the elastic modulus of the chars (E_s) from the reduced modulus, assuming a char Poisson ratio of v_s = 0.5, typical for incompressible materials. Hardness (H) of the chars was calculated by the ratio of the maximum applied load (P_{max}) divided by the contact area ($A = \pi a^2$). The reported material properties of the char surfaces were averaged over three discrete indentations.

4.2.8. Mechanical and thermal analysis and FT-IR spectroscopy.

Elastic modulus and tan delta of the samples was performed using a Mettler Toledo DMA/SDT 861e in the single cantilever mode. The samples were molded into bars of dimension 10 mm x 10 mm x 2 mm and then measured as a function of temperature. The range of temperatures was from room temperature to 180 °C at a rate of 2 °C /min with a frequency of 1 Hz. Thermogravimetric analysis (TGA) was conducted at a Mettler-Toledo 2000 analyzer in order to compare the RDP clays with the C20A clays in terms of the rate of mass loss of the clays in the N_2. The mass of samples (8-10 mg) were placed into an aluminum crucible. The crucible with the mass was put on the small dish at the furnace in the TGA and then the temperature was raised from 30 °C to 800 °C at a rate of 10 °C/min. The FT-IR spectra of RDP and clays were obtained from MAGNA-IR 760 spectrometer made by Nicolet. The samples were first mixed with KBr powder and then were hydraulic-pressed to a pellet for FT-IR spectroscopy.

4.3. Results and Discussion

4.3.1. RDP coated nanoclays.

4.3.1.1. Morphology and X-ray scattering.

In figure 4.1 we show the scanning force microscopy images of RDP coated MMT-Na+ and uncoated MMT-Na+ clay monlayers which were produced by lifting from the air water interaface onto a Si wafer. In the figure we see the distinct outline of the platelets both in height and lateral friction scans of the unmodified. The outline of the platelets is more difficult to observe on the coated samples. The surfaces of both types of clays are relatively smooth topographically. This indicates that the RDP coating is fairly uniform. In figure 4.1c and 4.1f we also show a cross sectional scan of the coated and uncoated platelets, where we can see that the uncoated ones are 1.36 nm in height while the coated ones are 3.52 nm in height. We could then estimate the height of RDP surfactant layer coating the clay surfaces, was about 2.2 nm. In figure 4.2 we show SAXS spectra of the coated and uncoated clays. From the figure we can identify the characteristic peak in the unmodified clays, at q = 0.50 $Å^{-1}$, which is in agreement with previously reported results and corresponds to d = 1.25 nm the [001] direction. A large shift in the characteristics peaks is observed for the RDP clays, where the [001] peak is observed at q = 0.282 $Å^{-1}$ and even the secondary [002] peak is observed at q = 1.14nm. Using the $d = 2\pi/q$, and substituting q = 0.282 $Å^{-1}$, we find that the interlayer spacing has increased to 2.23 nm as in the direction of [001], which is in excellent agreement with the value measured on the scanning force microscope images. For comparison we also show the x-ray scattering data obtained from a Cloisite 20A monolayer lifted by the same LB technique from the air/water interface. Here the primary peak is seen to shift to q = 0.2319 $Å^{-1}$, which corresponds to an interlayer spacing d = 2.7 nm in the [001] direction, in good agreement with previously reported data [71], and somewhat thicker than the RDP layer.

4.3.1.2. Thermal stability

TGA analysis was performed. From figure 4.3 we can see that approximately 5 % of mass loss on unmodified MMT-Na+ clays occurs at around 100 °C due to the vaporizations of moiety molecules unbounded onto the clays. However, in the case of Cloisite 20A, only 2.5 % of mass loss is obtained before the major decomposition undergoes around 250 °C. This mass loss could be indicative that the di-tallow molecules are firmly confined into the clays, which could lead to the strong interactions between polymer chains and the surfactants in the direct intercalation of polymer melt.[14, 81] On the other hand, the RDP coated MMT-Na+ clays also have the small mass loss before the clays start to decompose at round 300 °C. The higher decomposition temperature could be mainly contributed to the decomposition of RDP, which degrades at 288 °C (about 5 wt% loss) [14]. However, the extra increase of decomposition temperature (about 12 °C) may result from a synergic effect, where the RDP coated clays could be more stable on higher temperatures.

The synergic effect on the presence of RDP on the clay surfaces could be contributed to the spectra of RDP coated MMT-Na+ in FT-IR as well. From figure 4.4 we can see that the unmodified clays show typical characteristic absorption bands, 1047 cm^{-1}, 3448.27 cm^{-1} and 3629.97 cm^{-1} which corresponds to one of Si-O stretching regions, O-H stretching regions, respectively. In particular, the Si-O stretching band separates into the two peaks, 1008 cm^{-1} and 1078 cm^{-1} when the RDP is incorporated. Yan and Cole founded that the peak II (~1080 cm-1), which is out-of plane mode, became visible clearly as the content of water or compatiblizer increased into the clay interlayers.[83-84] Thus, it is clearly indicative that the RDP oligomers are intercalated into the clay galleries. Furthermore, The RDP IR spectrum shows that there are the phosphorus-oxygen double bond stretching (P=O) at ~1300 cm^{-1} and the phosphorus-oxygen single bond stretching (P-O) at ~960 cm^{-1}. The absorption band of the P=O still appears at the same position in the RDP clays spectrum. However, the P-O absorption band might be shift to at 1008 cm^{-1}, which may result from the presence with hydrogen bonding. Since the phoshoryl group (P=O) in the RDP oligomers are well known as a strong accepters for hydrogen bonding [78], the RDP oligomergs would be self-assembled in the clay

galleries, which could be biocompatible to bio-mass polymers, such as starch, which will be presented in the following report.

4.3.1.3. Contact angle measurements

In order to determine the relative affinity for the polymers, the RDP coated clays or the Cloisite 20A clays, films of spun cast PS or PMMA were floated on top of the LB monolayers and annealed for times up to 48 hours at T = 180 °C. The results are shown in figure 4.5. At this temperature the surface tensions of PS and PMMA are nearly equal (γ ~ 29 mN/m) [85]. and hence differences in the contact angle are mostly due to differences in the interfacial energy between the polymers and the surface. Since the surfactant layers on clays are thin and strongly adsorbed our system can be followed by Young's law rather than a Neuman construction [86]. We can assume that the observed angles correspond to the Young's contact angle,

$$\gamma_A = \gamma_B \cos\theta + \gamma_{A/B} \qquad (1)$$

, where γ_A and γ_B are the surface tension of the A and B phases, and $\gamma_{A/B}$ is the interfacial tension between the A and B phases. From the figure we can see that the contact angle for PS on RDP covered clays reaches an equilibrium value of 7.7 degrees after 24 hours of annealing and does not change significantly after additional annealing of another 24 hours. The PMMA film, on the other hand, appears to wet on the RDP coated clay surfaces and the holes initially formed upon deposition of the PMMA film do not seem to increase in diameter, nor do droplets form on the surface after 48 hours of annealing.

In order to determine the interfacial tension between the RDP coated clays and the homopolymers we first had to find the surface energy of RDP as a function of temperature. This was performed using the Wilhelmy plate method on a volume of 78 cm^3 of RDP heated from ambient to 80 °C. The data are shown in figure 4.6a, where we derive the equation,y = -0.1082x + 51.203, and from which we can extrapolate a value of 31.7 mN/m at 180 °C. Substituting this value for γ_A in equation 1 we find that $\gamma_{A/B}$ is 2.75 mN/m and 2.8 mN/m for RDP with PS and PMMA respectively, which is shown in

table 4.2. We can now determine whether PS or PMMA will wet the RDP coated clays at T= 180 °C, or the conditions used in melt mixing the nanocomposites. The spreading coefficient S is given by:

$$S = \gamma_{RDP} - \gamma_{Polymer} - \gamma_{RDP/Polymer} \qquad (2)$$

,where wetting occurs when $S > 0$. Hence for PS we obtain $S = -0.25 < 0$ and for PMMA $S = 0 \sim 0$, which is consistent with the observation that PMMA completely wets the RDP coated clay surface, whereas PS does not. Therefore, the RDP coated clays are expected to exfoliate in a PMMA matrix, in order to expose more interfaces. This observation is confirmed in the TEM image shown in figure 4.6b. In the case of PS, the spreading coefficient is only slightly negative, and the some exfoliation can occur when shear is applied. TEM images of RDP clay nanocomposites with HIPS are shown in figure 7, where a high degree of exfoliation is observed.

In figure 4.5 we show the contact angles obtained on Cloisite 20A monolayers. In this case we find that the angle of PS is rather high, or 32 degrees, indicating that a large unfavorable interfacial tension exists. This is a good agreement with the known lack of exfoliations of the Cloisite 20A in PS matrices. The angle with PMMA, on the other hand, is only 2 degrees, which is consistent with the known ability of PMMA matrices to exfoliation of the Cloisite clays under shear.

4.3.2. Nanocomposites

4.3.2.1. Homopolymers.

In order to examine the degree of exfoliation of the RDP clays in thermoplastic polymers, such as a high impact polystyrene (HIPS), poly(acrylonitrile butadiene styrene) (ABS), and polypropylene (PP), we performed SAXS experiments and compared the results with TEM images, for polymers which could be cross sectioned at ambient temperatures.

From figure 4.7a we show the SAXS data for HIPS nanocomposistes with either 5% Cloisite 20A or RDP coated clays and we plot the data for just the clays as a reference point. From the figure we see that in the nanocomposite with Cloisite 20A the [001] as well as the [002] scattering peaks are clearly visible, and of comparable intensity to the peaks of the pure clays. From the shifts in the peaks we find that the interlayer spacing has increased further to 4.1 nm, which indicates that most of the clay are intercalated, rather than exfoliated, with a layer which is approximately 1.4 nm thick of polymer. In contrast, for the HIPS/RDP clays nanocomposite, no scattering peaks are observed, which is consistent with most of the clays being exfoliated. This is further confirmed by the TEM micrographs shown in figure 4.7c-d. In figure 4.6c we show a typical cross sectional image of the HIPS/Cloisite 20A nanocomposite, where we see large tactoid-like structures, where the clay platelets are intercalated with polymers. From the inserted TEM image we can estimate the mean distance between platelets to be 4.2 nm, in a good agreement with the scattering data. In contrast, from figure 4.6d we can see a typical cross sectional image of the HIPS/RDP-Clay nanocompoiste. Here mostly individual platelets are seen, which would not produce diffraction peaks, confirming the exfoliated nature. These results are consistent with the contact angle measurements shown previously, where the interfacial tension between PS and RDP coated clays was found to be much smaller than that with the di-tallow coated clays, facilitating the exfoliation of the RDP coated clays during shear mixing.

Exfoliation is also more efficient at modifying the mechanical properties, than intercalation. This is also demonstrated in figure 4.7b where we plot the dynamic modulus and tan delta of HIPS/clay nanocomposites, obtained from DMA measurements as a function of temperature. From the figure we see that in both cases the addition of clays does not affect on the melting temperature, which remains as same as the HIPS homopolymer. On the other hand, we see that the addition of RDP clays increases the modulus by nearly a factor of 2 for $T<Tg$, whereas the addition of Cloiste 20A slightly decreases on the modulus, which is consistent with the poor mixing of the Cloisite clays with the polymers.

In figure 4.8 we show the SAXS data obtained for another nanocomposite with styrene groups, ABS with 3, 5 and 10 wt % RDP clays. Here we also find that the clays

diffraction peaks are not observed, while the TEM cross sectional image indicates a good exfoliation. The storage modulus of the nanocomposites with RDP clays increases by nearly an order of magnitude compared to that of homopolymer, which could mainly result from the fully exfoliation of the clays. Since the increase in the rubber fraction did not seem to affect the degree of exfoliation, we also attempted to blend the RDP clays with polypropylene (PP) homopolymer, another polymer in which numerous authors have reported difficulties with Cloisite 20A. The SAXS data is shown in figure 4.9a, where we find only a small trace peak at the position of the RDP-clays [001] indicating most of the clays are exfoliated. This is further confirmed by the DMA data shown in figure 4.9b, where we see that the storage modulus of the RDP clays nanocomposite is higher than that of the PP homopolymer up to the melting temperature.

4.3.2.2. Polymer blends

Blends of PMMA with either PS or PP: In figure 4.10 we show the SAXS data from blend samples composed of 30 % PMMA with either 70 % PS (figure 10a) or 70 % PP (figure 4.10b). The scattering peaks of the pure RDP coated clays are also plotted for comparison. In each case we see no remnant of the clay peaks indicating that a full exfoliation has occurred. In the previous paper [37], we claimed the partial compatibilization of the PMMA/PS blend when Cloisite 20A was added, yet the SAXS data indicated the presence of the clay peaks intercalated with the polymers. High and low magnification TEM images of both of these blends are shown in figure 4.11a-b. From the figures we conclude that the absence of the clay peaks in the SAXS data do not necessarily correlate with compatibilization. In the case of the PS/PMMA blend, the clays are entirely segregated within the PMMA phase, where they appear exfoliated. In contrast to the TEM images of ref.[31], no platelets are observed at the polymer phase interfaces, and hence no effect of the RDP coated clays can be seen on the compatibilization of this blend. In the case of the PMMA/PP blend, most of the clays are still in the PMMA domains, where they can also exfoliate, as they do in the homopolymer. In contrast to the TEM images for the blend with PS, some of the platelets are seen to be adsorbed onto the phase interfaces, which could lead to an increase of the dynamic modulus overall

temperatures compared to the blend without the RDP coated clay. It is shown in figure 4.10c.

From the contact angle data shown previously we have demonstrated that PMMA wets the surfaces of the RDP coated clays, while PS dewets the surfaces. During the melt mixing process at high temperatures the PMMA chains will preferentially be adsorbed onto the RDP coated clay surfaces, forming *in situ* grafts composed almost entirely of PMMA chains. Hence the RDP coated clays will segregate exclusively in the PMMA domains, and no reduction of the overall energy of the system occurs when these platelets are placed at the phase interfaces. Furthermore, the interfacial energy between PS and PMMA, $\gamma = 1.2$mN/m at 180 °C [85, 87], is lower than either of the interfacial tensions (table 4.2) between either of the blend polymers and RDP, no energetic advantage is obtained through segregation at the interface. Hence the RDP coated clays are massively segregated in the PMMA phase, where their interfacial energy is minimized, and no change in the blend compatibility occurs.

In figure 4.11 we show TEM data corresponding to a PP/PMMA blend. In this case some compatibilization is observed in the lower magnification images, while some clays at the blend interfaces are observed in the higher magnification image. Since the interfacial tension between PP/PMMA has been reported that the values are 4.5 mN/m [88] at 240 °C and 7.50 mN/m [89] at 200 °C we could calculate the interfacial tension of blend is ~ 9 mN/m at 180 °C or significantly higher than that between RDP and PMMA. As we have shown that the RDP clays exfoliate in PP as well, we can estimate that the interfacial tension with PP would be comparable to that with PMMA, and hence placing the RDP clays at the polymer interfaces can reduce the overall energy of the system, and result in partial compatibilization [31, 37].

*PC/SAN24 blend***:** From figure 4.12a-c we can see TEM images of cross-section samples of a PC/SAN24 blend. In both cases we find either Cloisite 20A or RDP coated clays are fairly intercalated rather than exfoliated. This observation is consistent with the SAXS data obtained from these samples, shown in figure 4.12d, where peaks are observed corresponding to either Cloisite 20A or RDP coated clays, with large intergallery spacings corresponding to an intercalated system. In addition, the

intercalation of RDP coated clays could be stable up to 450 °C in which the peaks still remain at the high temperature in figure 4.12e.

We also confirmed that the addition of the RDP clays improved the compatibility of the polymer blend using the STXM technique. In figure 4.13 we show a STXM images obtained from a symmetric PC/SAN24 blend mixed without clays and either with 5 % Cloisite Na+ or 5 % RDP clays, which were cross sectioned after removal from the Brabender. In the figure, PC and SAN24 correspond to the light and dark areas, respectively. From the figure we can see that in the absence of clays, the domains are well separated from each other. The addition of Cloisite Na+ clays further enhances the phase segregation, probably due to segregation of the clays in the PC phase (figure 4.13b). However, the addition of 5 % RDP coated clays dramatically changes in the morphology of the blend, where the domains become bicontinous and smaller than the resolution of the image (50 nm). This phase segregation can be explained by minimizing the interfacial energy of the blend. In order to quantify the energy, we can apply the values of surface tension for PC and SAN24, reported in literatures. We found that the interfacial tension for PC/SAN24 blend was ~ 2.8 mN/m [90, 93]. , and the surface tension for PC at 200 °C was 29.1 mN/m [94]. Since we know the temperature dependence of the surface tension for the RDP oligomers we can calculate a value of the surface tension of RDP is 29.6 mN/m at 200 °C. Hence we can see that the spreading coefficient S_{PC} on RDP clay surfaces almost is zero without adding the interfacial tension between PC/RDP. If $S_{PC} = 0$, $\gamma_{RDP/PC}$ is 0.5 mN/m. Although values of the surface tension for SAN24 at 180 °C is not available, The surface tension for SAN24 can be calculated using the temperature dependence of polystyrene ($-d\gamma/dt = 0.072$) [85, 94] γ_{SAN24} is 35.3 mN/m at 200 °C. As we can see that the spreading coefficient S_{SAN24} on RDP clay surfaces is already negative. Thus, when the SAN24 polymer melts dewets, and a value of $\gamma_{RDP/SAN24}$ would be higher than that of $\gamma_{PC/SAN24}$. Therefore, the maximization of reducing the interfacial energy could occur when all of RDP coated clays segregate at the interfaces, while increasing the compatibility.

Furthermore, we could also confirm the blend on the compatibility by obtaining a single Tg. From figure 4.14a we can see that the blend has two distinct glass transition

temperatures in which one is about 127 °C for SAN24 and the other is about 170 °C for PC. When the MMT-Na+ clays are added, the two Tg still exist at near the positions. As expected, when the addition of Cloisite 20A clays are added the two Tg becomes the single Tg, about 128°C. We also measure the Tg of the blend with RDP coated clays. From the figure we can see that the addition of RDP coated clays obtains a single Tg, which is about 122 °C. Thus, the formation of single Tg could result from an increase of the compatibility, which is a good agreement with both the TEM and STXM images. In addition, the measurements of dynamic modulus as a function of temperature could explain that the RDP coated clays act as a compatibilizer. From the figure 4.14b we can see that in the case of RDP coated clays the storage modulus gradually decreases as temperature increases compared to the others clays, where the storage modulus are constant up to 95 °C. This difference on the modulus could result from the extra RDP oligomers in the clay galleries. It could lead to an increase of loss modulus during heating. Therefore, the addition of RDP coated clays could make the polymer matrix ductile, which may increase impact toughness of the polymer blend.

4.4. Application

4.4.1. Cone calorimetry

As has been discussed in several previous publications [37, 64], rendering polymer blends flame retardant can pose a significant challenge. The combustion behaviors of polymers involve a complex sequence of condensed and gas phase reactions. In blends, the additional phase segregation during heating further complicates the situation, and degrades the resistance to combustion. We have previously shown that the addition of Cloisite clays can stabilize blends against phase segregations and catalyze reactions which lead to chars formation. In the case where exfoliation occurred in at least one of the components, the addition of organoclays was observed to decrease the heat release rate (HRR) and mass loss rate (MLR) [37, 64].

Here we will compare the flame retardant properties of blends where the RDP clays have been added, rather than the Cloisite organoclays. In figure 4.15a-b we show the HRR and MLR of the PC/SAN24 blends performed in nitrogen atmosphere. From the figure we find that the addition of Cloisite 20A only decreases the maximum HRR slightly but has nearly no effect on the MLR. In fact, a closer examination of the time dependence shows that Cloisite 20A degrades the performance of flame retardancy and decreases the total heat loss and mass loss time, which is somewhat consistent with the previous reports that the di-tallow coating of the organoclays is combustible, and can decrease the time to ignition in nanocomposites [37, 64]. The addition of MMT-Na^+ clays improves the performance, but the addition of RDP coated MMT-Na^+ clays indicates a major improvement on the HRR and the MLR. From the figure we find that the peak HRR is decreased by more than a factor of 2, and the MLR is decreased by 30%, while the total combustion time is nearly the same amount in the PC/SAN24 blend. This behavior also appears to be correlated to the characteristics of the chars, which can be seen in video clips obtained during the gasification test.{see the supplementary materials}. PC is known to be a good char former even though styrenic co-polymers such as SAN are not. All blends, with and without clays are observed to form chars, and the amount of carbonaceous chars were calculated after subtracting the inorganic components,

which is listed in table 4.3. From the table we can see that the largest amount of char residues is found in the unfilled blend, while the addition of clays reduces the total carbonaceous chars by more than 45 %, regardless of the type of clays. Hence the difference in the flame retardant performance with the addition of clays is not strictly a function of the ability to form char.

In figure 4.16 we show still images of the samples obtained from the video clips. From the figure we find that the char forms very quickly and then begins to swell with the gases from thermal decomposition of the blend, finally build up the pressure inside. In the case of the unfilled blend, and that containing RDP clays, a decrease in both MLR and HRR is observed when the char becomes thick enough to contain the gases and a "mushroom" structure is formed. In the case of the blend containing Cloisite 20A, the char collapses very quickly with the gases build up and no mushroom-like structures is formed. As a result, the thermal decomposition progresses very quickly and no reduction in the MLR and the HRR is observed.

The morphology of the chars was further studied using SEM and EDAX. In figure 4.17 we show the chars formed in the blend without clay. The box signifies the location where EDAX analysis was performed. In the EDAX spectrum we find primarily carbon, which is expected in the char. The morphology image at 20 micron magnifications shows that the char is fairly uniform, while the image at 100 micron magnification shows with what appear to be "vent holes" type of formations. Some of these "vents" are covered with membranes, while others have ruptured membranes, or membranes blown away. This morphology is consistent with the "mushroom" observed to form in the optical images. As the mushroom forms, the rate of gases released decreases, but is not completely stopped. The SEM images show that a uniform char layer is formed, but the gases can still escape from the holes. The chars from the blends with RDP or MMT clays have similar morphologies, with what appear to be membrane covered vent holes. The high magnification images show a uniform structure, which the EDAX spectra indicate that the membrane is mostly carbonaceous material. The Si/Mg/Al peaks, which are characteristic of the clays, are very small in comparison to the C peak, from the char. Since the clay platelets do not decompose and are still in the char the EDAX spectra indicate that they must either be in the interior of the chars or remain

dispersed within the surface layer (at the 5 % level) allowing the carbonaceous "skin" to form. Not surprisingly the appearance of this "skin" is similar to that observed in the blend without clays.

The images of the char with the Cloisite 20A clays are shown in figure 4.17 where a sharp contrast is immediately observed. The high magnification image shows that the structure of the char is almost entirely composed of compacted clay platelets. This is confirmed by the EDAX image, where the Al/mg/si peaks predominate and only a small C peak is observed. These images indicate that upon heating the Cloisite 20A clays segregates to the surfaces of the sample, possibly due to the large unfavorable energy with the matrix. In contrast to the previously reported results for PS/PMMA, where the polymer did not form a char, and the clay "char" was the only means of preventing heat and mass loss, in this case, the PC/SAN blend does form a good char. The clays appear to interfere with this char layer. The large magnification image shows that the morphology of this resultant char is very porous, as opposed to the char of the pure blends. The high degree of porosity is consistent with the inability of this char layer to contain the combustion gases, resulting in the poor flame retardant behavior.

Another factor which may impede the formation of the "mushroom" structure is the hardness and the elastic modulus of the chars. In order for the mushroom structure to expand, while containing the gases, the material must be relatively elastic; otherwise the internal pressure will produce cracks, which release the gases and accelerate combustion. We therefore used nanoindentiation to measure both the elastic modulus and the hardness of the chars (shown in figure 4.18). The results of the nanoidentation tests are shown in figure 4.19. From the figure we can see that the modulus of the char formed by the unfilled blend is the smallest, E' = 1.3 GPa, while its hardness is intermediate. The unfilled blend is able to form an intumescing char, but the larger hardness to modulus ratio indicates that it is somewhat brittle and, as can be seen in the images, unstable. Hence the flame retardant performance is not satisfactory. The addition of Cloisite 20A deteriorates the performance even further. Here we can see that the modulus, as well as the hardness, is nearly 400 % larger than for the other materials, and the mushroom-like structures are unable to form altogether. The modulus that we measure, E'= 4.9 GPa is larger than E'= 2.3 GPa of the Cloisite Na^+ or the RDP clays filled system, but still

smaller than that of pure montmorillonite clays E'= 14 GPa [96-97], indicating that despite the high concentration of clays, there may be other deposits of the polymer char left. The chars formed by the Cloisite Na^+ and RDP clays have similar hardness and modulii, where the modulii are larger than that of the pure blend, but the hardness is lower, indicating more elastic behavior. In both cases, the mushroom-like structures are able to form which contain the gases. We can only postulate, therefore, the superior flame retardant responses of the blends containing the RDP clays over those containing the Na clays, may be the presence of the adsorbed RDP on the clay surfaces, which catalyzes the reactions needed for further reduction of the HRR and MLR.

4.5. Conclusion

The absorption of resorcinol di(phenyl phosphate) (RDP) oligmoers on clay surfaces has been proposed as a replacement for di-tallow molecules commonly used in functionalizing clays. Using SAXS, we showed that RDP can be adsorbed on the surfaces of sodium montmorillonite clays, thereby increasing the interlayer spacing from 1.25 nm to 2.23 nm. We then demonstrated, using SAXS and TEM that these modified clays can be exfoliated in styrenic polymers: HIPS and ABS, well as in PP. We also produced single layers of the clays, using the LB technique and measured the contact angle of polymers on the surface, which were consistent with the ability to exfoliate. We found that the contact angle for between PS/RDP clays substrate was ~ 2.5°, whereas the angle for PS/Cloisite 20A clays substrate was ~ 32°. Therefore, the RDP coated clays were more compatible to the styrene groups compared to the Cloisite clays, which could lead to the exfoliation of HIPS and ABS.

The ability of RDP coated clays to compatibilize polymer blends was also probed. We showed that RDP coated clays segregated to the interfaces between the phase domains in the PC/SAN24 blend, while they segregated inside the PMMA domains in the PS/PMMA blend. This different morphology between the two blends could be explained by the interfacial energy. Since the interfacial tension for either PMMA/RDP or PS/RDP clays (~ 2.8 mN/m at 180 °C) was higher than that for PS/PMMA interfaces (~ 1.2 mN/m

at 180 °C) the segregations of RDP coated clays could not reduce the interfacial energy of the system. However, the interfacial energy for PC/SAN24 blend (~ 2.8 mN/m at 200 °C) was much higher than the interfacial tension for PC/RDP clays (~ 0.5 mN/m if S=0). Hence segregation of the RDP clays to the interfaces resulted in a significant reduction of the overall energy and increased compatibilization.

We also compared the effects of RDP coated clays on the flame retardant properties of the PC/SAN24 blend; We found that the addition of the RDP clays could reduce the heat release rate (HRR) and mass loss rate (MLR) for the blends in which they were interfacial active. In contrast, the Cloisite clays, which were also interfacially active, were shown to deteriorate the flame retardant responses. In addition to stability against phase segregation, the quality of chars is another important criterion for flame retardance. We show that elasticity is an important consideration in intumescing chars, which have to expand in order to contain the gases formed by the advancing heat front. TEM images indicated that the Cloisite clays segregated to the surfaces of the chars, while the RDP coated clays remained in the interior. Nanoindentation measurements showed that the clay rich surface crust resulted in the chars of the nanocomposites containing Cloisite 20A to be 400 % more brittle than those resulting from the compounds with the RDP or Na^+ clays. These results show that surfaces, as well as interfacial energies have to be considered in engineering the optimal properties of nanocomposites and furthermore, that clays treated with non-halogen (FR) oligomers can be an alternative for replacing the functionalized clays treated with the di-tallow molecules.

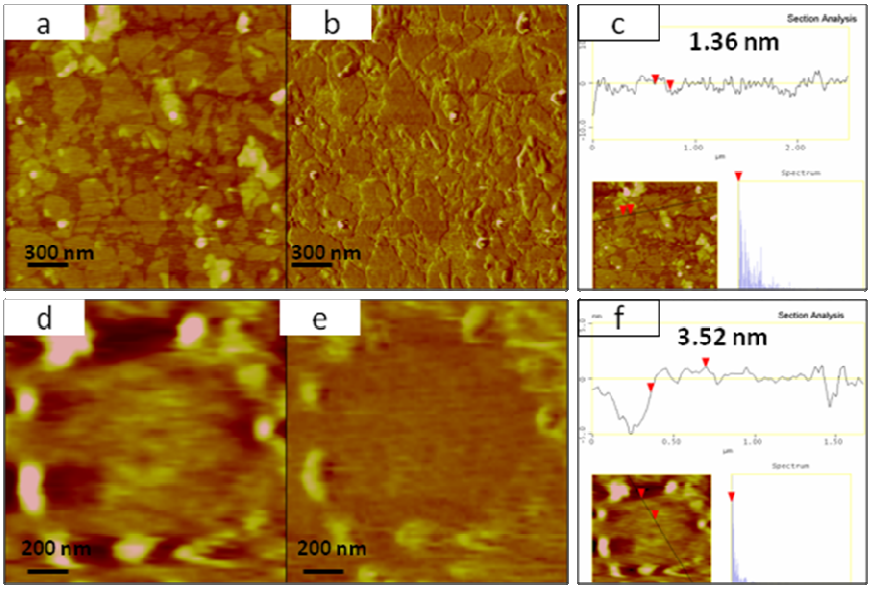

Figure 4. 1. AFM images of uncoated MMT-Na+ and RDP coated MMT-Na+: (a) Height and (b) friction, and (c) cross-section of uncoated MMT-Na+ , (d) Height and (e) friction, and (f) cross-section of RDP coated MMT-Na+.

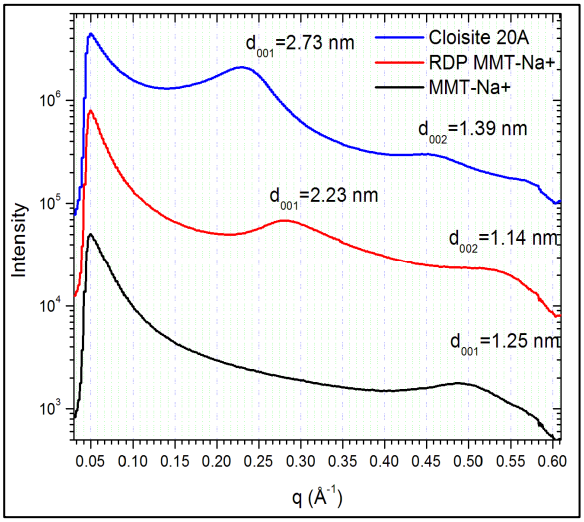

Figure 4. 2. SAXS spectra of Nanoclays.

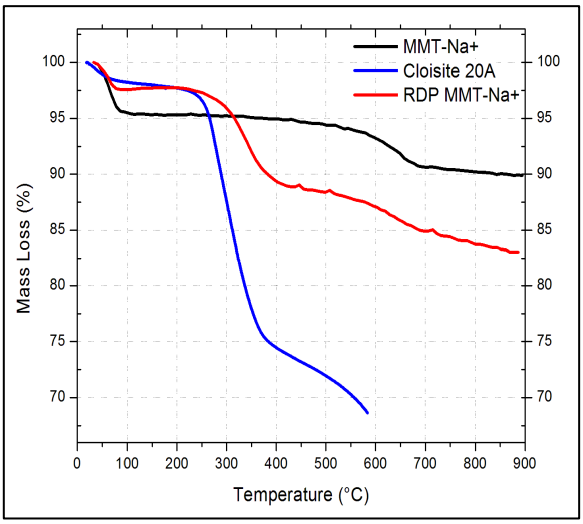

Figure 4. 3. TGA Curves of Nanoclays.

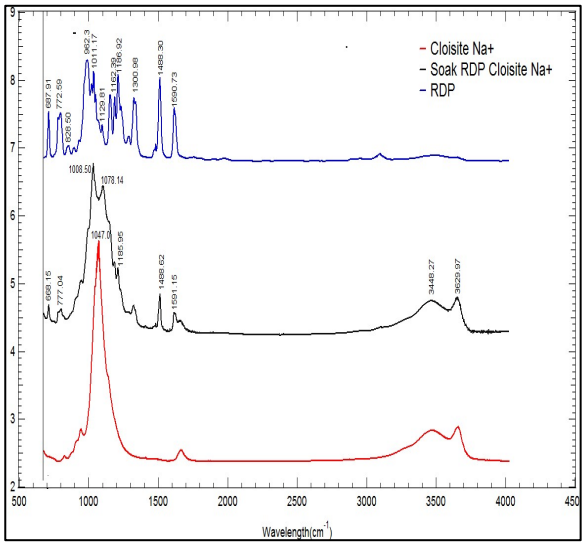

Figure 4. 4. FTIR spectra of Nanoclays: RDP – (blue line), RDP coated Cloisite Na+ - (black line), and MMT Na+ (Cloisite Na+) – (red line).

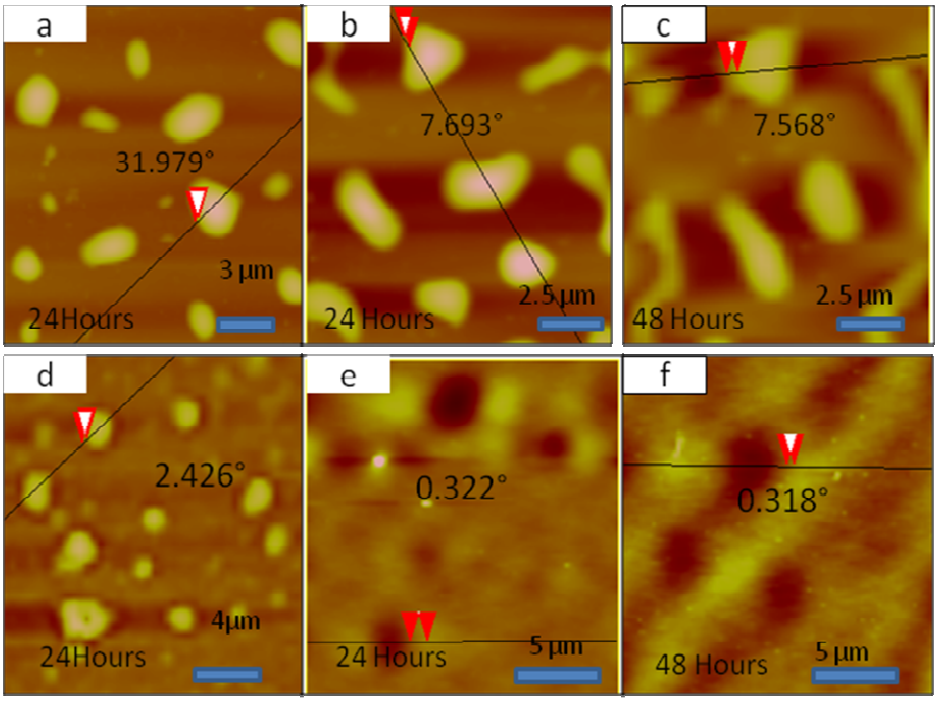

Figure 4. 5. The Contact Angles on polymer thin films on clays; (a) PS/C20A and (b) PS/RDP clays after 24 hours annealing (c) PS/RDP clays after 48 hours annealing. (d) PMMA/C20A and (e) PMMA/RDP clays after 24 hours annealing (f) PMMA/RDP clays after 48 hours annealing.

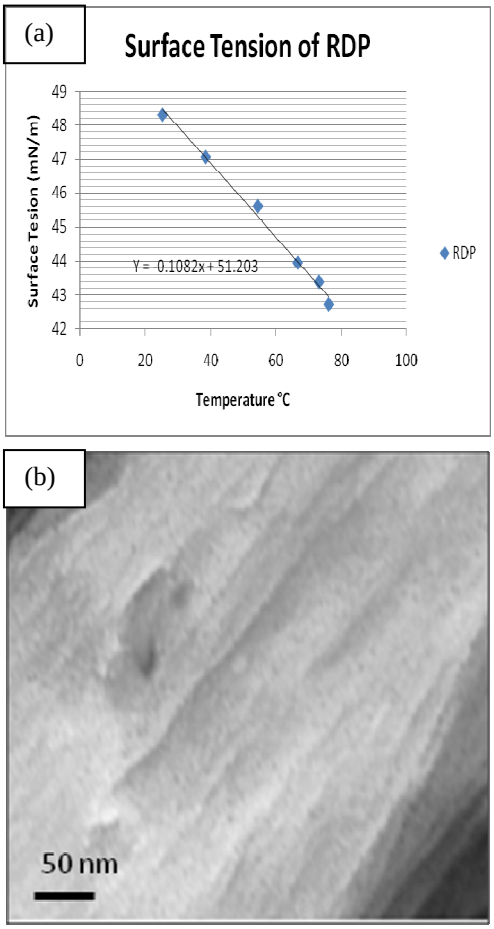

Figure 4. 6. (a) the surface tensions of RDP as a function of temperature. (b) The TEM image of a cross-section from PMMA/RDP Clays nanocomposite.

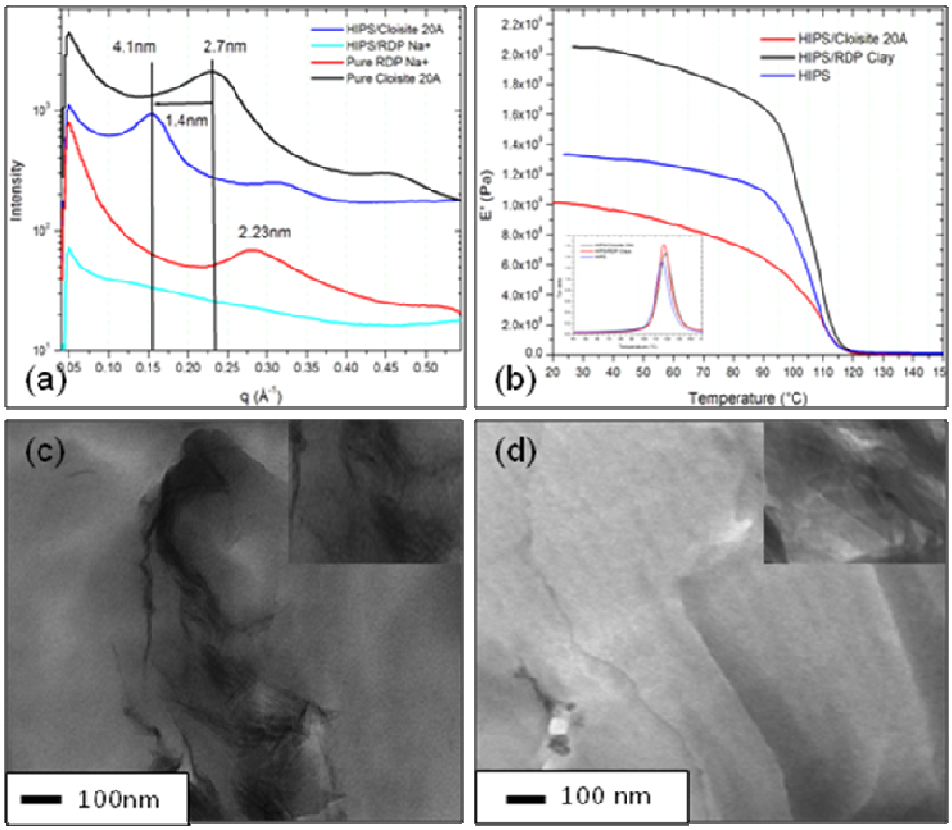

Figure 4. 7. (a) SAXS spectra of HIPS/Nanoclays nanocomposites, (b) Storage modulus and Tan delta of HIPS/RDP clays nanocomposite (the inserted image). TEM images of HIPS/Nanoclays composites: (c) HIPS/C20A- highly intercalated and (d) HIPS/RDP Clays – exfoliated.

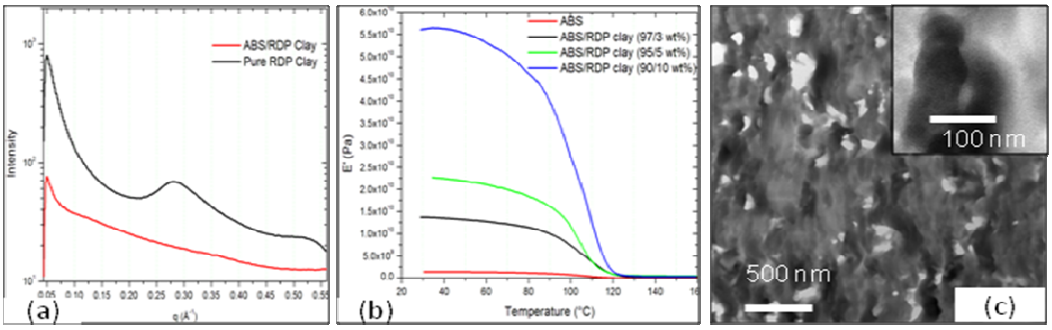

Figure 4. 8. ABS/RDP clays nanocomposites: (a) SAXS spectra, (b) Storage modulus, (c) TEM images.

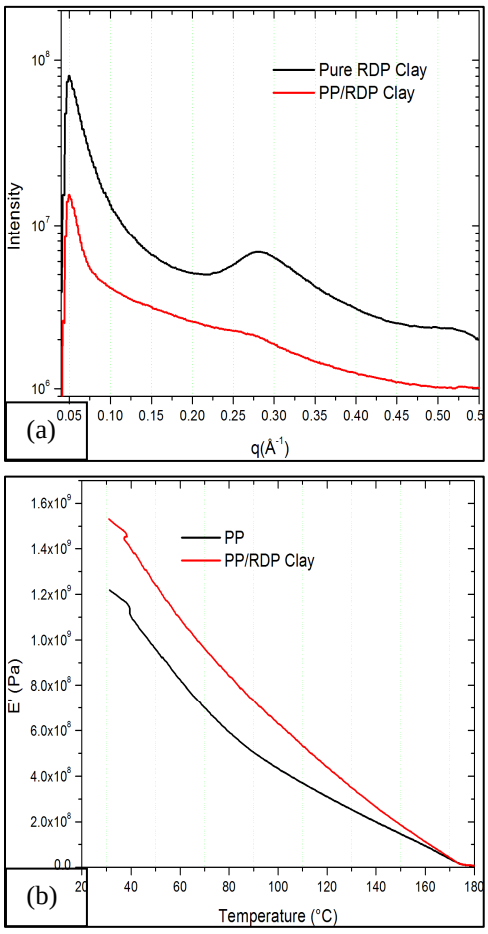

Figure 4. 9. PP/RDP clays nanocomposites: (a) SAXS spectra, (b) Storage modulus.

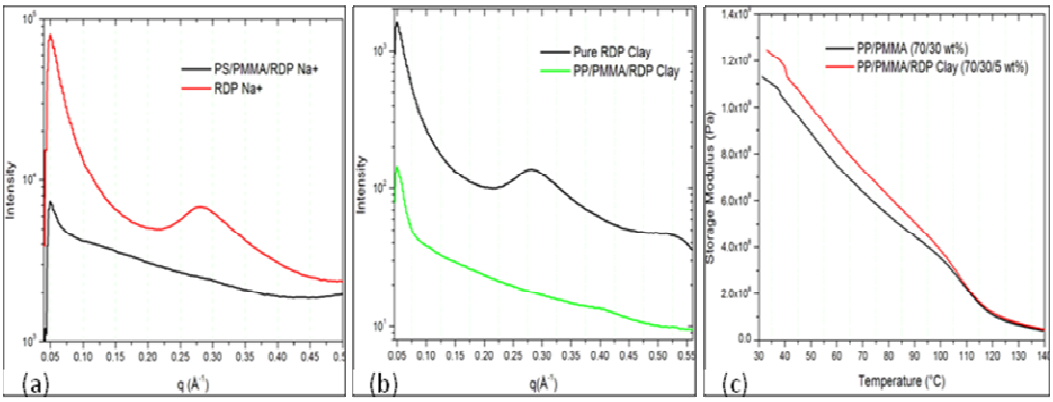

Figure 4.10. SAXS spectra: (a) PS/PMMA/RDP coated clays (70/30/5 wt%), (b) PP/PMMA/RDP coated clays (70/30/5 wt%) nanocomposites, and (c) Storage modulus of PP/PMMA/RDP coated clays.

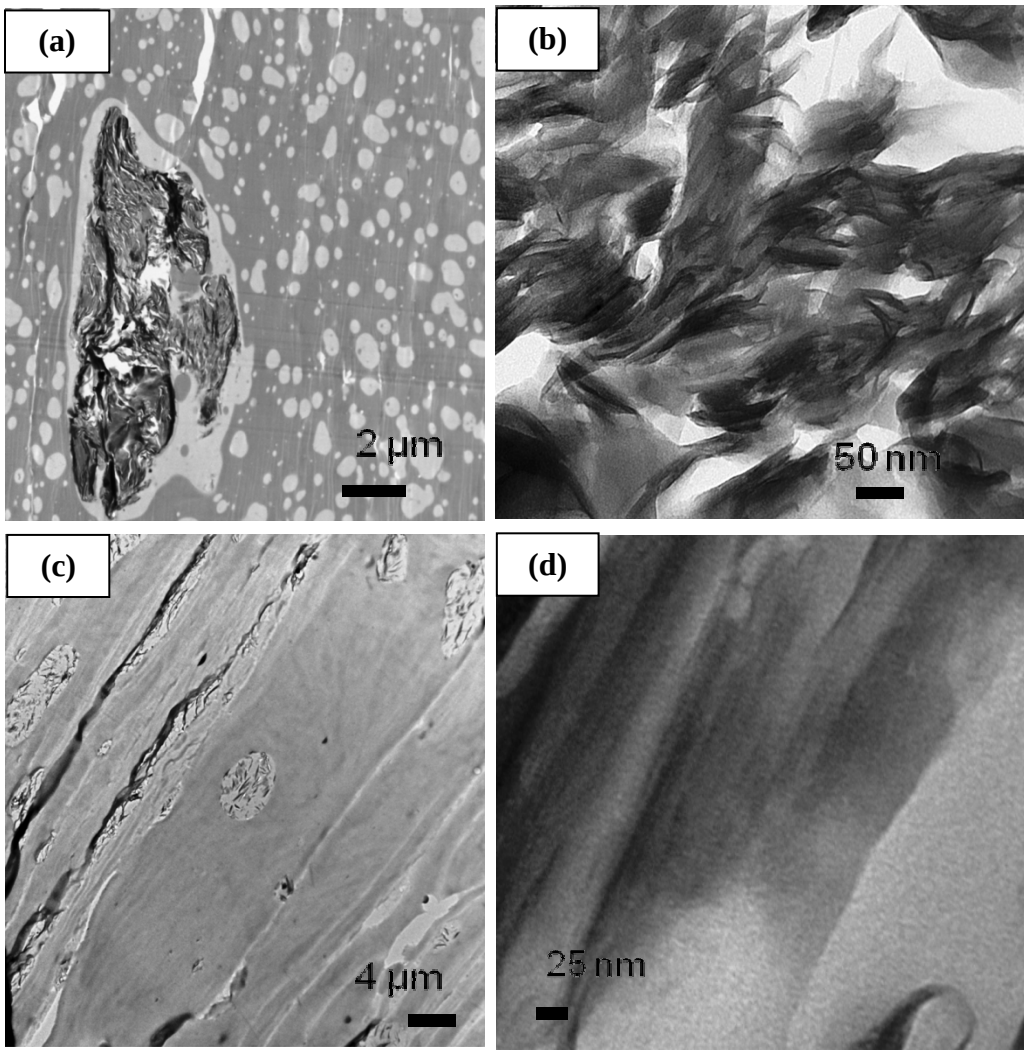

Figure 4. 11. TEM Images: PS/PMMA and PP/PMMA with the RDP clays.

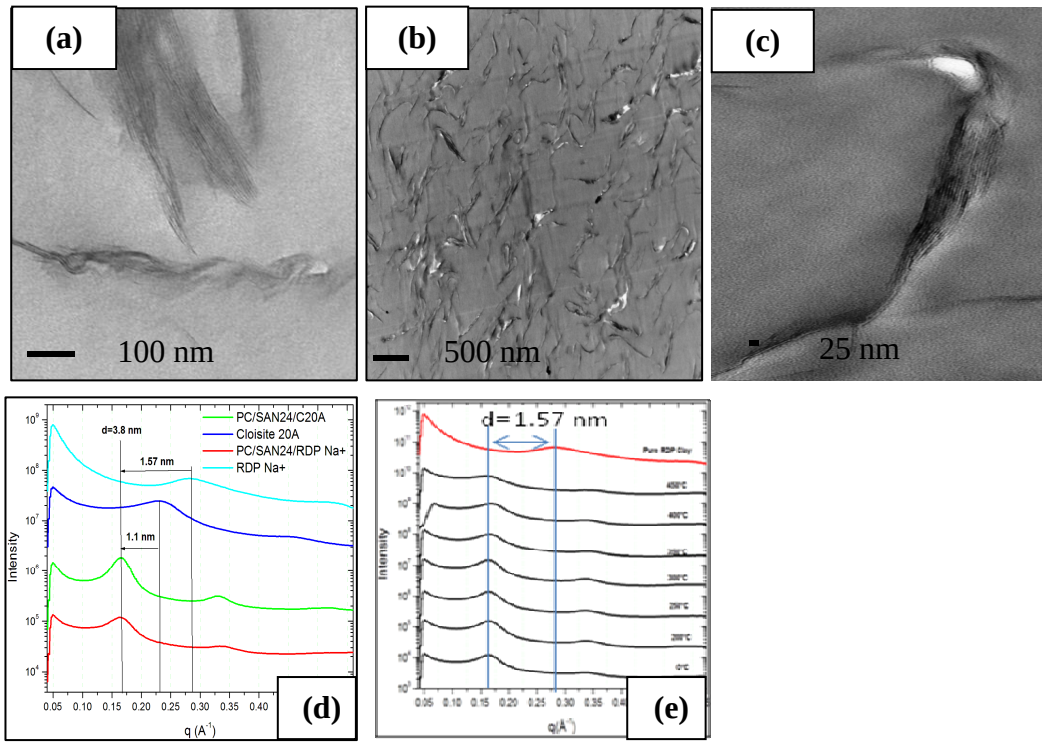

Figure 4. 12. TEM Images: (a) PC/SAN24/C20A (50/50/5 wt%), (b) PC/SAN24/RDP clays (50/50/5 wt%) - Low magnification, and (c) PC/SAN24/RDP clays (50/50/5 wt%)-High magnification. SAXS spectra: (d) PC/SAN24/RDP clays and PC/SAN24/C20A, and (e) PC/SAN24/RDP clays as a function of temperature.

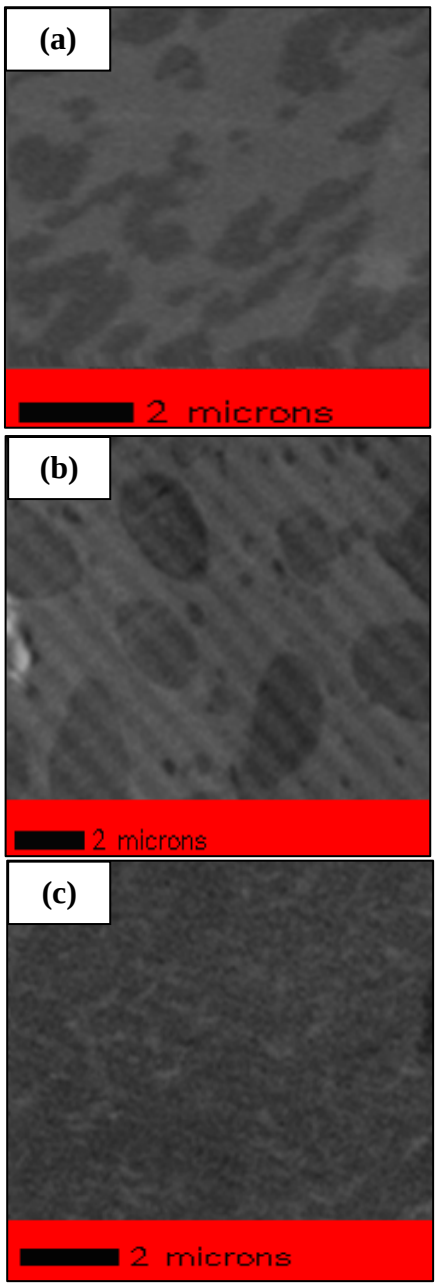

Figure 4. 13. STXM Images: (a) PC/SAN24 (50/50 wt%), (b) PC/SAN24/Cloisite Na+ (50/50/5 wt%), and (c) PC/SAN24/RDP clays (50/50/5 wt%). The Images were taken at 286.70 eV. (Dark regions are the rich SAN 24 phases)

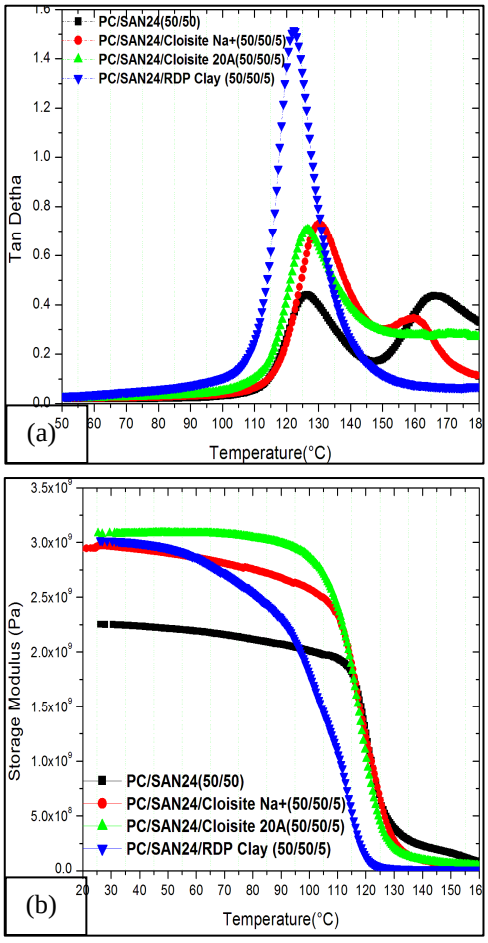

Figure 4. 14. PC/SAN24 nanocomposites: (a) Tan delta and (b) Storage modulus.

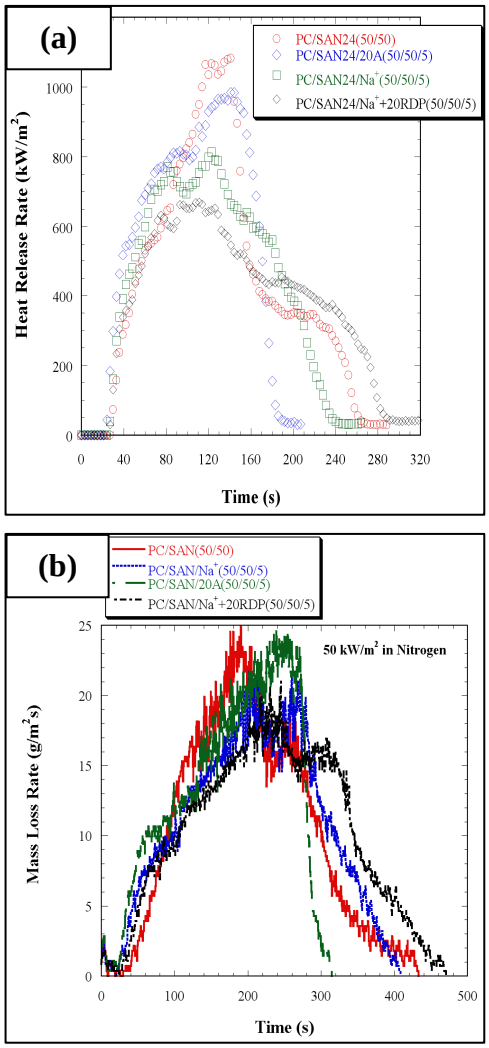

Figure 4. 15. (a) Heat release rate (HRR) and (b) Mass loss rate (MLR) of PC/SAN24/nanocomposites in N_2.

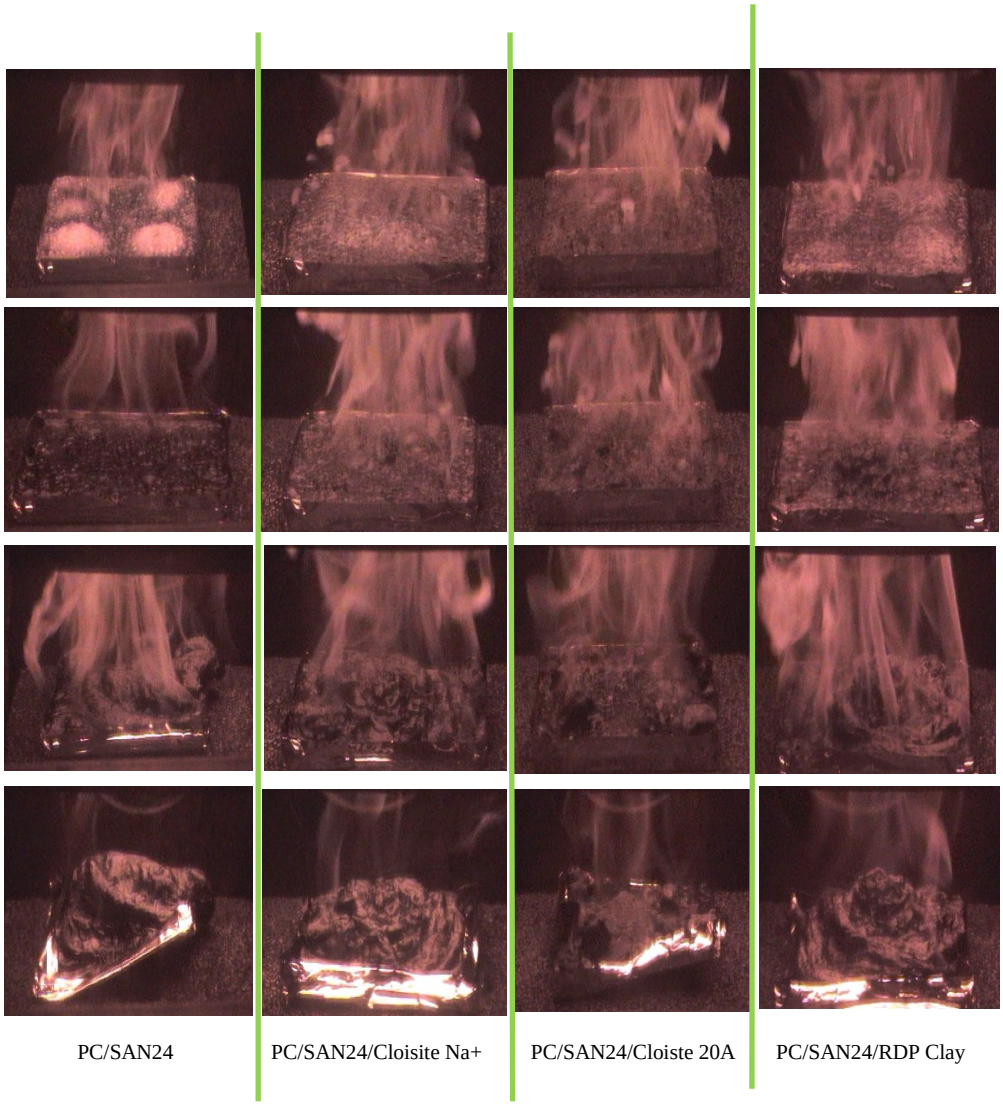

Figure 4. 16. A selected video images at 30, 100, 230, and 300 seconds from the gasification tests: PC/SAN24 (50/50 wt%) – the first column, PC/SAN24/Cloisite Na+ (50/50/5 wt%) – the second column, PC/SAN24/Cloisite 20A (50/50/5 wt%) – the third column, and PC/SAN24/RDP Clay (50/50/5 wt%)- the fourth column.

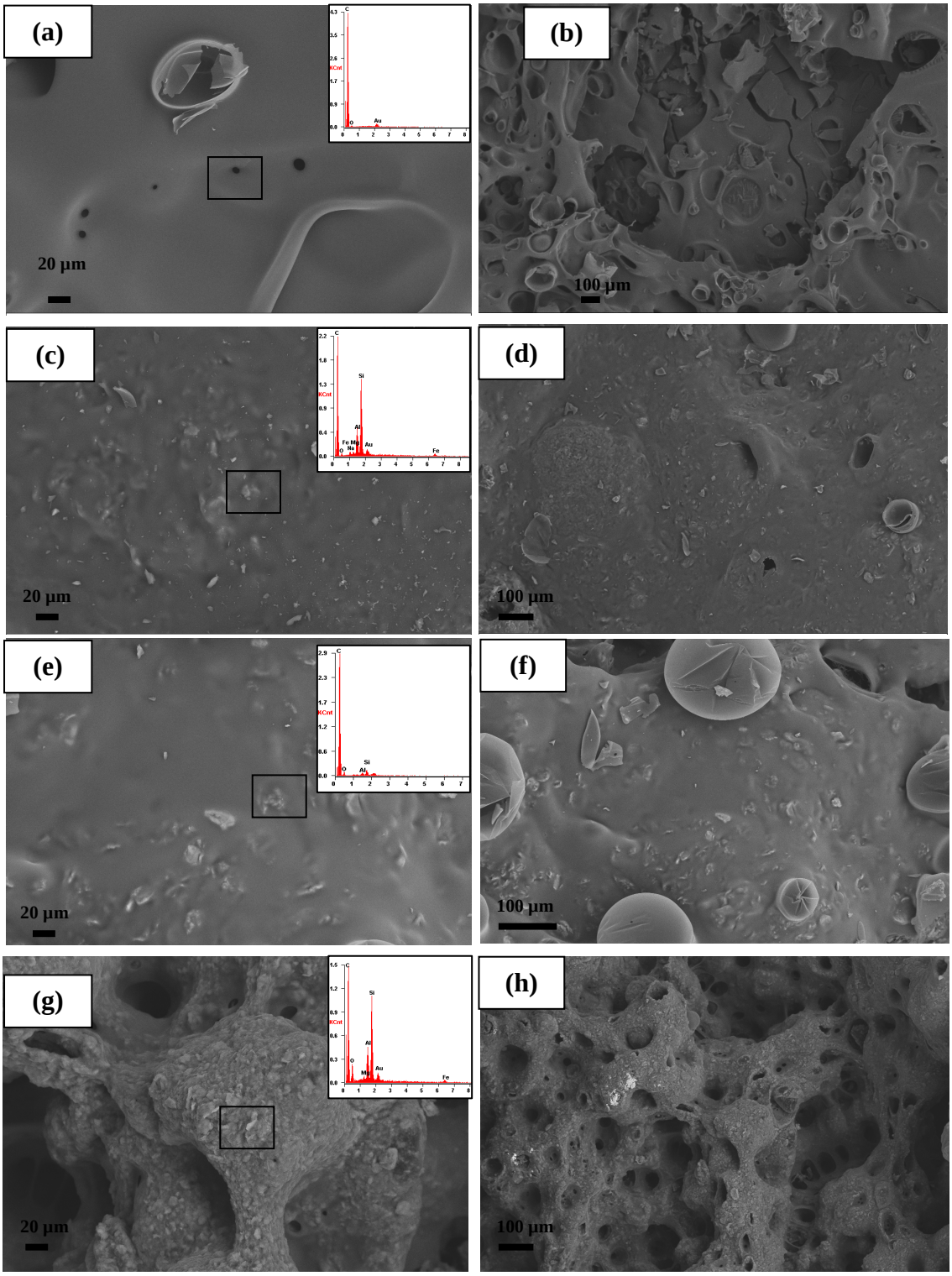

Figure 4.17. The SEM images and EDAX spectra from the residues: (a-b) PC/SAN24 (50/50 wt%) (c-d) PC/SAN24/Cloisite Na+ (50/50/5 wt%), (e-f) PC/SAN24/RDP Clay (50/50/5 wt%), and (g-h) PC/SAN24/Cloisite 20A (50/50/5 wt%).

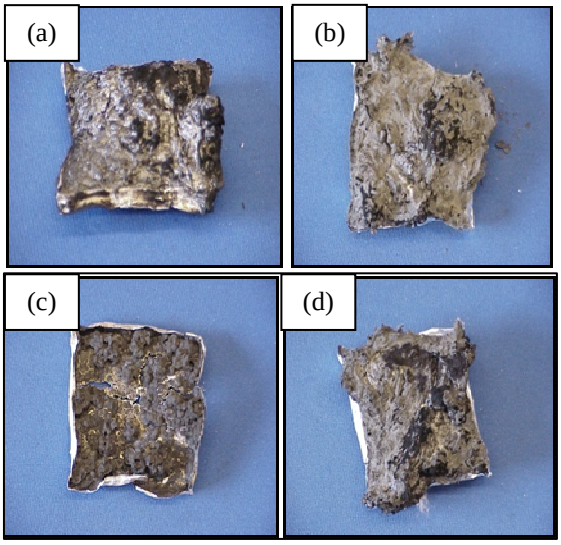

Figure 4. 18. The images of residues left after the gasification test: (a) PC/SAN24 (50/50 wt%) (b) PC/SAN24/Cloisite Na+ (50/50/5 wt%), (c) PC/SAN24/Cloisite 20A (50/50/5 wt%), and (d) PC/SAN24/RDP Clay (50/50/5 wt%).

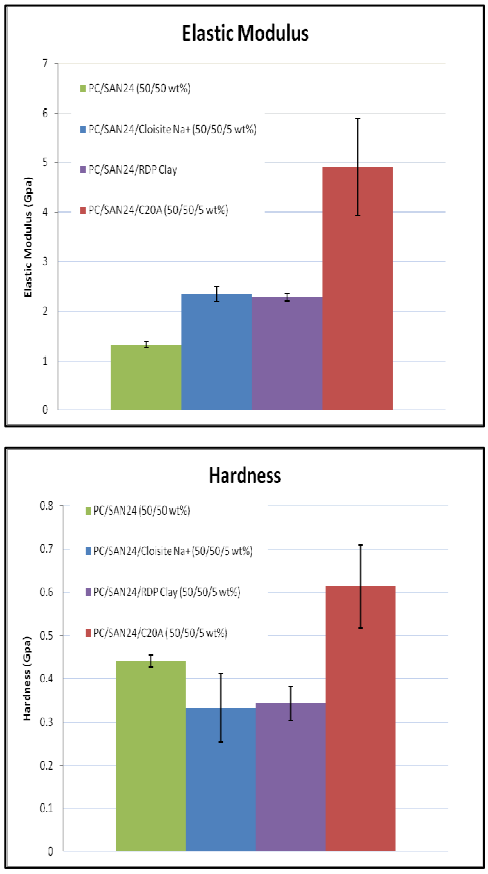

Figure 4. 19. The hardness and elastic modulus of the residues from the gasification test.

Polymer	MW or Grade	Manufacturer
Polystyrene	280k	Aldrich Sigma
Poly(methyl methacrylate) for melt blending Poly(methyl methacrylate) for spun-casting	120k 75k	Aldrich Sigma Polymer Science
Polycarbonate	23k	Mitsubishi Engineering Plastic Corp
Poly(styrene-co-acrylonitrile)	Luran ®358N	BASF
High Impact Polystyrene	5300	BASF
Acrylonitrile butadiene styrene (ABS)	Terluran® GP-35	BASF
Polypropylene	3825WZ	TOTAL PETROCHEMICALS

Table 4.1. Polymers were used in this study.

Polymer	Surface tension (mN/m)	Interfacial tension $\gamma_{Polymer/Polymer}$ (mN/m)	Interfacial tension $\gamma_{RDP/Polymer}$ (mN/m)
PS	29.2	-	2.75
PMMA	28.9	-	2.8
PS/PMMA	-	1.2	-
PP/PMMA	-	9	-
PC	29.1	-	0.5 (if S=0)
SAN24	35.3	-	-
PC/SAN24	-	2.8	-

Table 4.2. Polymer surface and interfacial tensions.

Nanocomposite	Carbonaceous chars yield
PC/SAN24	19 %
PC/SAN24/MMT	10 %
PC/SAN24/Cloisite 20A	10 %
PC/SAN24/RDP coated MMT	11 %

Table 4.3. The yield of carbonaceous chars for PC/SAN24 with clays in air.

Nanocomposite	Carbonaceous chars yield
PC/SAN24/MMT	8 %
PC/SAN24/Cloisite 20A	8 %
PC/SAN24/RDP coated MMT	3 %

Table 4.4. The yield of carbonaceous chars for PC/SAN24 with clays in air.

References

[1] Aseeva, R. M.; Zaikov, G. E. *Combustion of Polymer Materials*. Munich: Hanser, **1985**.

[2] Kuryla, W. C.; Papa, A. J. (eds.) *Flame Retardancy of Polymeric Materials*. Vols. 1-5. New York: Marcel Dekker, 1973-1979.

[3] Lewin, M.; Atlas, S. M.; Pearce, E. M. (eds.) *Flame Retardant Polymeric Materials*. Vols. 1-3. New York: Plenum Press, 1975-1982.

[4] Greand, A. E.; Wilkie, C. A. *Fire Retardancy of Polymeric Materials, Marcel Dekker, Inc.* **2000** (chapter 6 and 8).

[5] Levchik, S.; Weil, E. *Polym. Int*. **2005** 54, 981-998.

[6] Vaia, R. A.; Jandt, K. D.; Kramer, E. J.; Giannelis, E. P. *Macromolecules* **1995**, 28, 8080-8085.

[7] Kashiwagi, T.; Du, F; Douglas, J; Winey, K.I.; Harris, R.H.; Shields, J.R. *Nat. Mater*. **2005**, *4*, 928-933.

[8] Si, M.; Zaitsev, V.; Goldman, M.; Frenkel, A.; Peiffer, D.G.; Weil, E.; Sokolov, J.C.; Rafailovich, M. H. *Polymer Degradation and Stability* **2007**, 92, 86-93.

[9] Beyer, G. *Fire Mater* **2001**, 25, 193-197.

[10] Kashiwagi, T.; Mu, M; Winey, K.I.; Cipriano, B.; Raghavan, S.; Pack, S.; Rafailovich, M.; Yang, Y.; Grulke, E.; Shields, J.; Harris, R.; Douglas, J. *Polymer* **2008**, *49*, 4358-4368.

[11] Vaia, R. A.; Teukolsky, R. K.; Giannelis, E. P. *Chem. Mater.* **1994**, *6*, 1017-1022.

[12] Xie, W.; Gao, Z.; Pan, W.; Hunter, D.; Singh, A.; Vaia, R. *Chem. Mater.* **2001**, *13*, 2979-2990.

[13] Shi, H.; Lan, T.; Pinnavaia, T. J. *Chem. Mater.* **1996,** *8*, 1584-1587.

[14] Krishnamoorti, R.; Vaia, R. A.; Giannelis, E. P. *Chem. Mater.* **1996,** *8*, 1728-1734.

[15] Kawasumi, M.; Hasegawa, N.; Kato, M.; Usuki, A.; Okada, A. *Macromolecules* **1997**, *30*, 6333-6338.

[16] Yoon, J. T.; Jo, W. H.; Lee, M. S.; Ko, M. B. *Polymer* **2001**, *42*, 329-336.

[17] Fu, X.; Qutubuddin, S. *Polymer* **2001**, *42*, 807-813.

[18] Yeh, J.; Liou, S.; Lin, C.; Cheng, C.; Chang, Y. *Chem. Mater.* **2002,** *14*, 154-161.

[19] Lee, K. M.; Han, C. D. *Polymer* **2003**, *44*, 4573-4588.

[20] Si, M.; Goldman, M.; Rudomen, G.; Gelfer, M. Y.; Sokolov, J. C.; Rafailovich, M. H. *Macromol. Mater. Eng*. **2006**, 291, 602-611.

[21] Jimenez, G.; Ogata, N.; Kawai, H.; Ogihra, Y. *J. Appl. Polym. Sc/.* **1997**, *64*, 2211-2200.

[22] Mitsunaga, M.; Ito, Y.; Ray, S. S.; Okamoto, M.; Hironaka, K. C. *Macromol. Mater. Eng*. **2003**, 288, 543-548.

[23] Hu, X.; Zhang, W.; Si, M.; Gelfer, M.; Hsiao, B.; Rafailovich, M.; Sokolov, J.; Zaitsev, V.; Schwarz, S. *Macromolecules* **2003**, *36*, 823-829.

[24] Kim, J. H.; Kim, J. H. *J. Appl. Polym. Sc/.* **2003**, *89*, 2649-2656.

[25] Gelfer, M. Y.; Song, H. H.; Liu, L.; Hsiao, B. S.; Chu, B.; Rafailovich, M.; Si, M. ; Zaitsev, V. *J. Polym. Sc/. Part B: Polym. Phys.* **2003**, *41*, 44-54.

[26] Wang, Y.; Zhang, Q.; Fu, Q. *Macromol. Rapid. Commun*. **2003**, *24*, 231-235.

[27] Seo, Y. S.; Kim, J. H.; Kim, C. K.; Lee, R.; Keum, J. K. *J. Appl. Polym. Sci.* **2005**, *96*, 2097-2104.

[28] Gelfer, M. Y.; Burger, C.; Chu, B.; Hsiao, B. S.; Drozdov, A. D.; Si, M.; Rafailovich, M.; Sauer, B. B.; Gilman, J. W. *Macromolecules* **2005**, *38*, 3765-3775.

[29] Ray, S. S.; Bousmina, M. *Macromol. Rapid. Commun*. **2005**, 26, 1639-1646.

[30] Ray, S. S.; Bousmina, M. *Macromol. Rapid. Commun*. **2005**, 26, 450-455.

[31] Si, M.; Araki, T.; Ade, H.; Kilcoyne, A. L. D.; Fisher, R.; Sokolov, J. C.; Rafailovich, M. H. *Macromolecules* **2006**, *39*, 4793-4801.

[32] Hampsch, H.L.; Yang, J.; Wong, G.K.; Torkelson, J.M *Macromolecules* **1988**, *21*, 528-530.

[33] Kashiwagi, T.; Inaba, A.; Brown, J.E.; Hatada, K.; Kitayama, T.; Masuda, E. *Macromolecules* **1986**, *19*, 2160-2168.

[34] Kashiwagi, T.; Harris, R. H.; Zhang, X.; Briber, R. M.; Cipriano, B. H.; Raghavan, S. R.; Awad, W. H.; Shields, J. R. *Polymer* **2004**, *45*, 881-891.

[35] Gilman, J. W. *Appl. Clay. Sci.* **1999**, *15*, 31-49.

[36] Morgan, A. B.; Harris, R. H.; Kashiwagi, T.; Chyall, L. J. Gilman, J. W. *Fire. Mater.* **2002**, 26, 247-253.

[37] Pack, S.; Si, M.; Koo, J.; Sokolov, J.; Koga, T.; Kashiwagi, T.; Rafailovich, M. H. Polym. Degrad. Stab. 2009, 93, 306-326.

[38] Rhodes, B. T.; Quintiere, J. G. *Fire Safety J.* **1996**, 26, 221-240.

[39] Hopkins Jr, D.; Quintiere, J. G. *Fire Safety J.* **1996**, 26, 241-268.

[40] Greand, A. E.; Wilkie, C. A. *Fire Retardancy of Polymeric Materials*. Marcel Dekker, Inc.; 2000.

[41] Tewarson, A. *Thermochim Acta* **1996**, *278*, 19-37.

[42] Wang, D.; Echols, K.; Wilkie, C. A. *Fire. Mater.* **2005**, 29, 283-294.

[43] Sahoo, P. K.; Samal, *Polymer Degradation and Stability* **2007**, 92, 1700-1707.

[44] Gilman, J. W.; Jackson, C. L.; Morgan, A. B.; Harris Jr., R. *Chem. Mater.* **2000**, 12, 1866-1873.

[45] Tang, Y.; Lewin, M. *Polymer Degradation and Stability* **2007**, 92, 52-60.

[46] Zhu, J.; Morgan, A. B.; Lamelas, F. J.; Wilkie, C. A. *Chem. Mater.* **2001**, 13, 3774-3780.

[47] Tang, Y.; Lewin, M.; Pearce, E. M. *Macromol. Rapid. Commun.* **2006**, 27, 1545-1549.

[48] Newvile M. J., *Synchrotron Rad.* 2001; 8:322.Newvile M. IFEFFIT: interactive XAFS analysis and FEFF fitting. J.Synchrotron Rad 2001; 8:322.

[49] Kashiwagi, T.; Mu, M; Winey, K.I.; Cipriano, B.; Raghavan, S.; Pack, S.; Rafailovich, M.; Yang, Y.; Grulke, E.; Shields, J.; Harris, R.; Douglas, J. *Polymer* **2008**, *49*, 4358-4368.

[50] Jang, B.K.; Wilkie, C.A. *Polymer* **2005**, *46*, 2933-2942.

[51] Koo, J.; Shin, K.; Si, M.; Gelfer, M.; Hsiao, B.; Rafailovich, M.; Sokolov, J.; Zaitsev, V.; Schwarz, S. *Macromolecules* **2003**, *36*, 823-829.

[52] Zhang, Y.; Ge, S.; Tang, B.; Rafailovich, M.H.; Sokolov, J.C.; Peiffer, D.G.; Li, Z.; Dias, A.J.; McElrath, K.O.; Satija, S.K.; Lin, M.Y.; Nguyen, D. *Langmuir* **2001**, *17*, 4437-4442.

[53] Georlette, P.; Simons, J. Halogen-Containing Fire-Retardant Compounds. In *Fire Retardancy of Polymeric Materials*; Grand, A. E.; Wilkie, C. A., Eds.; Marcel Dekker, Inc.: New York, NY, **2000**; pp 246-254.

[54] *Polymer Handbook (4th edn)*; Brandrup, J.; Immergut, E.H.; Grulke, E.A., Eds.; Wiley: New York, NY, **1999**.

[55] *Handbook of Chemistry and Physics (70th edn)*; Weast, R.C.; Lide, D.R.; Astle, M.J.; Beyer, W.H. Eds.; CRC Press, Inc.: Boca Raton, Florida, **1989–1990**.

[56] Xie, H.; Cai, A.; Wang, X. *Phys. Lett. A* **2007**, *369*, 120-123.

[57] Si, M.; Hefter J.; Song, A.; Rafailovich, M.H.; Sokolov, J.C. *J adhesion Sci. Technol.* **2005**, *19*, 1459-1474.

[58] Bao, S.P.; Tjong, S.C. *Mater. Sci. Eng. A* **2008**, *485*, 508-516.

[59] Balazs, A. C.; Emrick, T.; Russell, T.P. *Science* **2006**, *314*, 1107-1110.

[60] Gelfer, M.; Burger, C.; Fadeev, A.; Sics, I.; Chu, B.; Hsiao, B. S.; Heintz, A.; Kojo, K.; Hsu, S-L.; Si, M.; Rafailovich, M. *Langmuir* **2004**, *20*, 3736-3758.

[61] Vaia, R.A.; Giannelis, E. P. *Macromolecules* **1997**, *30*, 7990-7999.

[62] Vaia, R.A.; Giannelis, E. P. *Macromolecules* **1997**, *30*, 8000-8009.

[63] Starr, F. W.; Schroder, T. S.; Glotzer, S. C. *Macromolecules* **2002**, *35*, 4481-4492.

[64] Pack, S.; Kashiwagi, T.; Stemp, D.; Koo, J.; Si, M.; Sokolov, J. C.; Rafailovich, M. H. *Macromolecules*. **2009**, *42*, 6698-6707.

[65] Khatu, B. B.; Lee, D.; Kim, H.; Kim, J. *Macromolecules* **2004**, *37*, 2454-2459.

[66] Li, Y.; Shimizu, H. *Macromol Rapid Commun*. **2005**, *26*, 710-715.

[67] Yoo, Y.; Park, C.; Lee, S.; Choi, K.; Kim, D.; Lee, J. *Macromol. Chem. Phys*. **2005**, *206*, 878-884.

[68] Ray, S. S.; Pouliot, S.; Bousmina, M.; Utracki, L. A. *Polymer* **2004**, *45*, 8403-8413.

[69] Nesterov, A. E.; Lipatov, Y. S. *Polymer* **1999**, *40*, 471-481.

[70] Lipatov, Y. S.; Nesterov, A. E.; Ignatova, T. D.; Nesterov, D. A. *Polymer* **2002**, *43*, 875-880.

[71] Koo, J.; Park, S.; Satija, S.; Tikhonov, A.; Sokolov, J. C.; Rafailovich, M. H.; Koga, T. J. *Colloid Interface Sci.* **2008**, *318*, 103-109.

[72] Zeng, C.; Lee, L. J. *Macromolecules* **2001**, *34*, 4098-4103.

[73] Chen, B.; Evans, R. G. *Carbohydr. Polym.* **2005**, *61*, 455-463.

[74] Pluta, M.; Paul, M.; Alexandre, M.; Dubois, P. *J. Polym. Sci., Part B: Polym. Phys.* **2006**, *44*, 299-311.

[75] Hou, S.; Schmidt-Rohr, K. *Chem. Mater.* **2003**, *15*, 1938-1940.

[76] Sarkar, M.; Dana, K.; Ghatak, S.; Banerjee, A.; *Bull. Mater. Sci.* **2008**, *31*, 23-28.

[77] Ramazani, A.; Tavakolzadeh, F.; Baniasadi, H. *J. Appl. Polym. Sci.* **2009**, *115*, 308-314.

[78] Modro, A. M.; Modro, T. *A Can. J. Chem.* **1999**, *77*, 890-894.

[79] Ade, H.; Smith, A. P.; Cameron, S.; Cieslinski, R.; Mitchell, G.; Hsiao, B.; Rightor, E. *Polymer* **1995**, *36*, 1843-1848.

[80] Ade, H.; Winesett, D. A.; Smith, A. P.; Qu, S.; Ge, S.; Sokolov, J.; Rafailovich, M. *Europhys. Lett.* **1999**, *45*, 526-532.

[81] Vaia, R. A.; Ishii, H.; Giannelis, E. P. *Chem. Mater.* **1993**, *5*, 1694-1696.

[82] Jang, B.; Wilkie, C. A. *Thermochim. Acta* **2005**, 433, 1-12.

[83] Cole, K. C. *Macromolecules* **2008**, *41*, 834-843.

[84] Yan, L.; Roth, C. B.; Low, P. F. *Langmuir* **1996**, *12*, 4421-4429.

[85] Wu. S. *J. Phy.Chem.* **1970**, *74*, 632-638.

[86] Wyart, F. B.; Martin, P.; Redon, C. *Langmuir* **1993**, *9*, 3682-3690.

[87] Carriere, C. J.; Biresaw, G.; Sammler, R. L. *Rheol. Acta* **2000**, *39*, 476-482.

[88] Zhang, X.; Kim, J. *Macromol Rapid Commun*. **1998**, *19*, 499-504.

[89] Valera, T. S.; Morita, A. T.; Demarquette, N. R. *Macromolecules* **2006**, *39*, 2663-2675.

[90] Faldi, A.; Composto, R. J.; Winey, K. I. *Langmuir* **1995**, *11*, 4855-4861.

[91] Watkins, V. H.; Hobbs, S. Y. *Polymer* **1993**, *34*, 3955-3959.

[92] Zhu, J.; Uhl, F. M.; Morgan, A. B.; Wilkie, C. A. *Chem. Mater.* **2001**, *13*, 4649-4654.

[93] Watkins, V. H.; Hobbs, S. Y. *Polymer* **1993**, *34*, 3955-3959.

[94] Hobbs, S. Y.; Dekkers, E. J.; Watkins, V. H. *Polymer* **1988**, *29*, 1598-1602.

[95] Qin, H.; Zhang, S.; Zhao, C.; Hu, G.; Yang, M. *Polymer* **2005**, *46*, 8386-8395.

[96] Vanorio, T.; Prasad, M.; Nur, A. *Geophys. J. Int.* **2003**, 155, 319-326.

[97] Chen, B.; Evans, J. R. G. Scr. Mater. **2006**, 54, 1581-1585.

[98] Oliver, W.C.; Pharr, G.M. *J. Materials Res.* **1992,** 7, 1564-1583.